

The Study of CO₂ Conversion in a Microwave Plasma/Catalyst System

by

Laura Frances Spencer

A dissertation submitted in partial fulfillment
of the requirements for the degree of
Doctor of Philosophy
(Applied Physics)
in The University of Michigan
2012

Doctoral Committee:

Professor Alec D. Gallimore, Chair
Professor Mark Kushner
Associate Professor John E. Foster
Lecturer Timothy B. Smith

© Laura Frances Spencer 2012

All Rights Reserved

For the person who first inspired me to discover the world through physics, Dean
Sousanis.

ACKNOWLEDGEMENTS

While the defined nature of obtaining a PhD requires the individual to perform and complete independent work, it can never be successfully accomplished without the help and support of an entire network of people. From staff, faculty, colleagues, friends, and family, one needs all of these people to survive the roller coaster ride of a PhD program to the end. I would like to take this opportunity to sincerely thank and acknowledge my own network of people that have helped me through this journey.

First I would like to thank my advisor, Professor Alec Gallimore, for allowing me to pursue a research area outside of his typical domain of electric propulsion. He saw and understood my interest in the environmental applications of plasma and gave me encouragement and support to perform this research. Professor Gallimore provided enough freedom for me to examine and explore my dissertation topic independently, while still providing enough guidance to keep me from losing my way. While he may not have had the answers to all the problems I encountered, he always asked the right questions so that I could come to the answer on my own. This style of mentorship has given me the confidence and ability to approach any scientific or technical challenge and find a solution. I greatly appreciate all the professional and personal advice Professor Gallimore has given over the years, and for providing an exceptional example of what it means to be a good leader and mentor.

In addition to my advisor, my dissertation committee members Professor Mark Kushner, Professor John Foster, and Dr. Tim Smith have also offered their time and support to enable me to complete my research project. I am extremely grateful

for their willingness to meet and discuss any difficulty I experienced throughout my research, offering their invaluable knowledge to help me along the way. This project has been greatly enhanced by the amazing team of faculty at my disposal.

I would like to express my gratitude to the three organizations which provided funding throughout my doctoral degree: the Michigan Regents Fellowship, the National Science Foundation Graduate Research Fellowship Program, and the Michigan Institute for Plasma Science and Engineering Graduate Fellowship. The financial scholarships awarded through these programs have made it possible for me to obtain my degree.

Many thanks goes out to the staff of Applied Physics and Aerospace Engineering for all of their hard work behind the scenes. The Applied Physics administration team, Cynthia McNabb and Charles Sutton, have given a depth of kindness and understanding that has become the foundation of the Applied Physics Program, treating me like a family member since the very first day I arrived on campus. The administrative support from Denise Phelps and Cynthia Enoch in Aerospace Engineering has made it possible for me to successfully pursue research in Professor Gallimore's group, even though I am not officially an Aerospace student. Similarly, the Aerospace Engineering technical staff members Tom Griffin, Eric Kirk, and Dave McLean have always kept an open door, willing to help with any technical problem or concern I might have.

I am indebted to two very kind and generous people in the Chemical Engineering Department. First I would like to thank Harold Eberhart, the talented and warm-hearted glassblower of Chemical Engineer who helped design the oil-cooled quartz discharge tube that made this entire plasma experiment possible. I have lost count of all the beautifully-crafted quartz tubes Harold made for me, that were eventually destroyed because of my plasma. Without his skill and expertise in the field of glassblowing, I would have been utterly lost. Additionally, I would like to thank fellow graduate student Steve Edmund. He was gracious enough to offer his time and skills

to fabricate the catalyst materials used in my experiments. Without his willingness to help I would not have been able to test the influence of catalysts in my plasma system, and for that I am extremely grateful.

I may not have made it past my first year of graduate school without the help of my fellow first year colleagues in Applied Physics: Nick Patterson, Ryan Murphy, Franklin Dollar, Meredith Brenner, Aaron Rury, Andrea Bianchini, Kyle Renshaw, and Devon Triplett. During my first semester, I spent more time with these individuals going to class or working on homework than I did doing any other activity. We were a team, conquering Electrodynamics (aka 'Jackson'), Quantum Mechanics, Statistical Mechanics and our qualifying exam together. I am truly grateful for the friendship and support I received during that first year. Particularly, Devon has become a dear friend over these past five years, and I cannot thank her enough for her positive and selfless attitude that has helped me through some of my toughest days.

When I joined the Plasmadynamics and Electric Propulsion Laboratory during my second semester, I was introduced to a group of intelligent and talented graduate students. For those who were senior students when I arrived and have since become doctors, Bryan Reid, Robbie Lobbia, Kristina Lemmer, Sonca Nguyen, and Tom Lui, thank you for preserving and passing down a collaborative environment where we are all encouraged to help and learn from one another. You were all willing to help me become accustomed to the many different facets of experimental research when I was just a 'newbie' and I appreciate your kindness. Sonca, thank you for mentoring me during my first year in the lab, being the first to show me how to make a Swagelok fitting which I have come to do at least 100 times over. Dr.'s Rohit Shastry, Ricky Tang, David Huang, and Mike McDonald were closer in year, and I was able to observe first hand the fruits of their perseverance as they completed their dissertations to officially become doctors. I have learned far more about Hall thruster dynamics, probes, electron trajectories, and laser alignment than I ever imagined. Ricky, thanks

for your congruent need of a microwave system, otherwise I may have been left trying to produce a plasma with Alec's old microwave oven!

My colleagues Ray Liang and Adam Shabshelowitz have witnessed my entire journey moving from Junior to CTF and finally to the microwave system. If only I had ran an experiment in LVTF and my experience would have been complete. Ray, while our typical working hours did not often overlap, I appreciate your consistently positive attitude in the lab, and for teaching me the value of meticulous experimental preparation. Adam and I have shared in the struggles of RF plasmas. Thank you for monitoring lab safety with your RF meter every time I ran an experiment and for placing the popcorn kernels around my system, just in case there was a leak, haha! For those students with a bit more time left in the lab, Roland Florenz (who has taught me more than I intended to know about international music and foreign language), Kim Trent (the lab safety manager), Chris Durot (the new laser guy), Mike Sekerak (soon-to-be HDLP expert), and Chris Bellant (our newest addition), thank you for continuing to demonstrate the quality and excellence of personnel that our lab has become known for. You have all been amazing colleagues, not just from a technical academic standpoint but from a personal standpoint as well, making the experimental research environment infinitely more enjoyable.

In my personal life, I would like to thank my family and close friends that have supported me long before I began the PhD program and will continue to give support long after. I would not be where I am today without the determination, character, and work-ethic instilled in me by my parents. Mom and Dad, I have come a long way from the shy little girl on the farm to the confident research scientist I am now. Thank you for all that you have done and all that you continue to do. I am thankful for my wonderful sister who will always be there for me no matter the circumstance, and for my talented brother, whose music helped me focus to finish my dissertation. Of course I cannot forget my lifelong friends, Melanie Anspaugh, Karen Vitrone, and

Amanda Warner. Thank you for your irreplaceable friendship, I cannot wait until our next crazy adventure!

Lastly, my deepest thanks belongs to my best friend and partner in life, Phil Weaver. He has waited patiently for me to finish my degree, choosing to remain in Michigan on my behalf while spending 4 years traveling back and forth on weekends to see one another, never complaining once. Thank you for being the calm and steady rock in my life, anchoring me to the ground when life threatens to blow me off course. You have kept me balanced and sane during this journey and I am extremely grateful to have you in my life. Thank you for being the exceptional person that you are.

TABLE OF CONTENTS

DEDICATION	ii
ACKNOWLEDGEMENTS	iii
LIST OF FIGURES	xi
LIST OF APPENDICES	xiv
LIST OF ABBREVIATIONS	xv
CHAPTER	
I. Introduction	1
1.1 Motivation	1
1.2 Aim of Research	3
1.3 Dissertation Overview	4
II. Background	6
2.1 Energy Crisis and Climate Change	6
2.1.1 Energy Challenge	6
2.1.2 Climate Change	13
2.1.3 Predictions for the Future	18
2.2 CO ₂ Remediation Efforts	22
2.2.1 Policy Efforts	22
2.2.2 Technological Efforts	24
2.3 Conclusions	26
III. Plasma Systems	28
3.1 Overview of Plasmas	29
3.1.1 Introduction to Plasma	29
3.1.2 Collisional Processes in Plasmas	31

3.1.3	Plasma Sources	40
3.2	Plasma Processes for CO ₂ Dissociation	50
3.2.1	Vibrational Excitation	52
3.2.2	Electronic Excitation	53
3.2.3	Thermal Discharges	54
3.2.4	Non-thermal Discharges	55
3.3	Plasma/Catalyst Systems	58
3.3.1	Overview of Catalysis	58
3.3.2	Types of Plasma/Catalyst Systems	61
3.4	Conclusions	64
IV. Preliminary Investigation in a Helicon Source		65
4.1	Hypothesis	65
4.1.1	Benefits of Helicon Source	65
4.2	Research Design	66
4.2.1	Experimental Setup	66
4.2.2	Diagnostics	67
4.3	Results	69
4.3.1	Applied Magnetic Field Effects	72
4.3.2	Energy and Conversion Efficiencies	73
4.4	Efficiency Requirements	76
4.5	Conclusions	78
V. Microwave Plasma/Catalyst System		79
5.1	Benefits of Microwave Plasmas	79
5.2	Experimental Setup	82
5.2.1	Microwave System	82
5.2.2	Oil-Cooled Discharge Tube	86
5.3	Catalyst Material	89
5.3.1	Rhodium-Coated Monoliths	89
5.4	Diagnostics	92
5.4.1	Residual Gas Analyzer	92
5.4.2	Optical Emission Spectroscopy	94
5.5	GlobalKin	100
5.5.1	Description of Model	100
5.5.2	CO ₂ Microwave Plasma Model	103
5.6	Summary	105
VI. Results and Discussion		107
6.1	Plasma System Results	107
6.1.1	Initial Plasma Observations	107
6.1.2	Mass Spectrometry of the CO ₂ /Ar Plasma	110

6.1.3	Optical Emission Spectroscopy of the CO ₂ /Ar Plasma	117
6.2	Plasma/Catalyst Results	125
6.2.1	Control Test with Uncoated Monolith	125
6.2.2	Rh/TiO ₂ Catalyst Test	127
6.3	Computational Results	130
6.3.1	Simulated Efficiencies	130
6.3.2	Simulated Plasma Properties	132
6.3.3	Flow Rate and Pressure Effects	136
6.4	Discussion	138
6.4.1	Experimental Results	138
6.4.2	Computational Results	143
6.4.3	Cost Analysis	146
6.5	Summary	150
VII. Conclusions		152
7.1	Experimental Conclusions	153
7.1.1	Development of Atmospheric Pressure Microwave Plasma Source	153
7.1.2	Plasma System Characterization	154
7.1.3	Plasma/Catalyst System Characterization	155
7.2	Computational Conclusions	156
7.3	Cost Impact	156
7.4	Future Work	157
APPENDICES		160
BIBLIOGRAPHY		172

LIST OF FIGURES

Figure

2.1	Historical U.S. energy consumption trends	7
2.2	Renewable energy consumption by source in 2010	9
2.3	World energy consumption from 1995-2035	11
2.4	2009 U.S. greenhouse gas emissions	12
2.5	CO ₂ emissions by fuel type	13
2.6	Global carbon cycle	15
2.7	Historical trends of CO ₂ concentration and global temperature . . .	16
2.8	Surface temperature trends from 1880-2006	17
2.9	U.S. sea level trends from 1900-2003	18
2.10	Climate model predictions of CO ₂ concentrations from 2000-2100 . .	20
2.11	Long-term predictions for global surface warming from 1900-2300 .	20
2.12	Sea level changes from 1800-2100	21
2.13	Schematic diagram of carbon capture and sequestration technology .	25
3.1	The reaction rate coefficient of ion-ion recombination in air as a function of pressure	37
3.2	Electronic excitation methods of dissociation	40
3.3	Configurations for capacitive discharges	43
3.4	Formation of a sheath along electrodes in a CCP	44
3.5	Possible configurations of ICP	45
3.6	Electric field intensity of the $m = 0$ surface wave as a function of radial position.	49
3.7	Relationship between plasma column length and input power	51
3.8	Energy level diagram of CO ₂	53
3.9	Electronic excitation energy efficiency	54
3.10	Equilibrium molar fraction products of CO ₂ dissociation in thermal discharge	55
3.11	CO ₂ electron impact rate coefficients	56
3.12	Vibrational modes of CO ₂	57
3.13	Catalytic effects on activation energy	59
3.14	Illustration of surface adsorption	60
3.15	Plasma/catalyst configurations	62
3.16	CO ₂ conversion in an alumina-packed corona discharge	64

4.1	Experimental setup of helicon system	68
4.2	Diagram of RGA chamber	69
4.3	RGA data collection	70
4.4	Output plasma species flow rate with $\vec{B} = 0$	71
4.5	Magnetic field effects of CO production	73
4.6	Efficiencies of CO ₂ dissociation over all flow rates	75
5.1	Energy efficiency of CO ₂ dissociation in various discharges	80
5.2	Efficiencies of CO ₂ dissociation in a microwave plasma at 120 torr	81
5.3	Experimental results of a non-thermal surface wave plasma operating at atmospheric pressure	82
5.4	Microwave plasma setup	84
5.5	Diagram of <i>Surfaquide</i>	85
5.6	Optical and IR transmission of the cooling fluid	88
5.7	Discharge tube with cooling jacket	89
5.8	Mounting of catalyst material into discharge tube	90
5.9	CO ₂ conversion efficiency for 2.5% CO ₂ in He mixture	91
5.10	CO ₂ dissociation energy efficiency for 2.5% CO ₂ in He mixture	92
5.11	RGA calibration curve for capillary configuration	94
5.12	Optical emission spectroscopy setup	95
5.13	Relative vs. corrected spectrum of the C ₂ Swan Band	96
5.14	Comparison of SPECAIR spectrum to experimental spectrum	97
5.15	Diagram of GlobalKin modules	100
5.16	Plug flow diagram	105
5.17	Power deposition profile	106
6.1	Pure Ar normalized emission spectrum at 1 kw	109
6.2	Normalized Ar/CO ₂ emission spectra at 1 kw	110
6.3	Pictures of plasma with 700 W input power	111
6.4	RGA background scans for air and Ar	112
6.5	Ar/CO ₂ RGA scan for 8 slm Ar and 4 slm CO ₂	113
6.6	CO and O ₂ production as a function of power	114
6.7	CO production as a function of Ar flow	115
6.8	CO production as a function of CO ₂ flow	116
6.9	Energy efficiency of CO ₂ dissociation	117
6.10	Conversion efficiency of CO ₂ dissociation	118
6.11	Effects of T _r on SPECAIR spectrum	119
6.12	Effects of T _v on SPECAIR spectrum	120
6.13	Effects of T _{el} on SPECAIR spectrum	121
6.14	Plasma temperature results from SPECAIR simulations	122
6.15	Energy efficiency of CO ₂ dissociation with uncoated monolith	126
6.16	Conversion efficiency of CO ₂ dissociation with uncoated monolith	127
6.17	Plasma/monolith temperature results from SPECAIR simulations	128
6.18	Energy efficiency of CO ₂ dissociation in the plasma/catalyst system	129
6.19	Conversion efficiency of CO ₂ dissociation in the plasma/catalyst system	130
6.20	Plasma/catalyst temperature results from SPECAIR simulations	131

6.21	Computational conversion efficiencies for Ar flow rate of 10 slm, CO ₂ flow rate from 1-8 slm , and 1-2 kW of power	132
6.22	Computational energy efficiencies for Ar flow rate of 10 slm, CO ₂ flow rate from 1-8 slm , and 1-2 kW of power	133
6.23	Computational electron temperature	134
6.24	Computational gas temperature	135
6.25	Computational electron density	136
6.26	Computational results for operating conditions outside the experimental test plan	137
6.27	Summary of efficiency results for all three experiments	139
6.28	Summary of T_{el} results for all three plasma experiments	140
6.29	Summary of T_v results for all three plasma experiments	141
6.30	Summary of T_r results for all three plasma experiments	141
6.31	Computational efficiency results including surface reactions	145
C.1	Tabulated empirical values for CO ₂ gas phase reactions	168
D.1	Energy level diagram of atomic oxygen	170
D.2	Potential energy curves for O ₂	171

LIST OF APPENDICES

Appendix

A.	Description of Hönl-London Factors	161
B.	GlobalKin Modeled Reaction Species and Mechanisms	162
C.	Tabulated Empirical Values for CO ₂ Reactions	167
D.	Excited Oxygen Energy Levels	169

LIST OF ABBREVIATIONS

RF	radio-frequency
MW	microwave
CCS	carbon capture and storage
OECD	Organization for Economic Cooperation and Development
GHGs	greenhouse gases
IPCC	Intergovernmental Panel on Climate Change
SRES	Special Report Emissions Scenarios
EM	electromagnetic
NTP	non-thermal plasma
CCP	capacitively coupled plasma
ICP	inductively coupled plasma
IPC	in-plasma catalysis
PPC	post-plasma catalysis
CTF	Cathode Test Facility
PEPL	Plasmadynamics and Electric Propulsion Laboratory
RGA	residual gas analyzer
TEM	transverse electromagnetic
TE	transverse electric
TM	transverse magnetic
PDMS	polydimethylsiloxane

OES optical emission spectroscopy
EEDFs electron energy distribution functions
ODE ordinary differential equation
MS mass spectrometry
VT vibrational-translational
sccm standard cubic centimeter per minute
slm standard liter per minute
FWHM full width at half maximum

CHAPTER I

Introduction

1.1 Motivation

Overwhelming scientific evidence has shown that human activities are changing the composition of the earth's atmosphere to include increasing amounts of greenhouse gases, such as carbon dioxide (CO₂). It is well understood that the burning of fossil fuels, the world's primary source of energy, causes the emission of CO₂ and that levels of atmospheric CO₂ have dramatically increased since the industrial revolution. Increasing concentrations of CO₂ that remain trapped in the atmosphere contribute to global warming by re-radiating energy from the sun back to the earth's surface, preventing radiation from escaping the atmosphere. This effect leads to a global warming trend which has been documented over the last century to show an increase in surface temperature of about 1 - 1.7°F [49]. This change in global temperature may seem trivial, but in reality it can have drastic effects on the earth's physical and biological systems.

The threat of climate change cannot be treated as an individual problem, however. It is uniquely intertwined with the energy crisis and the two must be faced as a joint effort. As of 2008, approximately 84% of world energy consumption was supplied by fossil fuels [21]. Here in the United States, which can be considered a world leader in innovative energy research, only about 8% of energy is generated from renewable

sources. Given the continuing and increasing world reliance on fossil fuels, CO₂ emissions will likely only increase as well and it remains imperative to find ways to mitigate the effects on climate change.

Some of the U.S initiatives for CO₂ mitigation involve federal tax incentives, a carbon capture and storage (CCS) system, and increasing energy efficiency for processes across all sectors. The tax incentives, as part of the American Recovery and Reinvestment Act of 2009, are designed to encourage individuals and businesses to reduce their overall energy consumption. For example, homeowners who make energy efficient improvements and install energy efficient appliances and equipment, as well as individuals who purchase electric vehicles, are eligible for a tax credit. Businesses that use renewable energy sources such as wind to power facilities can receive a tax credit, or they can apply for renewable energy grants which provide 30 percent of the investment in a qualified renewable energy facility. CCS is technology designed to remove CO₂ emissions from stationary sources, specifically targeting coal-fired power plants. First the CO₂ is separated and captured from flue gas streams, then the CO₂ is compressed and transported via pipeline to be stored in geological formations. Efforts are also being made to increase energy efficiency for processes in sectors such as transportation, buildings, and industry. Automobile manufacturers are focused on constructing more fuel efficient vehicles, hybrid vehicles, and cleaner diesel engines. Buildings are now being designed to include efficient lighting technology as well as more efficient electrical appliances and heating and cooling devices. Industry is utilizing more efficient end-use electrical equipment and is increasing material recycling. These efforts have helped raise awareness to climate change and demonstrate that this is a multifaceted problem without one single solution [48].

Given that fossil fuels will remain a part of the energy equation for many years to come, it is necessary to find an alternative way to get rid of the resulting environmentally harmful emissions. Plasma-assisted CO₂ dissociation offers one possible solution

to reduce concentrations of the greenhouse gas. This technology can be combined with CO₂ capture technology; instead of storing captured CO₂ in geological reservoirs, plasma can be used to break down the molecule to create carbon monoxide (CO) and oxygen, essentially mitigating its effects on climate change. Collisions with charged species created in the plasma provide an environment for dissociation to occur.

Experimental investigations have reported the successful dissociation of CO₂ in various plasma systems such as dielectric barrier discharges [113], microwave discharges [74, 101], and glow discharges [107, 110]. In particular, low temperature plasmas operating under vacuum are especially capable of achieving high energy efficient dissociation, which is a key component to scaling up the technology for industrial-size applications. However these reported plasma systems have only managed small conversion rates of less than 20% and they require the use of a vacuum pump, causing losses in overall system energy efficiencies [37]. Therefore this technology has not been optimized for industrial use. It is necessary to study the dissociation processes at atmospheric pressure and to look at alternative ways of increasing conversion rate without sacrificing energy efficiency.

1.2 Aim of Research

This dissertation focuses on studying the efficiency of CO₂ dissociation in an atmospheric pressure plasma system. In particular, an atmospheric pressure microwave plasma source is designed and tested for this purpose, examining the energy cost of creating CO from CO₂. In addition, catalyst material is inserted into the post-plasma zone to examine its effect on the conversion of CO₂ to CO.

In order to determine the effectiveness of the system, an energy efficiency and conversion efficiency analysis will be given for the specific plasma process. A threshold value of efficiency will be developed as a condition to guide future studies of plasma systems for CO₂ treatment. A cost comparison to existing technological approaches

will also be given to put the current research method in a larger framework.

The plasma properties that affect CO₂ dissociation will also be experimentally studied in the atmospheric pressure microwave system. Properties such as plasma gas temperature, electronic temperature, and vibrational temperature can greatly influence the collisional behavior that leads to dissociation. Therefore such information will provide insight into the experimental results.

Lastly, a computational model will be used as a comparison for the experimental results and to provide additional information on plasma properties that cannot be obtained experimentally in the system studied for this dissertation. Electron temperature and electron density play an important role in the outcome of CO₂ dissociation and this model will give information on these values. The computational results in combination with the experimental results will provide a complete picture of CO₂ dissociation in the microwave plasma.

1.3 Dissertation Overview

This dissertation is presented to achieve the above stated aim in the following manner. Chapter II discusses the evidence supporting the energy and climate change challenges and the predictions for the future, citing CO₂ as one of the most dangerous global warming gases. Possible solutions to the overabundance of atmospheric CO₂ are offered, explaining how plasmas can be used for CO₂ mitigation. An overview of plasma systems is given in Chapter III, describing the collision processes that occur within a plasma that lead to efficient dissociation. The properties of radio-frequency (RF) and microwave (MW) plasma sources are discussed as well as reports on plasma/catalyst systems. A preliminary investigation of CO₂ dissociation in a low-pressure RF helicon source is presented in Chapter IV. The low energy efficient results from this experiment lead to the design and construction of an atmospheric pressure MW plasma/catalyst system shown in Chapter V. This chapter illustrates details of the experimental setup,

the diagnostics used, and a description of the computational program GlobalKin used to model the plasma system. Mass spectrometry and optical emission spectroscopy are the two main diagnostics used to determine plasma species concentrations and plasma properties, respectively. GlobalKin is used to complement the experimental work by computing the theoretical species densities and plasma properties such as electron temperature and density. Chapter VI illustrates the experimental results of the plasma alone as well as the plasma/catalyst system and compares the efficiencies achieved in both cases. The plasma properties are analyzed to provide insight into the dissociation mechanisms. A comparison to the computational results from GlobalKin simulations is also given. Finally, Chapter VII lays out the conclusions of this project and cites future work for continued efforts.

CHAPTER II

Background

As described in the introductory chapter, the energy and climate change challenges pose a serious threat to the environment and are the main motivation for this research. It is important to understand the scientific and historical significance of the problem and what steps have already been taken towards solutions in order to lay an appropriate framework for the research presented in this dissertation. Section 2.1 describes past and current energy usage trends and identifies the relationship between atmospheric CO₂ concentrations and fossil fuel use. Evidence to support the impact of carbon emissions on climate change is reported and future predictions are given. Efforts for CO₂ remediation are outlined in Section 2.2. Technological as well as public policy solutions are explained. In Section 2.3, conclusions are drawn from the current state of knowledge and plasmas are offered as an alternative solution.

2.1 Energy Crisis and Climate Change

2.1.1 Energy Challenge

The world's primary source of energy is derived from fossil fuels, a nonrenewable energy source formed from the remains of plants and animals buried millions of years ago. There is no fast or easy way to replenish the supply of fossil fuels once they are used up given the extended length of time needed to create them. Coal, oil ,

and natural gas are the three primary forms in which fossil fuels are produced and they account for 21%, 36%, and 25% of energy consumption, respectively [21]. This high reliance on fossil fuels combined with increasing world energy demand raises the question of whether the earth’s natural energy supply will be able to meet such demands in the future.

Since the industrial revolution U.S fossil fuel use, in particular petroleum and natural gas use, has dramatically increased. However for the past decade, U.S. energy consumption has remained almost constant. Figure 2.1 illustrates the historical trends of energy consumption to support these claims. Because of efforts to reduce energy usage and to produce more energy efficient products, in combination with the recent economic recession, the U.S. has been able to halt the increasing trend of energy demand. However the U.S still accounts for 20% of total world energy demand, with the majority of energy consumption from fossil fuels.

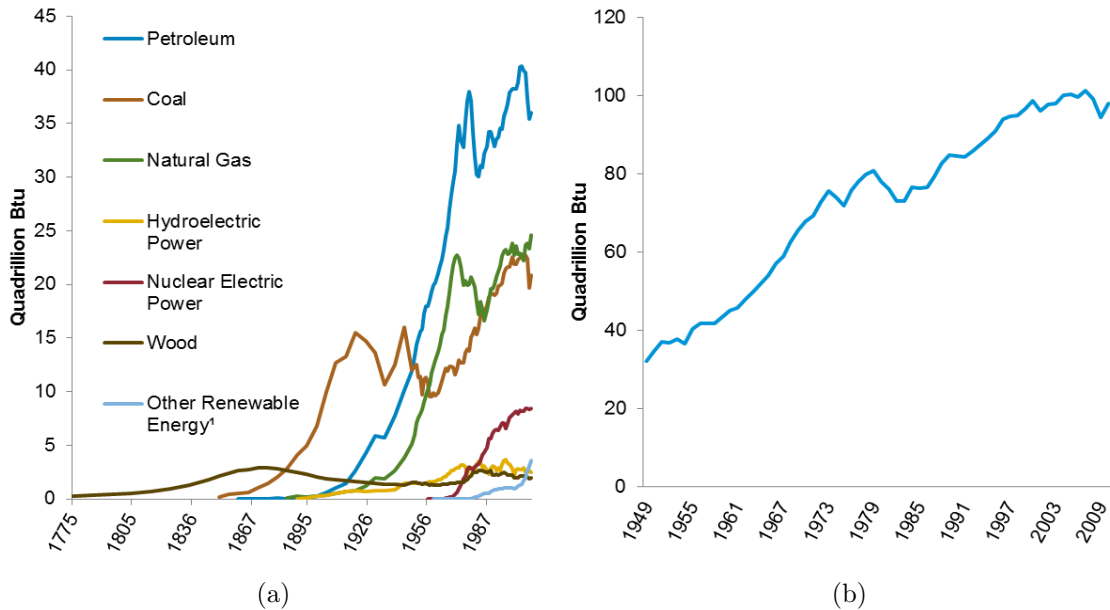


Figure 2.1: Historical U.S. energy consumption trends: (a) U.S. Energy Consumption by source from 1775-2010. (b) U.S. total energy consumption from 1945-2010. [21]

Part of the dependence on fossil fuels is due to its availability as a resource. Coal’s natural abundance in the U.S. as well as its relatively low cost has made it a consistent

and primary energy source. The U.S. has the world's largest recoverable coal reserves, with enough coal to last an estimated 200 years based on current consumption trends. Almost all of the coal-produced energy is used in the electric power sector, with coal supplying nearly half of all the country's electricity [29]. Natural gas is another abundant energy source found in the U.S. with only 9% of total consumption originating from imports, largely from Canada [30]. Natural gas has a much wider range of usage, in areas such as the electric power, industrial, residential, and commercial sectors. Currently more than half the homes in the U.S. use natural gas as the main heating fuel, and it is also used to produce steel, paper, clothing, and electricity. Petroleum, the third primary nonrenewable energy source, is the least plentiful of the three in the U.S. Despite the fact that the U.S. is the third largest crude oil producer, half of U.S. petroleum demands are met by imports, chiefly from Canada and Saudi Arabia [25]. The transportation sector accounts for 2/3 of petroleum use, with 2/3 of that from gasoline. Other uses of petroleum include residential and commercial heating, electric power generation, and as a raw material for creating products such as plastics. Though fossil fuels are clearly the dominant energy source, renewable and alternative energy sources still contribute to overall consumption.

Non-fossil fuel energy sources have begun to play an important role in the energy portfolio of the U.S. While alternative energy sources have been used for many years, they have now become the focus as a way to lessen dependence on nonrenewable fossil fuels. Nuclear energy currently provides about 20% of the country's electricity and about 8% of the total energy consumption [27]. Though other countries such as France and Japan may have a higher reliance on nuclear power, the U.S. has the world's highest capacity for nuclear power.

Renewable energy sources have a greater appeal because they can regenerate and be sustained nearly indefinitely. The most commonly used renewable energy sources are biomass, hydropower, geothermal, wind, and solar. Only 8% of U.S. energy

consumption is from renewable sources with over half of energy production expended for electricity generation, and the other half used for the production of heat and steam for industrial and residential purposes as well as for transportation [28]. Biomass, an organic material made from plant and animal waste, can be burned to produce energy in the form of heat and steam, or it can be converted to usable transportation fuels and methane gas. Hydropower is primarily used to generate electricity by using water flowing through a pipe to turn the blades of a turbine to spin a generator. Water and steam heated from processes in the earth’s core can be brought to the surface for electricity and heating purposes in the form of geothermal energy. Wind turbines collect the kinetic energy of the wind to produce electricity. The conversion of solar energy to thermal energy through the use of photovoltaic devices and solar thermal/electric power plants can create heat and electricity. Figure 2.2 shows the contribution of each renewable energy source to the total U.S. renewable energy consumption of 8 billion Btu’s in 2010.

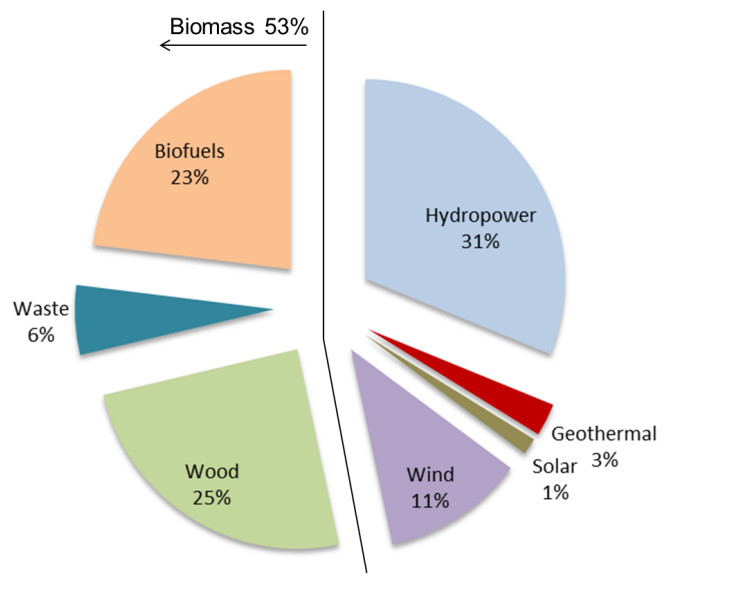


Figure 2.2: Renewable energy consumption by source in 2010 [21].

While the U.S. is making efforts to reduce fossil fuel consumption and overall

energy demand, not all countries are following the same path. Countries outside of the Organization for Economic Cooperation and Development (OECD), labeled as non-OECD¹, are expected to dramatically increase their energy consumption. According to the Energy Information Administration's 2011 International Energy Outlook, OECD countries are expected to increase energy use by 18% from 2008 to 2035, whereas non-OECD countries have a projected increase of 85%. In particular, China and India are expected to account for more than half of world energy growth by 2035, shown in Figure 2.3a. As of 2009, China had already surpassed the U.S. as the largest world energy consumer. The combination of high populations and the prediction for strong economic growth for both countries equates to an ever increasing energy demand from China and India.

In order to meet this demand, energy production must increase as well. Though fossil fuels are still expected to provide the vast majority of energy needs, renewable energy is predicted to be the fastest growing energy sector as shown in Figure 2.3b. Despite the rise in renewable energy technology, China, India and other non-OECD Asian countries will have a larger reliance on coal because of the availability of coal reserves in that region as well as the fact that it is a less expensive energy source. Coal-fired power generation will be needed to sustain the growth in electric power and industrial processes in this region. While the economic cost of fossil fuels may be lower than renewable sources, the environmental cost of burning fossil fuels is significantly greater. CO₂ and other polluting greenhouse gases (GHGs) are emitted with the burning of fossil fuels, and these emissions will only increase as world energy demand increases.

Fossil fuels are made of hydrogen and carbon atoms, thus given the name hydro-

¹Current OECD member countries (as of September 1, 2010) are the United States, Canada, Mexico, Austria, Belgium, Chile, Czech Republic, Denmark, Finland, France, Germany, Greece, Hungary, Iceland, Ireland, Italy, Luxembourg, the Netherlands, Norway, Poland, Portugal, Slovakia, Slovenia, Spain, Sweden, Switzerland, Turkey, the United Kingdom, Japan, South Korea, Australia, and New Zealand. Israel became a member on September 7, 2010, and Estonia became a member on December 9, 2010, but neither country's membership is reflected in IEO2011 [26].

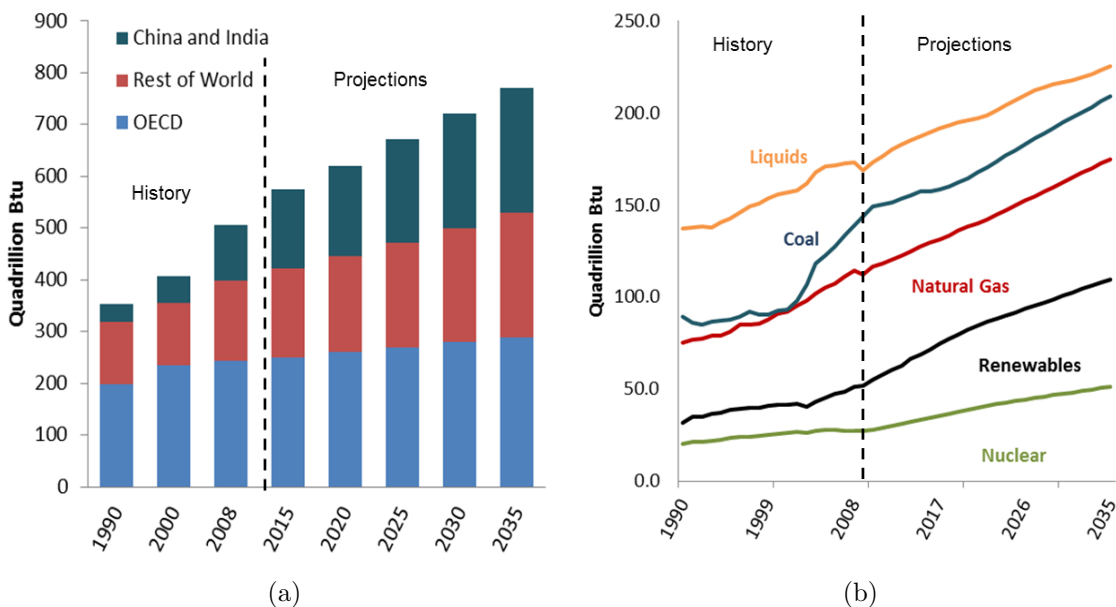
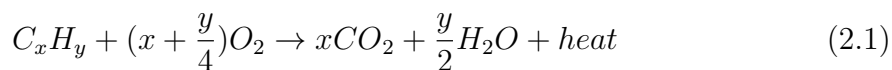


Figure 2.3: World energy consumption from 1995-2035: (a) projected world energy consumption by region. (b) projected world energy consumption by energy source. [26]

carbons. The combustion of hydrocarbons results in the release of CO_2 as depicted in Equation 2.1. Energy-related CO_2 emissions account for 81% of the total anthropogenic carbon emissions [22].



Other harmful GHGs resulting from human practices include methane (CH_4), nitrous oxide (N_2O), and some man-made gases like hydrofluorocarbons (HFCs) and perfluorocarbons (PFCs). Methane is created in oil and natural gas operations, coal mines, landfills, and agriculture. Nitrous oxide is produced from hydrocarbon combustion, nitrogen fertilizers, and other industrial processes. HFCs and PFCs are created as byproducts and emitted as leakage in industrial processes. All of these gases contribute to the warming of the planet, but CO_2 has the greatest effect because it is produced in such large quantities due to the dependence on fossil fuels. Figure 2.4 shows the dominance of CO_2 emissions over the other GHGs listed.

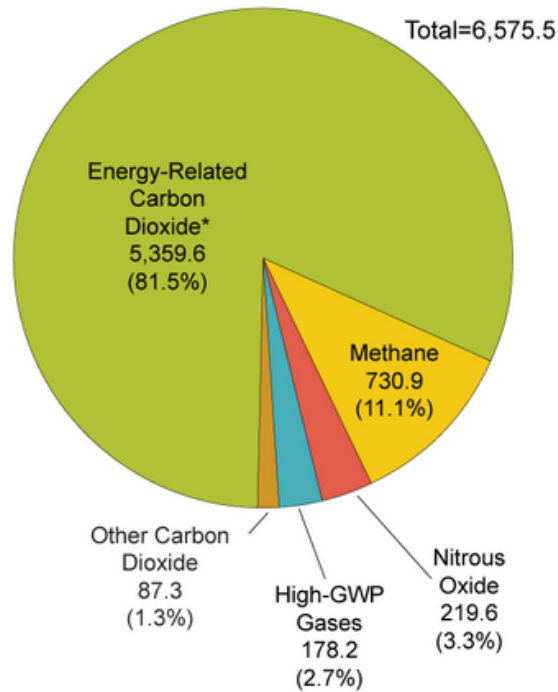


Figure 2.4: 2009 U.S. greenhouse gas emissions. Units are in million metric tons of CO₂ [22].

Different fossil fuels emit different amounts of CO₂ based on their hydrocarbon structure. In order to compare the contribution of CO₂ emissions across fuels types the amount of CO₂ emitted per unit of energy output or heat content can be used. The amount of energy a fuel produces is a function of the carbon and hydrogen content of the fuel. When combustion occurs, carbon and hydrogen combine with oxygen and heat is released. Figure 2.5 shows a comparison of different fuels with respect to their CO₂ production. Coal has the largest CO₂ to energy content, meaning that it releases relatively high amounts of CO₂ while producing low amounts of energy. Natural gas has the lowest CO₂ to energy content due to its primary composition of methane.

The U.S. has turned its focus on producing renewable energy technology because, unlike fossil fuels, the use of non-biomass renewable sources does not directly emit GHGs. However renewable energy is currently significantly more expensive and the specific energy source is not consistently available nor available in all geographic regions. When it is cloudy or when the wind is not blowing, there is no way to utilize

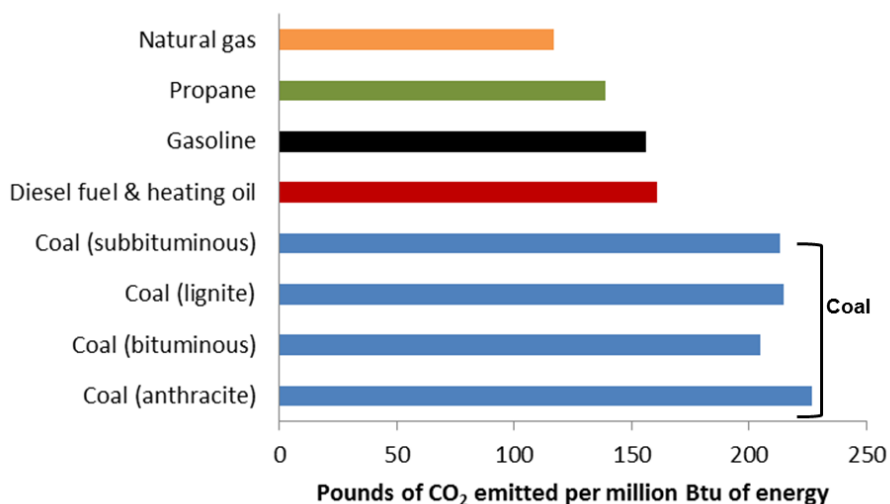


Figure 2.5: CO₂ emissions by fuel type [20].

the renewable sources of solar and wind power. The technology to harness large amounts of renewable energy in an energy-efficient way has yet to be presented. If renewable energy sources can become a greater share of the total energy outlook, the effects of climate change can hopefully be reduced.

2.1.2 Climate Change

Climate change is a global environmental challenge facing the world today [49]. As described in the previous section, the majority of anthropogenic emissions of CO₂ are created from burning fossil fuels. This has caused an overabundance of CO₂ in the atmosphere which has had a non-trivial effect on global climate. Climate change is considered any significant changes in the factors that make up climate such as temperature, precipitation, and wind over periods of time lasting decades or longer.

GHGs affect climate change by trapping heat in the atmosphere. More specifically, GHGs first allow ultra-violet (UV) radiation from the sun to pass through the atmosphere unimpeded to reach the earth's surface. As some of this energy is absorbed into the surface, infrared (IR) radiation is reradiated back out to the atmosphere where it becomes absorbed by the GHGs. The bonds of GHG molecules like CO₂

bend and vibrate when IR radiation strikes the molecule, allowing it to absorb some of the energy and consequently reradiate this energy via vibrations in all directions. This prevents all of the radiation from escaping and causes a general heating of the atmosphere known as the greenhouse effect [68].

The greenhouse effect is a physically occurring phenomenon due to the natural production of gases in the atmosphere. This effect actually stabilizes the temperature of the earth and makes the earth's climate suitable to sustain life. Without the greenhouse effect, the earth would be about 60°F cooler [24]. The most abundant GHG is water vapor. Water vapor is a critical gas in understanding the future effects of climate change because it creates a feedback loop of increasing temperature. As atmospheric temperatures rise, more water will evaporate from surface stores like lakes and rivers, and since the air is warmer it will be able to hold more water vapor as well. With more water vapor in the atmosphere, more radiation from sunlight will be absorbed and reradiated back to the surface. This causes atmospheric heating which in turn causes more water to evaporate, leading to a feedback system. Therefore the contributions of water vapor to climate change are complicated and hard to predict. Other naturally occurring GHGs are CO₂, methane, nitrous oxide and tropospheric ozone, while chlorofluorocarbons are all man-made. Atmospheric concentrations of these GHGs have all been affected by human intervention since the industrial revolution.

Concentrations of CO₂ in particular have been greatly affected by the burning of fossil fuels. The earth has natural sources and sinks that make up the carbon cycle and this flux of carbon has remained in equilibrium until the contribution of anthropogenic CO₂ emissions. Figure 2.6 shows the exchange of carbon between the atmosphere, land, and oceans, which is dominated by natural processes like plant photosynthesis. However the increase of CO₂ production from human intervention has created an imbalance in the natural cycle such that more carbon is being emitted into

the atmosphere than can be absorbed by nature. This imbalance results in climate change.

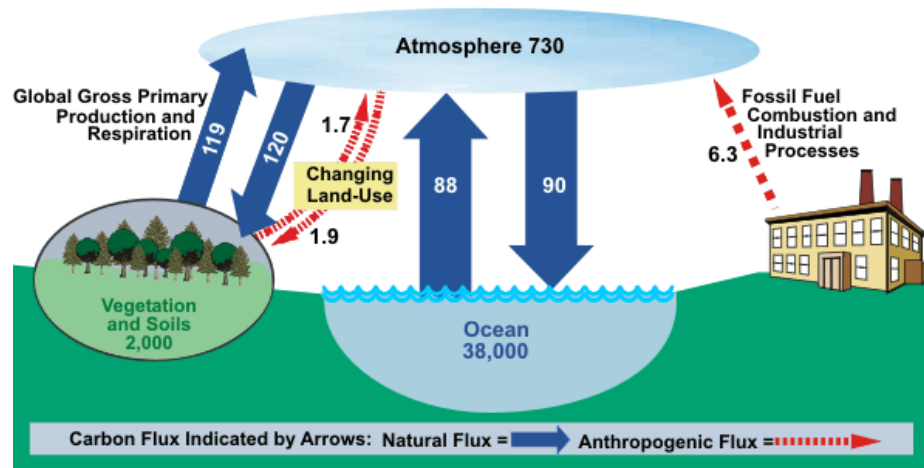


Figure 2.6: Global carbon cycle in units of billion metric tons of CO₂ [47].

Evidence in climate change can be found in measurements of various climate parameters like surface temperature, sea level, arctic ice and glaciers, tree rings, and ocean acidification. Scientists have been able to put together a map of the earth's climate history dating back thousands of years by analyzing a number of surrogate measures (e.g. tree rings, ice cores, boreholes, etc.) that can then be compared to today's data. Such analysis has found that while there have always been fluctuations in climate throughout history like ice ages followed by periods of warming, the fluctuations today are of a greater magnitude.

Figure 2.7 displays the estimates for fluctuations of temperature and CO₂ concentrations for the past 649,000 years. The trend clearly shows a correlation between higher CO₂ concentrations and higher temperatures. It also shows that record levels of CO₂ concentrations have been measured over the past century, suggesting that a greater than average warming period will follow. Past changes in CO₂ concentrations could be attributed to changes in the earth's orbit, changes in the sun's intensity, and volcanic eruptions. These periods of warmth also trigger feedback effects because as temperatures rise, more CO₂ is released from the oceans. Because CO₂ is a greenhouse

gas, higher concentrations of CO₂ in the atmosphere will lead to more warming, therefore making it difficult to predict the extent with which CO₂ concentrations will impact climate change. Despite this, it is clear that CO₂ concentrations have risen since the industrial revolution, and scientists are confident that the global average temperature during the last few decades has been warmer than any comparable period during the last 400 years [32].

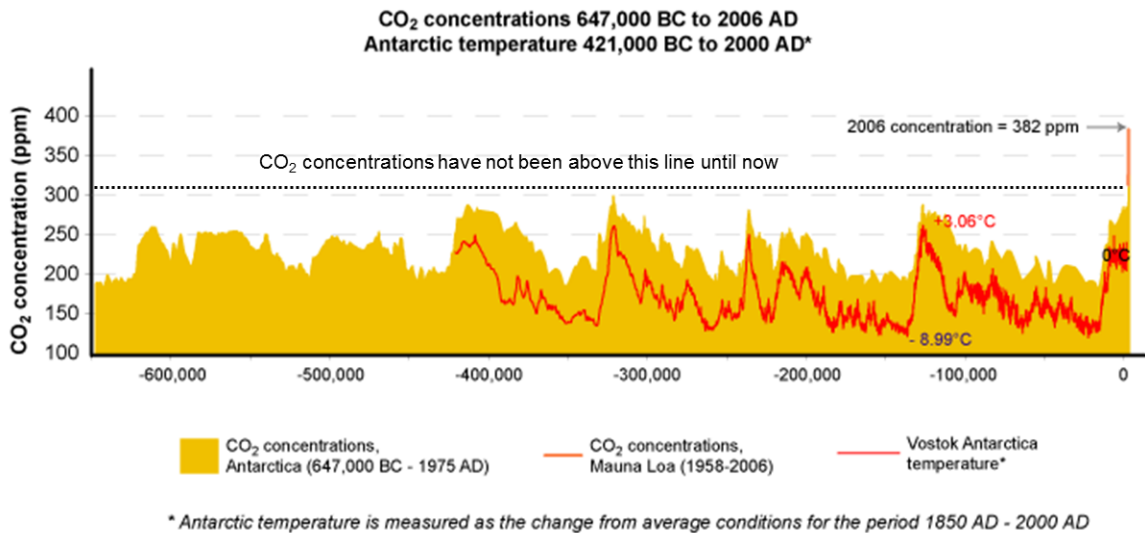


Figure 2.7: Historical trends of CO₂ concentration and global temperature. The red line represents fluctuations in temperature while the yellow portion represents CO₂ concentrations [32].

More recently, the Intergovernmental Panel on Climate Change (IPCC) concluded in 2007 that warming of the climate is now considered unequivocal. This determination is based on a number of observations including rising global temperatures, increased ocean acidification, and changes in global average sea level as well as precipitation and storms. Data taken of surface temperatures from land stations and ships has been compiled from 1880-2006 in Figure 2.8. Since 1970, global surface temperature has risen about 0.6°C (equivalent to about 1°F) and is currently warming at a rate of 0.29°F/decade [34]. Ocean acidification has also increased by about 0.1 units, equating to about a 30% increase in hydrogen ions, since pre-industrial times due to increasing CO₂ emissions. The atmosphere and ocean are constantly exchanging

CO₂, and as atmospheric CO₂ concentrations increase, the oceans begin to absorb more CO₂. Increased acidification results in a lower carbonate ion concentration of seawater, affecting coral and other marine calcifiers [49].

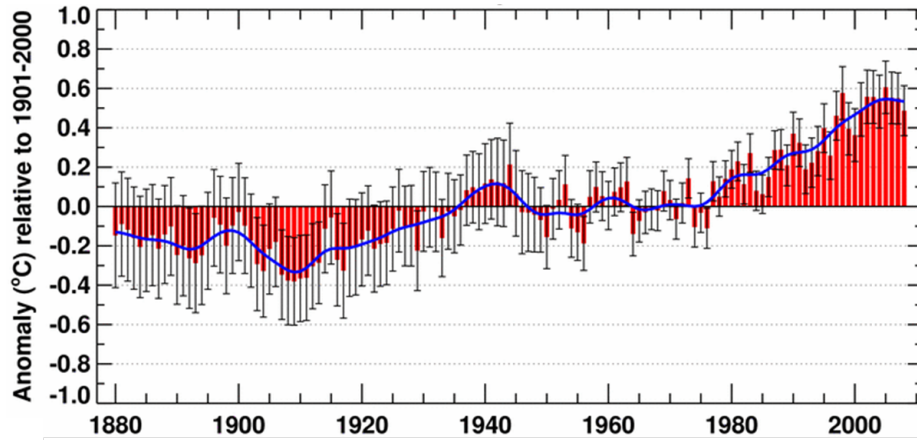


Figure 2.8: Surface temperature trends from 1880-2006 [34].

Changes in sea level across the globe have been measured at rises between 4.8-8.8 inches during the 20th century. Factors that influence sea level include the expanding ocean water for warmer ocean temperatures, the melting of glaciers and ice caps, and the melting of ice sheets. The rise in sea level has not been uniform across regions. In the U.S. sea levels have risen above average near Louisiana due to land sinking, and sea levels have dropped near Alaska due to land rising. Figure 2.9 show the trends in sea level across various regions in the U.S. Except for the Alaskan coast, all trends show rising sea levels from 1900-2003. The warming trend has also led to increases in average global precipitation. While precipitation trends vary widely by region with some areas actually becoming drier, in general it has become wetter in regions north of the 30°N latitude from 1900-2005. The World Meteorological Organization has been studying the effects of global warming on extreme storm events like hurricanes, tornadoes, hail storms, and thunderstorms. There is a natural variability in storm frequency and intensity which makes it hard to determine if the warming of the oceans has played any part in recent storm seasons. However, the Atlantic storm season of

2005 which set a record of 27 named storms has brought much attention to finding a link between changes in storms and changes in climate. As of now, the studies are inconclusive [33].

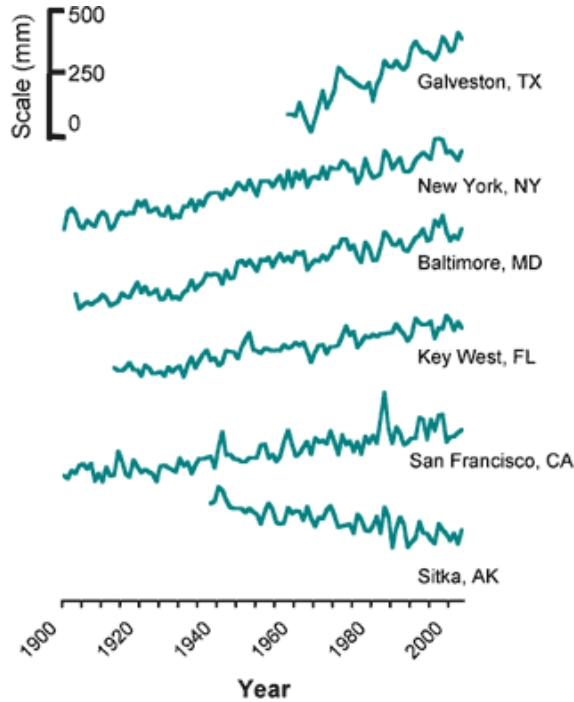


Figure 2.9: U.S. sea level trends from 1900-2003 [33].

2.1.3 Predictions for the Future

Atmospheric levels of CO_2 will continue to rise in the future unless carbon emissions are significantly decreased through technological or legislative means. This will most likely cause a continual rise in global temperature, but the extent to which this will affect climate change is difficult to determine. There are several variables involved in the calculations that affect climate change predictions such as estimates of future GHG concentrations, the amount of response climate features will have to variations in GHG concentrations, and the climate's response to natural inconsistencies like the sun's intensity, volcanic activity, and changes in orbit. These diverse and complex variables make accurate climate modeling a difficult task. However climate models have shown

the ability to model current and historical climate changes, giving confidence to their future predictions. Thus, climate modeling can provide important contributions to our understanding of future climate change.

In order to accurately predict the magnitude and speed of climate change, certain assumptions must be made for global population size and energy use, and the potential effects of government intervention and legislation should be considered. Therefore different scenarios can be modeled based on these assumptions. The IPCC has developed several such scenarios to cover a wide range of driving forces for future emissions of all relevant GHGs, though none of the scenarios include policies that specifically address climate change. There are four 'families' of scenarios (A1, B1, A2, B2) that branch out into six groups of scenarios (A1FI, A1T, A1B, A2, B1, B2), which will be explained here for reference in Figures 2.10 and 2.11. The A1 family models a future with rapid economic growth coupled with new technologies and a population that peaks mid-century. The three groups within the A1 family represent scenarios that are fossil fuel intensive (A1FI), balanced (A1B), or predominantly non-fossil fuel (A1T) [46]. The A2 family describes a heterogeneous world with slower growth and change. B1 follows a similar story to A1, but with an emphasis on global sustainability and energy efficiency. B2 focuses on slow growth with diverse technological change and an emphasis on regional environmental protection practices.

Future GHG emissions are one of the most important factors in determining the extent of future climate change. The IPCC Special Report Emissions Scenarios (SRES) has developed several long term models to predict changes in CO₂ concentrations through the 21st century based on changes in emissions, shown in Figure 2.10. In all scenarios modeled, CO₂ concentrations will continue to rise until the year 2100, with concentrations increasing between 41 and 158% compared to present levels. The A1FI scenario results in the highest concentration of CO₂, which should be expected since it models a fossil fuel intensive future. Given the predicted rise in CO₂ concentrations,

there is also a predicted rise in global surface temperature. Though estimates for future temperatures do not only depend on emissions concentrations, but are also affected by positive and negative feedback systems induced by the already present warming, making it difficult to model. Four different scenarios are shown in Figure 2.11 of predictions for future surface warming. Even in the constant-concentration commitment scenario in which concentrations are held fixed at year 2000 levels, surface temperature will continue to warm due to past emissions that remain in the atmosphere decades later and for heat absorbed by oceans that has not yet been realized. On average, surface temperature is expected to rise 3.2 to 7.2°F by the year 2100.

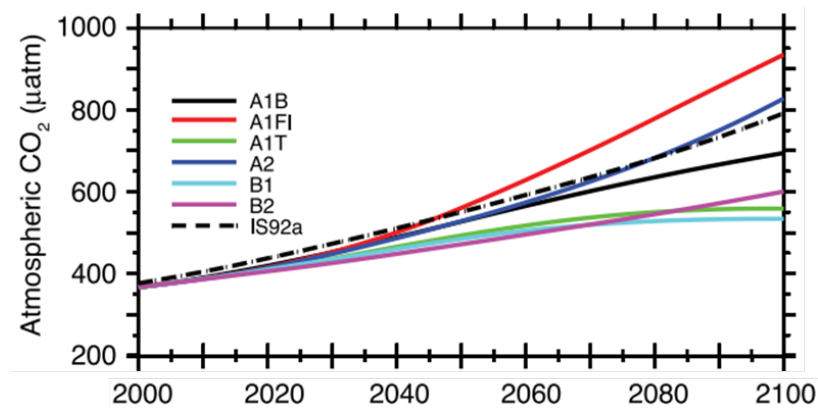


Figure 2.10: Climate model predictions of CO₂ concentrations from 2000-2100 [49].

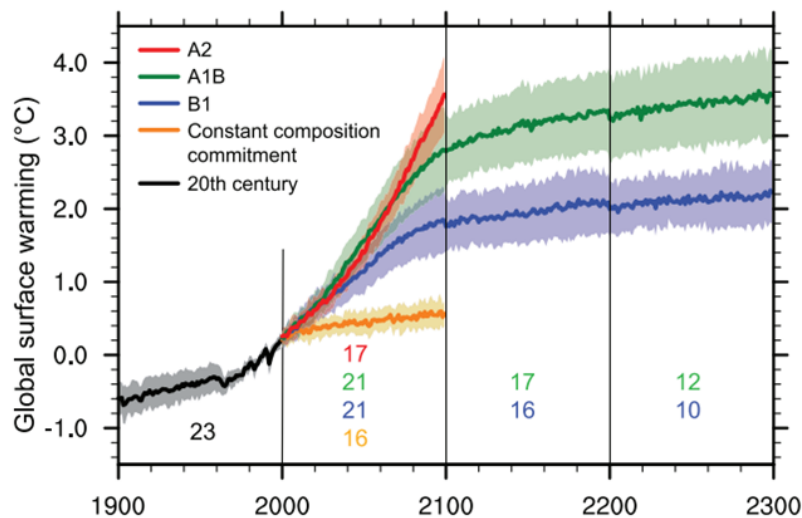


Figure 2.11: Long-term predictions for global surface warming from 1900-2300 [49].

Changes in sea level and ocean acidification are also considered in the IPCC SRES report. As temperatures are expected to rise, the oceans will expand, mountain glaciers and ice caps will melt, and the Greenland and Antarctic ice sheets may also begin to melt, leading to a global rise in sea level. Figure 2.12 shows the past and projected global average sea level based on the medium growth emission scenario A1B. By the year 2100, global sea level could rise by 7.2 to 23.6 inches [49], having a profound effect on low-lying coastal areas by intensifying flooding, eroding beaches, and increasing salinity of rivers and bays. Increased ocean acidification is a direct effect of increased CO₂ emissions, as the oceans continue to absorb more of the over-abundant concentrations. Ocean pH levels may decline up to 0.5 units if human activities continue on in the present trend [49]. As ocean acidification increases, the availability of calcium carbonate minerals will decline causing significant impacts on the ecosystem structure and productivity of marine life. The effects of acidification can also extend to future climate change, as the ocean’s capacity to absorb increasing CO₂ concentrations will decline.

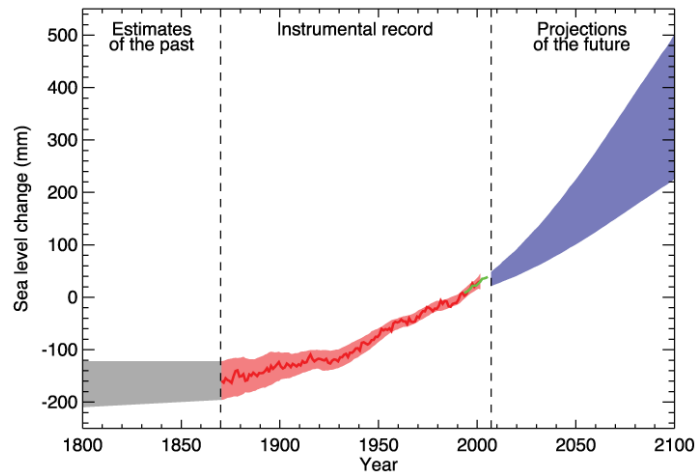


Figure 2.12: Sea level changes from 1800-2100 [49].

While the effects of climate change over the next century are not entirely certain, it is clear that if the current trends of CO₂ emissions continue as ‘business as usual’ there will be significant global environmental changes. The models used in the IPCC

SRES report do not take into account any direct legislative action to reduce CO₂ concentrations, so the possibility of CO₂ regulation policies could help reduce the future outlook. Near future technological advances could also help lessen the threat of climate change, as the world's leading scientists are now actively pursuing possible solutions to this problem.

2.2 CO₂ Remediation Efforts

2.2.1 Policy Efforts

There are several approaches to minimize CO₂ emissions through government policy. For example, a carbon cap and trade system has been proposed to manage emissions. In this system, policymakers would create a new commodity by limiting the amount of CO₂ emissions allowed during a given period. A certain number of allowances would be admitted for the set cap on emissions and participating entities, like fossil fuel burning power plants, would be able to buy and sell such allowances [99]. While this policy may help limit the number of emissions and encourage industry to upgrade equipment to green technologies, ultimately the cost burden will fall on consumers. Consumers will be subject to persistently higher prices for products like electricity and gasoline. A similar result could occur if a carbon tax is imposed. This policy would require the entities that emit GHGs to pay a fine for every tonne of GHG released. This charge would be a set fee per unit of GHG that would be uniform across all industries and would provide incentive for polluters to implement emissions reductions technology. However this system does not put any cap on emissions, and it allows emitters to weigh the cost of emissions control against the cost of paying the tax to determine the least expensive solution. If the tax is to be used to set a limit on emissions, it will have to be adjusted over time to account for inflation, technological progress, and new emission sources [48].

Another way to encourage the use of emissions reductions technology is to provide technology and performance regulatory standards. These two classes of regulations would work together as the technology requirements would specify GHG abatement technologies to be used for production, while the requirements of performance would specify the environmental outcome desired per unit of product. The benefit of this method for pollution control is that it can be tailored to each industry taking into account any specific circumstances, unlike the industry-wide uniform policy changes mentioned previously. However the drawback is that it may also slow technological growth by removing any incentive to develop improved pollution abatement approaches [48]. It will also be difficult for the government to determine the appropriate amount of regulatory change that is possible at a reasonable economic cost. This could result in overly ambitious changes impossible to implement or overly weak changes that stunt technological advancement.

Financial incentives from tax credits and government subsidies can provide other means for emissions control. In the U.S., the American Recovery and Reinvestment Act of 2009 offers tax credits to individuals and businesses for making energy efficient and alternative energy investments. For example, homeowners are eligible for tax credits if they make energy efficient improvements to their home or if they install renewable energy equipment like solar water heaters and geothermal heat pumps. There are also tax credits for facilities generating electricity from renewable sources like wind power, biomass, geothermal, and hydropower, and businesses that use these renewable energy facilities are eligible for tax incentives, as well [43]. Government subsidies can be strong policy instruments for emissions control, but sometimes they may even increase emissions depending on their nature. Subsidies aimed at research and development for renewable energy and GHG abatement or price supports for renewable electricity tariffs can help decrease emissions. However subsidies that support industries that are sources of GHGs, like the fossil fuel sector, will only help to increase emissions.

Subsidies in OECD countries that support the fossil fuel energy industry are slowly being reduced and the focus is shifting to environmental sustainability and economic concerns [48].

2.2.2 Technological Efforts

Scientific research to reduce CO₂ emissions is aimed at capturing carbon directly at the source, called flue scrubbing. Flue scrubbing involves isolating CO₂ from other flue gases after combustion via a liquid solvent. Typically, the chemical absorption of CO₂ is done using an amine-based solvent, which results in 75% - 95% of CO₂ captured using this technology [5,19,94]. The process involves using an absorber where the CO₂ is removed, and a regenerator where the CO₂ is released and the solvent regenerates. This method has the potential to allow continued use of fossil fuels while significantly decreasing emissions. However, flue scrubbing requires a large amount of heat to regenerate the solvent and it needs low flue gas concentrations of SO₂ and NO₂ because they reduce the ability of the solvent to absorb CO₂. This process becomes very costly such that electricity generated at a coal plant with flue scrubbing can cost at least 50% more than electricity generated from a plant without it [19].

Complementary efforts to manage CO₂ emissions with carbon capture processes involve CO₂ conversion technology and carbon sequestration research. The former uses a photocatalyst for the conversion of CO₂ into hydrocarbons with the help of solar energy and water. The process has the potential of forming a useful carbon cycle, but requires an efficient photocatalyst that utilizes a maximum amount of solar energy. For this to be an effective solution the conversion rate must greatly increase and the technology must be made to scale the needs of industrial power plants [86,105]. The other option, carbon sequestration, involves storing CO₂ in geological and oceanic reservoirs. A diagram describing the carbon capture and sequestration process is shown in Figure 2.13. Conventional methods propose to inject

CO₂ into depleted oil and gas reservoirs for enhanced oil recovery, store CO₂ in deep underground saline formations, and inject liquid CO₂ into the ocean at intermediate depths. While technology is available for each of these methods, the financial costs to implement them run high when considering the energy needed to compress captured CO₂, transport it to storage reservoirs, and pump it into the ground or ocean. There is also great concern over the potential environmental impacts associated with leaks, slow migration and accumulation, induced seismicity, and ocean acidification [42]. As the ocean absorbs increasing amounts of CO₂, the pH will continue to drop as well as carbonate ion concentrations. The undersaturation of carbonate enhances the dissolution of calcium carbonate, having adverse effects on oceanic calcifying organisms such as corals, algae, and shellfish.

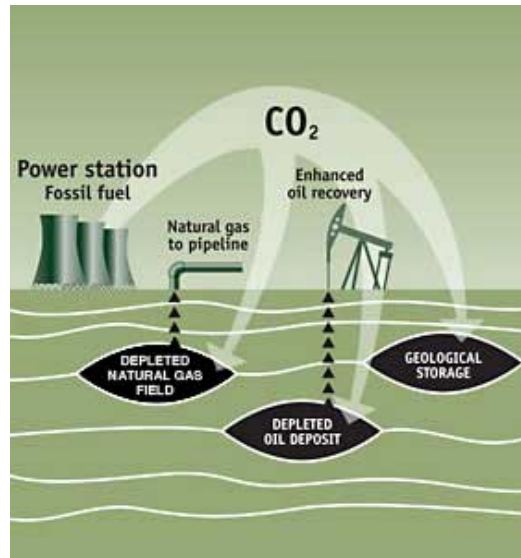


Figure 2.13: Schematic diagram of carbon capture and sequestration technology [53].

A less conventional approach to mitigate the effects of CO₂ on global warming is to manipulate the earth's climate via geoengineering. The main approaches include ocean modification for increased CO₂ absorption and atmospheric modification to decrease solar energy reaching the earth's surface. Research has shown that iron fertilization of oceans can increase phytoplankton bloom which naturally absorbs CO₂ from the atmosphere. However, adding large quantities of iron to the ocean could

potentially damage the biological food chain and it is unknown how much carbon will be stored or for how long. Methods for blocking solar energy involve injecting SO_2 into the stratosphere to scatter sunlight and launching a 'sunshade' in space to directly block sunlight from reaching the earth. The consequences of SO_2 injection is unknown but will most likely increase production of acid rain [57]. While these two solutions could have an immediate effect on cooling the planet, they fail to solve the root of the problem. If this method to block sunlight were to fail with CO_2 emissions left unchecked, mean global temperatures would dramatically increase. Therefore it is necessary to directly solve the problem through the reduction of emissions.

2.3 Conclusions

The evidence for climate change is vast and undeniable. The only uncertainty lies in the predictions for how quick and how severe the consequences will be known. Until the world's fossil fuel dependence is greatly decreased, CO_2 emissions will continue to rise causing potentially drastic effects on the environment. Technological and public policy remediation efforts are needed to help lower atmospheric CO_2 concentrations while fossil fuels remain the primary source of energy. Though policy efforts provide incentive for industry to invest in the reduction of emissions via technological improvements, some of the cost burden will ultimately fall on the consumer. The proposed technological efforts are primarily focused on manipulating the earth's natural resources for increased alternative storage and absorption options or to actually prevent solar radiation from reaching the surface of the earth. Any attempts to actually convert the CO_2 molecule to something less harmful using solar energy combined with catalysis is currently not cost effective. However, plasma processing of CO_2 could provide an alternative means of CO_2 conversion to produce gaseous products such as carbon monoxide, oxygen, and usable hydrocarbons. The highly energetic plasma electrons have the ability to efficiently excite and dissociate CO_2 via collisional processes, reducing anthropogenic

CO₂ emissions. This plasma technology could provide a means to continue burning fossil fuels without releasing harmful carbon emissions into the atmosphere.

CHAPTER III

Plasma Systems

Plasma processing and plasma chemistry techniques offer another possible solution to the climate change challenge. Plasma discharges can be selected to produce specific operational conditions of characteristic temperatures and charged species densities within the discharge that favor a given set of chemical reactions. With such a wide variety of plasma sources to choose from, it is necessary to first understand the fundamental properties and qualities of plasma to best identify the proper plasma discharge for a given process. Thus, Section 3.1 will provide a brief overview and description of general plasmas, describing the main physical processes that occur in a plasma as well as discussing two types of plasma generation, radio-frequency and microwave discharges. Section 3.2 will explain the specific mechanisms for plasma CO_2 dissociation and cite the plasma conditions required for the most efficient dissociation to take place. The emerging field of plasma/catalyst systems will be introduced in Section 3.3 to review the benefits and uses of catalyst material when combined with plasma systems, and specifically how catalysts may benefit CO_2 dissociation efficiency. Lastly, conclusions will be given in Section 3.4 summarizing the potential of plasmas for CO_2 conversion.

3.1 Overview of Plasmas

3.1.1 Introduction to Plasma

Plasma is the fourth state of matter and is simply defined as ionized gas. Thus, any gas can potentially become a plasma once energy is applied to create a significant density of electrons and ions. The average charge summed over the negatively charged species (electrons and negative ions) and positive ions are considered to be balanced in the bulk of the plasma, giving plasmas the characteristic of quasi-neutrality. Therefore despite the existence of charged particles, plasmas as a whole are considered neutral. Plasmas can occur naturally in the environment along with man-made plasmas generated in the laboratory. Some examples of plasmas in nature include solar flares, the earth's ionosphere, the aurora borealis, and lightning. Laboratory plasmas can be generated in a diverse range of conditions from very low vacuum pressures (10^{-9} torr) up to atmospheric pressure and above, with heavy particle (ions and neutral species) temperatures ranging from room temperature up to thousands of degrees Celsius. These properties make plasmas attractive for chemical and other industrial applications because they can generate temperatures that greatly exceed those of traditional chemical processes. Plasmas can create a significant concentration of excited and chemically active species. This can increase the intensity and efficiency of chemical reactions, which would be unachievable in conventional chemistry [37].

One of the fundamental parameters that characterizes a plasma is the temperature of plasma species. Each species in a plasma (i.e. electrons, ions, and neutrals) is usually defined by its own temperature associated with its distribution function. Typically energy is transferred to electrons via acceleration by an applied electric field, which in turn is transferred to heavy particles through collisional processes [37]. The electron temperature can be much higher than heavy particle temperatures, with an equilibrium temperature determined by collisions and radiative processes. Electron

and heavy particle temperatures may never equilibrate if the collision frequency is too low.

Plasmas in which the electron temperature (T_e) approaches the heavy particle translational temperature (T_0) are defined as thermal plasmas, with gas temperatures greater than 3,000 K. In the opposite case where $T_e \gg T_0$, the plasma is called a non-thermal plasma. For many non-thermal plasmas, the temperature relation is as follows: $T_e > T_v > T_r \approx T_i \approx T_0$ [37]. The electron temperature remains the highest followed by the vibrational temperature (T_v), both being higher than the rotational temperature (T_r) which is considered close in value to the ion temperature (T_i) and neutral heavy particle temperature. In these types of discharges, T_e is generally close to unity measured in units of electron volts or eV (equivalent to 11,600 K) with the gas temperature, T_0 , close to room temperature.

Another characteristic of plasma is particle density. As mentioned previously, there must be a significant number density of charged species for a plasma to exist; however the plasma does not need to be fully ionized. In a completely ionized plasma, the ratio of charged species density to neutral species density approaches one. This characteristic is called the ionization degree and is denoted by $n_{e,i}/n_0$ where $n_{e,i}$ is the electron and ion number density and n_0 is the neutral gas density [37]. These types of plasmas are present in nuclear fusion and stellar plasmas. Plasma discharges conventionally used to study plasma-chemical systems are considered weakly ionized. Here the ionization degree is around $10^{-7} - 10^{-4}$, meaning the neutral particle number density is several orders of magnitude higher than the charged particle number density [37].

While there may be variations in ionization degree in different plasmas, most plasmas tend to be quasi-neutral. This phenomenon occurs due to some basic electrostatic principles. Any charge separation that occurs between electrons and positive ions will generate an internal electric field, essentially accelerating the electrons in the direction of the ions and reducing any charge separation that may exist. Therefore

plasmas are considered quasi-neutral on large length scales greater than a few Debye lengths, also known as the sheath thickness [78]. The Debye length, or Debye radius as it is also referred, is the characteristic length scale by which a charged particle will be 'shielded' by particles of opposite polarity. For example, if a positive ion is inserted into an initially neutral and spatially uniform plasma system, a displacement of plasma electrons and negative ions will occur as they are attracted to the positive ion creating a charge cloud surrounding the particle. This charge cloud results in a shielding effect, partially canceling out the test particle potential [78]. This charge separation created by the positive ion and the negative charge cloud over the distance of a few Debye lengths produces a region of non-neutrality within the plasma. For Debye shielding to be relevant, the length scale must be small compared to the overall plasma dimensions, otherwise plasma particles would not exist outside of the Debye radius.

3.1.2 Collisional Processes in Plasmas

Now that the basic properties of plasmas have been described, the collisional processes that occur between charged and neutral species which are essential for plasma production and plasma chemistry will be discussed. In most weakly ionized plasmas, electrons are the primary energy carrier and are responsible for transferring energy to heavy particles via collisions. These collisional processes can become very complex when dealing with molecular plasmas due to the creation of various chemically active species such as excited atoms and molecules, charged particles, neutral species, and radicals. Each component of the plasma plays a role in the output of a given chemical process, and it is necessary to understand how collisions can be manipulated to achieve a desired result.

Before describing the different types of collisional processes, an explanation of how a collision is defined should first be identified. There are generally two classes of

collisions: elastic and inelastic. In elastic collisions between charged particles (typically a very light electron) and neutrals (a heavy particle), there is no change in the internal energies of the colliding particles and the electron simply scatters. However, when an electron succeeds in transferring energy and changes the internal structure of the neutral via ionization or excitation, this collision is called inelastic [78]. There are special cases when energy is transferred from an excited atom or molecule back into the kinetic energy of an electron; this is referred to as a superelastic collision.

The collision cross section along with the mean free path, collision frequency, and reaction rate coefficient are some of the parameters that define a collisional process. The cross section can be illustrated as a circular area of influence, σ , surrounding a collisional particle. When another particle breaches this region a collision is said to have taken place. The mean free path is the average distance a particle will travel before encountering a collision. The relationship between mean free path and cross section is given by Equation 3.1 where n_B is the number density of particle B with which a collisional process occurs [37].

$$\lambda = 1/n_B\sigma \tag{3.1}$$

The frequency of a collision, given by ν , is defined in Equation 3.2 with v representing the relative velocity between two collision partners A and B.

$$\nu_A = v/\lambda = n_B\sigma v \tag{3.2}$$

Once Equation 3.2 is averaged resulting in the relation $\nu_A = \langle\sigma v\rangle n_B$, the reaction rate coefficient can be defined as $\langle\sigma v\rangle$ [37]. This factor depends on energy distribution functions and the mean energies of collision partners, as shown in Equation 3.3. It provides a connection between micro- and macro-kinetic processes and can provide

insight into which collisional reactions will dominate in a given plasma.

$$\langle \sigma v \rangle = \int f(v) v \sigma(v) dv \quad (3.3)$$

3.1.2.1 Electron and Ion Production

Perhaps viewed the most essential collisional process, plasma ionization techniques will be described first given that it is the primary mechanism for electron production, and thus plasma production. The three main methods for ionization most relevant for the plasma systems discussed in this dissertation are direct ionization by electron impact, stepwise ionization by electron impact, and ionization by collision with heavy particles.

Direct ionization by electron impact indicates the collision of an electron with a neutral or unexcited atom or molecule that results in ionization. This process is usually found in non-thermal discharges where the electrons have a high enough energy to ionize a neutral ground state species in a single collision [37]. The transferred electron energy, $\Delta\epsilon$, must be sufficiently high to overcome the ionization potential of the valence electron of the participating species. When the participating species is a molecule, the ionization process may or may not result in dissociation. When non-dissociative molecular ionization occurs, as shown in Equation 3.4 for a diatomic molecule AB, the electron energy does not greatly exceed the ionization potential [37].

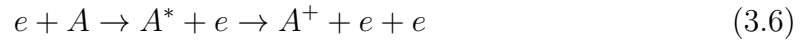


According to the Frank-Condon principle, the atoms inside a molecule can be taken as frozen during electron impact excitation processes. This is due to the fact that the even the fastest internal motions of an atom inside a molecule (vibrational motion) is still slower than the interaction time between electrons and molecules inside

a plasma, which takes place on the order of $10^{-16} - 10^{-15}$ seconds [37]. When the electron temperature is significantly higher than the ionization potential, an electron collision can result in dissociative ionization, displayed in Equation 3.5 [37].



Stepwise ionization by electron impact takes place via collision with an electron and an excited neutral. This process is relevant in plasmas with high ionization degree and high concentrations of excited neutral species, and requires multiple steps versus a single collisional event. First, energy is transferred to the neutral species via multiple electronic excitation incidents. Then a final collision with a low energy electron (energy lower than the ionization potential) can result in ionization as shown in Equation 3.6. Stepwise ionization can be more than 1,000 times faster than direct ionization and allows the final ionizing electron to have lower energy [37].



Finally, ionization by collision of heavy particles is a process describing interaction between ions and excited or ground state molecules. Due to the heavy mass of ions and neutrals and the consequently low particle velocity, they are usually unable to provide the energy required for ionization. However when a species gains electronic excitation energy through a previous collision with an electron, collision with another atom can result in ionization. This is termed Penning ionization (Equation 3.7a) [37]. Even if the combined electronic energy of the participating atoms is too low, associative ionization may still occur in which the participating atoms react to form an ionized molecule (Equation 3.7b) [37]. This reaction can only work for a select few species like mercury or nitrogen.





3.1.2.2 Electron and Ion Destruction

After this general introduction to the creation of electrons and ions, it is necessary to illustrate the processes by which they may be destroyed. Recombination, attachment, and detachment are the main mechanisms for the loss of charged particles. First electron-ion recombination will be reviewed, followed by ion-ion recombination. Then electron-neutral attachment will be considered, along with the related subject of electron detachment via electron-ion and ion-neutral collisions.

Electron-ion recombination can play an important role in plasma-chemical reactions because the recombination is a highly exothermic process [37]. Therefore this excess energy can be transferred to different channels such as molecular dissociation, the release of radiation, or to a third-body partner facilitating the reaction. Dissociative electron-ion recombination is the fastest method for electron destruction in a molecular plasma and follows from the reaction sequence of Equation 3.8 [37]. Here the released energy is used to dissociate the intermediate excited molecule and to excite the atomic product.



With relatively low plasma densities, radiative electron-ion recombination may occur, though the cross section for this process is not very high. Here the energy is converted to radiation as shown in Equation 3.9 [37].



Three-body electron-ion recombination may also occur in atomic gases where the energy is transferred to the third-party electron that participates in the reaction. This

is a more common electron-ion neutralization process for atomic gases.



Recombination processes between positive and negative ions are significant in plasmas containing electronegative gases such as oxygen and can have very high rate coefficients. The binary collision between a negative and positive ion releases energy which is used to excite a neutral product. This process dominates ion-ion recombination at low pressures [37].



The three-body ion-ion recombination reaction involving the presence of a heavy neutral is more common in high pressure discharges.



The pressure dependence of the reaction rate coefficient for the reaction shown in Equation 3.12 is displayed for air in Figure 3.1. The rate coefficient rises as pressure rises and then begins to decrease above atmospheric pressure as ion mobility drops.

Attachment is a process that removes a free electron while simultaneously producing a negative ion. This can occur in collisions between electrons and neutral atoms or molecules. In molecular gases, dissociative attachment is common if the resulting products have positive electron affinities, resulting in an endothermic reaction [37]. The attachment proceeds as in Equation 3.13 where an electron-neutral collision first creates an unstable excited negative ion which quickly decays leading to dissociation [37].



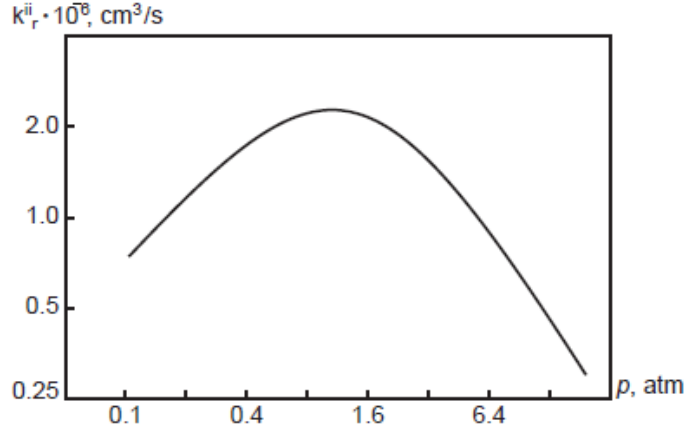


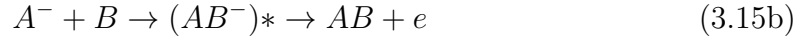
Figure 3.1: The reaction rate coefficient of ion-ion recombination in air as a function of pressure [37].

In the case of atomic gases, a three-body electron attachment can take place. This reaction is preferred at higher pressures and when electron energies are too low to cause dissociative attachment [37]. Unlike the previous process, this reaction is exothermic.



Detachment, a process analogous to attachment, results in the destruction of negative ions with the release of an electron. The detachment processes relevant to plasma-chemical processes take place in electron-ion collisions and ion-neutral collisions. Electron impact detachment shown in Equation 3.15a is pertinent in discharges of high ionization degree and high electron energy ($T_e > 10$ eV) [37]. Associative detachment is significant in non-thermal plasmas, displayed in Equation 3.15b [37]. Similar to Penning ionization, Equation 3.15c describes detachment in collisions with excited species [37]. The neutral atom or molecule can be electronically or vibrationally excited, and if its excitation energy exceeds the electron affinity of the participating negative ion, detachment will follow.





3.1.2.3 Neutral Dissociation and Excitation

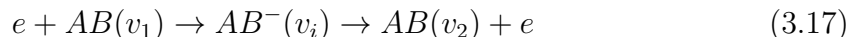
While the previous sections dealt specifically with the creation and destruction of electrons and ions, the following specifically addresses neutral species. The excitation and dissociation of neutral species play very important roles in generating active species to facilitate plasma-chemical reactions. First, methods of electronic, vibrational, and rotational excitation for atoms and molecules will be discussed, preceded by methods of molecular dissociation.

Electronic excitation can occur in both atoms and molecules and requires the highest electron energies ($T_e > 10$ eV) compared to other excitation processes. As with all excitation processes, energy is transferred from the high energy electron to the low energy neutral, and this absorbed energy transitions the neutral species from the ground state to an excited state (Equation 3.16). Cross sections for electronic excitation are on the order of $\sigma \sim 10^{-17}$ cm² [37].



Vibrational excitation requires less electron energy to stimulate and is very important for plasma-chemistry processes in non-thermal discharges. The process of vibrational excitation is considered to be completed in two steps with the creation of an unstable, short-lifetime excited negative ion, as shown in Equation 3.17 [37]. This describes the transition of molecule AB from vibrational state v_1 to v_2 where v_i is the vibrational quantum number of the negative ion, and is considered a resonant process

due to the structure of cross-section dependence on electron energy.



Vibrational excitation is most effectively stimulated when $T_e \sim 1 - 3$ eV, which can result in reaction rate coefficients as high as 10^{-7} cm³/s [37]. In molecules like N₂, CO₂, and CO, much of the input energy can be transferred to vibrational excitation in non-thermal discharges because of this relation to electron energy. Similar to vibrational excitation, rotational excitation can also proceed resonantly via an intermediate ionized state, though the contribution of the multi-step event is much smaller than the low values of rotational energy quantum [37].

Besides excitation, molecular dissociation can also result from electron-neutral collisions. Electron impact dissociation can proceed in single or multi-step processes. Vibrational excitation leading to dissociation requires a non-direct step-by-step process in which molecules exchange vibrational energy until reaching the threshold for dissociation. However dissociation via electronic excitation is a direct process resulting from a single collision. Figure 3.2 shows the different intermediate transitions that can occur once a molecule is electronically excited to dissociation [37].

In excitation channel A, the molecule is excited to a repulsive state by an electron with energy greatly exceeding that required for dissociation. High energy neutral atoms are generated as a result. In channel B, the molecule is excited to an attractive state with energy exceeding the dissociation energy, though the resulting atoms are of lower energy. Similar to A, high energy atoms are the products of channel C where the molecule is excited to an attractive state that can lead to a transition to a low-energy repulsive state. As in channel C, channel D begins with an excitation to an attractive state which transfers to a high energy repulsive state leading to electronically excited products. Channel E requires the highest electron energies in which the molecule is

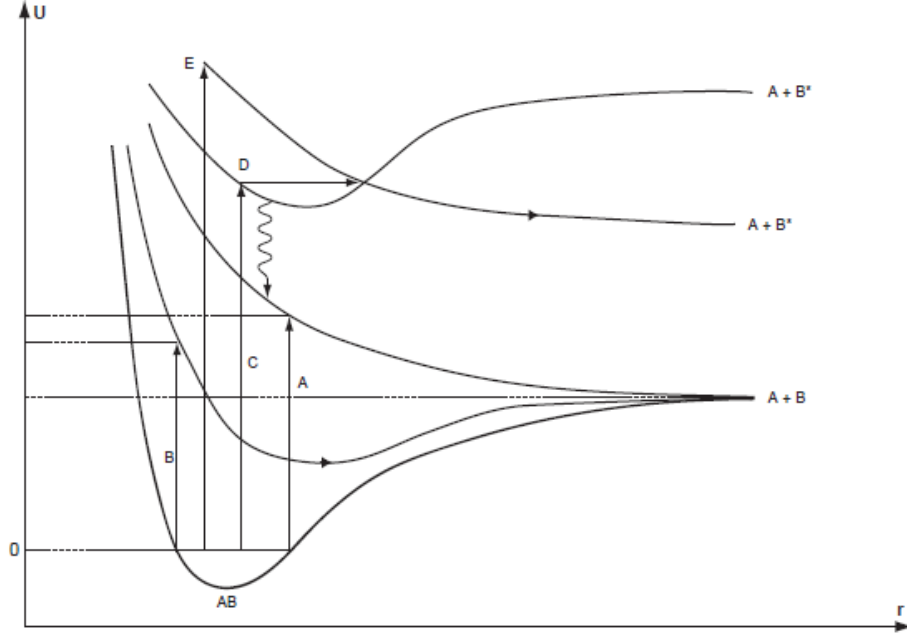


Figure 3.2: Electronic excitation methods of dissociation [37].

excited to repulsive state creating electronically excited atoms from dissociation [37].

3.1.3 Plasma Sources

It is now appropriate to explain the generation of plasma and electromagnetic wave propagation in different plasma sources, specifically RF and MW discharges which are relevant for this dissertation. Given that power is initially transferred to the electrons in a plasma, it is important to understand how charged particles interact with electromagnetic fields. According to the Lorentz force law, an electric charge q is accelerated by electric and magnetic fields \vec{E} and \vec{B} in the following way:

$$\vec{F} = m\vec{a} = m\frac{d\vec{v}}{dt} = q\left[\vec{E} + \vec{v} \times \vec{B}\right] \quad (3.18)$$

Thus in a simple DC discharge with a uniform electric field $\vec{E} = \vec{E}_0$ and no applied magnetic field, the acceleration a charged particle experiences is shown in Equation 3.19 [61]. If the particle is an electron, the particle will accelerate in the opposite

direction of \vec{E} .

$$\frac{d\vec{v}}{dt} = \frac{q}{m} \vec{E}_0 \quad (3.19)$$

Likewise, when charge q is in the presence of a uniform magnetic field $\vec{B} = B_z$ with $\vec{E} = 0$, the equations of motion become [61]:

$$m \frac{dv_x}{dt} = qv_y B_0 \quad (3.20a)$$

$$m \frac{dv_y}{dt} = -qv_x B_0 \quad (3.20b)$$

where the acceleration along z goes to zero when taking the cross product of two vectors in the same direction. After differentiating 3.20a and substituting 3.20b for v_y the equation becomes

$$\frac{d^2 v_x}{dt^2} = -w_c^2 v_x, \quad (3.21a)$$

$$w_c = \frac{qB_0}{m} \quad (3.21b)$$

From Equation 3.21b the cyclotron frequency, w_c , is defined [61]. Solutions to Equation 3.21a show that a charged particle will gyrate in a circular motion with frequency w_c along with direction z when a magnetic field B_z is applied. However when a combination of oscillatory electric and magnetic fields are applied to a charge as in the electromagnetic (EM) waves of RF and MW discharges, the motion becomes far more complicated.

Because of the force imparted on an electron by an electric field, all plasmas are subject to Ohmic heating, even if the electric field is small in the bulk plasma. Ohmic (Joule) heating refers to the process by which power is transferred to the plasma via electron-neutral collisions. As electrons are accelerated by the electric field and gain kinetic energy, some of that kinetic energy can be transmitted via inelastic collisional processes to neutral species. This results in the excitation or ionization of the particle. The power transfer to an electron in the presence of an electric field can be calculated

as follows [61]:

$$P = \vec{J} \cdot \vec{E} \quad (3.22)$$

where \vec{J} is the current density given by Ohm's law as:

$$\vec{J} = \sigma \vec{E}. \quad (3.23)$$

Here, σ is the DC electron conductivity found to be

$$\sigma = \frac{n_e e^2}{m \nu_{en}} \quad (3.24)$$

where n_e is the electron number density, m is the mass of an electron, and ν_{en} is the electron-neutral collision frequency. After substitution of (3.23) into (3.22), the final power transfer can be written as:

$$P = \sigma E^2 = \frac{n_e e^2 E^2}{m \nu_{en}}. \quad (3.25)$$

While Ohmic heating is the most common source of electron heating in a plasma, there are other heating mechanisms that are of importance depending on the discharge type. Low pressure RF capacitive and inductive discharges rely on stochastic heating, while wave-particle interactions play a role in helicon and MW sources. These mechanisms will be discussed in the following section along with properties of RF and MW sources.

3.1.3.1 Radio-frequency and Microwave Discharges

RF discharges can be operated from low pressure up to atmospheric pressure, though the low-pressure regime will be the focus of this section because of its relevance to the experimental work performed for this dissertation. Low pressure RF plasmas are characteristically non-thermal with $T_e \gg T_0$, due to a low electron-neutral collision

frequency and high rates of gas cooling by the walls. RF plasmas can also be operated in three different power coupling regimes denoted as capacitive, inductive, and helicon mode. The characteristics of each mode will be described below.

In a capacitively coupled plasma (CCP), an oscillating RF voltage is typically applied to electrodes located either within or outside the vacuum chamber. These two common configurations using parallel plates for the electrodes are shown in Figure 3.3. The CCP is particularly successful at stimulating high electric fields, facilitating plasma ignition [37].



Figure 3.3: Configurations for capacitive discharges: a) electrodes inside the plasma, and b) electrodes outside the plasma [37].

In this parallel plate configuration, an oscillating current flows between the plates forming a plasma in between, along with a corresponding voltage across the plates. A sheath of positive charges is formed along the surface of the electrode, where within the sheath $n_e \ll n_i$. This charge separation forms an internal potential, reflecting any electrons traveling towards the wall back into the plasma. Likewise, positive ions that enter the sheath are accelerated to the wall. The formation of the sheath and accompanying potential is shown in Figure 3.4.

The current flowing within the sheaths is due to the time-varying electric field, unlike in the bulk plasma where the current is due to the conduction of electrons. Thus the sheath boundary will actually oscillate with the applied current [61]. This sheath boundary oscillation is the source of an electron heating mechanism called the stochastic heating effect. As an incoming electron with mean free path greater

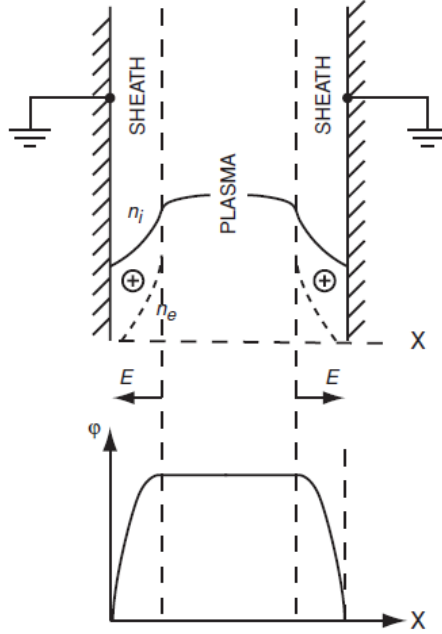


Figure 3.4: Formation of a sheath along electrodes in a CCP [37].

than the sheath size moves toward the sheath, that electron will gain kinetic energy if the sheath boundary is moving away from the electrode (essentially moving towards the electron). However if the sheath boundary is moving in the opposite direction towards the electrode, the electron will lose kinetic energy as it is reflected back into the plasma [37].

In contrast to a CCP, the inductively coupled plasma (ICP) stimulates an EM field through an inductive coil. Possible configurations of the inductive coil are shown in Figure 3.5. An ICP will particularly stimulate the magnetic field due to the oscillating current passing through the coil, creating a comparatively low electric field. Therefore, the ICP is usually generated at low pressure where values of reduced electric field, E/p (where p is pressure), are sufficient for breakdown. Under these conditions, ICP discharges can achieve high currents and high electron densities on the order of $10^{11} - 10^{12} \text{ cm}^{-3}$ [37]. All ICPs have a capacitive component, characterized by low plasma densities when the plasma is coupled to the low- and high-voltage ends of the cylindrical coil [61]. A jump in electron density can be observed when the discharge

changes to inductive mode, where plasma is driven by the induced electric field inside the coil.

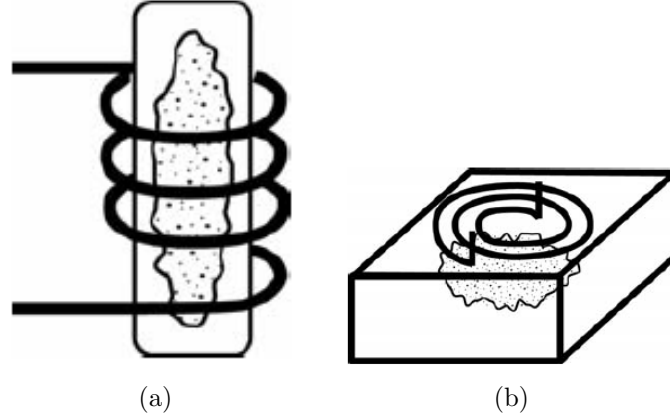


Figure 3.5: Possible configurations of ICP: a) the plasma is located inside the coil, and b) the plasma is located adjacent to the coil [37].

Unlike CCP discharges, RF power is coupled to the plasma through a dielectric window or wall; the plasma has no direct contact with the coils. However power can be transferred to electrons in a small layer near the plasma surface called the skin depth, δ , similar to the stochastic collisionless heating process mentioned for CCP discharges. In this process, electrons are accelerated and thermalized via interaction with the oscillating electric fields within the skin depth layer [61]. Here the interaction time of the electrons with δ is short compared to the RF frequency, and a stochastic collision frequency can be defined as [61]:

$$\nu_{stoc} = \frac{C_e \bar{v}_e}{4\delta_e} \quad (3.26)$$

where \bar{v}_e is the average electron velocity, δ_e is the anomalous skin depth, and C_e is a dimensionless constant of order unity if the relation $\bar{v}_e/2\delta_e \gg \omega, \nu_m$ holds true (ω is the RF frequency and ν_m is the electron-neutral momentum transfer frequency) [61].

Assuming that $\nu_{stoc} \gg \omega$, the anomalous skin depth is given by

$$\delta_e = \left(\frac{C_e c^2 \bar{v}_e}{2\omega \omega_{pe}^2} \right)^{1/3} \quad (3.27)$$

where c is the speed of light and ω_{pe} is the plasma frequency.

The helicon plasma is the third operating mode of RF discharges. This is a wave-heated plasma that is sustained by an EM wave and an external magnetic field. RF frequencies range from 1 - 50 MHz with magnetic fields on the order of a few hundred Gauss. Similar to the inductive coil configuration of an ICP, the helicon wave is excited by an RF antenna that typically surrounds a cylindrical dielectric plasma-containing vessel. Electromagnets surround the antenna and the plasma tube, forming a uniform DC magnetic field along the plasma column. These discharges are able to achieve high electron densities up to 10^{14} cm^{-3} [61]. The RF antenna excites the transverse mode structure, resulting in a superposition of low-frequency whistler waves propagating at a fixed angle to the external \vec{B} field. The antenna will couple to transverse electric or magnetic fields to excite a specific mode.

Energy transferred to electrons takes place via wave-particle interaction. In collisional damping, the helicon mode propagates along the plasma column and energy is transferred to the bulk electron population from Ohmic heating. However in collisionless Landau damping, the wave transfers energy to electrons that have velocities near the wave phase velocity $v_{ph} = \omega/k_z$, where k_z is the axial component of the wave vector [61]. Landau damping can result in a non-equilibrium electron population in which a portion of the electrons have energies much higher than the bulk electron temperature. Other mechanisms have been cited as possibly contributing to electron heating, such as electron trapping in large amplitude helicon waves or excitation of Trivelpiece-Gould modes. However, it is clear that Ohmic heating alone cannot account for the electron energies in low pressure helicon discharges.

Surface wave discharges excited by microwaves are another type of plasma that utilizes wave-particle interactions for energy transfer. Surface waves are defined as waves that only propagate near the surface of the plasma and can be launched in a range of frequencies, typically in the microwave regime from 1 - 10 GHz. When operating microwave plasmas, the EM waves will usually propagate through rectangular waveguides until striking the plasma. The wave propagation inside a waveguide can be described using Maxwell's equations assuming an EM field sinusoidal time dependence of $e^{-i\omega t}$:

$$\nabla \times \mathbf{E} = i\omega\mathbf{B} \quad (3.28a)$$

$$\nabla \times \mathbf{B} = -i\mu\epsilon\omega\mathbf{E} \quad (3.28b)$$

$$\nabla \cdot \mathbf{E} = 0 \quad (3.28c)$$

$$\nabla \cdot \mathbf{B} = 0 \quad (3.28d)$$

Three different types of wave propagation modes may be excited for microwave propagation. The transverse electromagnetic (TEM) waves have no electric or magnetic field in the direction of propagation. Thus in polar coordinate notation, $B_z = E_z = 0$. The transverse magnetic (TM) waves have an electric field but no magnetic field in the direction of propagation ($B_z = 0, E_z \neq 0$). The transverse electric (TE) waves are the opposite of TM, with a magnetic field but no electric field in the direction of propagation ($B_z \neq 0, E_z = 0$). The transverse electric and magnetic fields derived from (3.28) for the TM and TE waves, respectively, are given below [50]:

$$\mathbf{E}_t = \pm \frac{ik}{\gamma^2} \nabla_t \psi \quad (3.29a)$$

$$\mathbf{B}_t = \pm \frac{ik}{\gamma^2} \nabla_t \psi \quad (3.29b)$$

where the scalar function ψ satisfies the wave equation as

$$(\nabla_t^2 + \gamma) \psi = 0 \quad (3.30)$$

and γ , the propagation constant, is defined as

$$\gamma^2 = \mu\epsilon\omega^2 - k^2. \quad (3.31)$$

Here k is the wave number. For a given ω , k is determined for each solution, α , of the eigenvalue equations (3.29) [50].

$$k_\alpha^2 = \mu\epsilon\omega^2 - \gamma_\alpha^2 \quad (3.32)$$

A cutoff frequency can be defined by setting $k_\alpha = 0$ in (3.32):

$$\omega_\alpha = \frac{\gamma_\alpha}{\sqrt{\mu\epsilon}} \quad (3.33)$$

and k can be written as:

$$k_\alpha = \sqrt{\mu\epsilon} \sqrt{\omega^2 - \omega_\alpha^2}. \quad (3.34)$$

An examination of (3.34) will determine if the wave will propagate in a given waveguide or not. For wave frequencies greater than the cutoff frequency ($\omega > \omega_\alpha$), k_α is real and can propagate through the waveguide. For $\omega < \omega_\alpha$, k_α is imaginary and thus the wave will decay exponentially in an evanescent field [50].

When an azimuthally symmetric ($m = 0$) surface wave is launched along the plasma column, a TM wave results with electric and magnetic field components E_z, E_r, H_ϕ [10,65,67]. Figure 3.6 shows the radial and axial components of the electric field for the $m = 0$ wave. The electric field has a maximum at the plasma dielectric interface, and thus the wave is evanescent (exponentially decaying) in both directions

away from the wall. The axial component of the electric field dominates over the radial component once the wave penetrates the plasma region. The $m = 1$ mode can also be launched to sustain the plasma, provided that the product of the wave frequency, f and the tube radius, a exceed a critical value: $fa > 2$ GHz-cm [65]. Below this value, only the $m = 0$ mode will propagate.

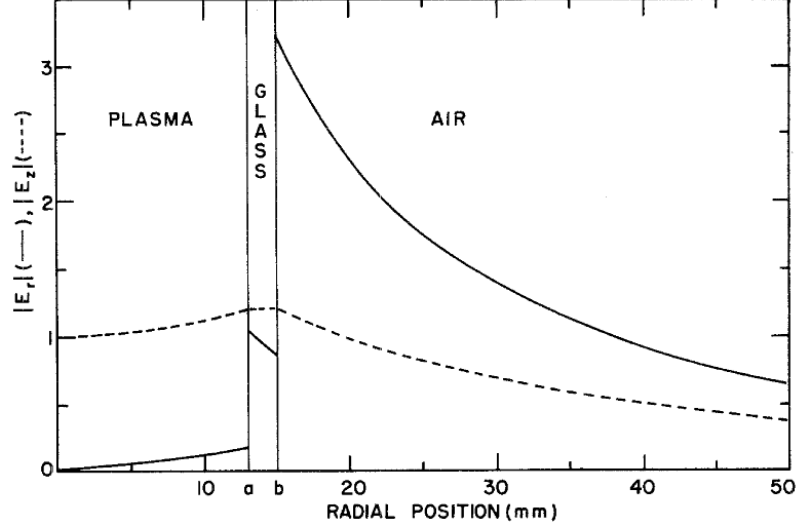


Figure 3.6: Electric field intensity of the $m = 0$ surface wave as a function of radial position. $|E_z|$ and $|E_r|$ are the axial and radial components, respectively, for a wave propagating along a cylindrical plasma column [10].

In surface wave discharges, a surface wave launcher creates an electromagnetic wave that travels along the interface of the plasma column and the enclosing dielectric barrier, delivering energy to the plasma zone from the power flux carried by the wave. In principle, the plasma column length has no limitation, but in practice the power handling capability of the waveguides or wave launcher will impose such limits. This feature contrasts many traditional microwave frequency discharges which are limited in plasma volume. To initially break down gas at atmospheric pressure using this surface-wave launcher, either the electric field created by the launcher must be large enough to cause spontaneous breakdown or an external ignition source must be used, such as a Tesla coil. Once the electron density, n_e , becomes greater than the critical value, n_{crit} , a surface wave is excited and propagates along the plasma column until

it is reflected back when $n_e \approx n_{crit}$. Equation 3.35 gives the definition of the critical density where ϵ_0 is the permittivity of free space, m is the electron mass, ω^2 is the microwave frequency, and κ_d is the dielectric constant [61].

$$n_{crit} = \frac{\epsilon_0 m \omega^2}{e^2} (1 + \kappa_d) \quad (3.35)$$

This critical value is the electron density corresponding to surface-wave resonance and represents the axial point at which the plasma column ends. Therefore, the plasma column length, and essentially the axial electron density, is actually determined by the total power input delivered to the launcher, rather than by the characteristics of the launcher itself. A plot demonstrating this linear relationship between the plasma column length and input power is shown in Figure 3.7. The power balance relation for surface wave discharges shown in Equation 3.36 displays the dependence of electron density on input power, where $\alpha(\bar{n})$ is the wave attenuation coefficient, \bar{n} is the cross sectional average electron density, $P(z)$ is the axial power flux, a is the discharge tube radius, and θ is the power lost per electron [67].

$$2\alpha(\bar{n})P(z) = \pi a^2 \bar{n} \theta \quad (3.36)$$

3.2 Plasma Processes for CO₂ Dissociation

In the following section, mechanisms for CO₂ conversion in a plasma system will be discussed. The processes for dissociation via vibrational and electronic excitation will be illustrated followed by the effectiveness of dissociation in thermal and non-thermal discharges.

In any system, the dissociation of CO₂ is an endothermic process that starts with

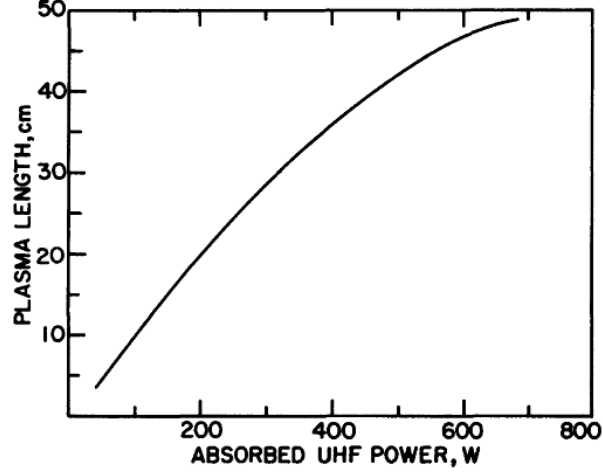
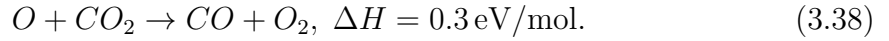


Figure 3.7: Relationship between plasma column length and input power. Plasma produced in Ar at atmospheric pressure [67].

and is limited by the following reaction:



From here the oxygen atom is free to interact with other CO_2 molecules to form molecular oxygen via:



This results in the equation for total CO_2 decomposition as:



The energy efficiency of the plasma process for CO_2 dissociation can be written as

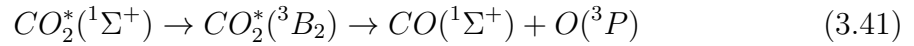
$$\eta = \frac{\Delta H}{E_{CO}}, \quad (3.40)$$

where $\Delta H = 2.9 \text{ eV/mol}$ is the enthalpy of dissociation for CO_2 and E_{CO} is the actual

energy cost for one CO molecule produced in the plasma [37].

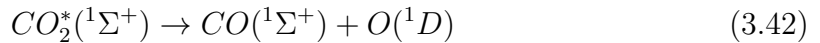
3.2.1 Vibrational Excitation

Plasma assisted dissociation of molecules occurs through electron impact by vibrational and electronic excitation. Vibrational excitation is the most effective means for CO₂ dissociation because the process requires the least amount of energy. Plasma electrons excite low vibrational levels of the ground electronic state CO₂(¹Σ⁺), and these low-energy excited species participate in vibrational-vibrational (VV) energy exchange to create highly excited species with enough energy for dissociation to occur. The non-adiabatic dissociation of vibrationally excited CO₂ resulting from the transition ¹Σ⁺ → ³B₂ from the ground electronic state to a low valence excited state requires only 5.5 eV/mol, which is the exact energy of the OC=O bond. This is a non-direct multi-step process that takes place through VV quantum exchange, as shown in Equation 3.41 [37].



From here, the electronically ground state oxygen atom that is created can participate in a secondary reaction with another vibrationally excited CO₂ molecule to create another CO molecule, as described in Equation 3.38.

Figure 3.8 shows the dissociation process based on the excitation of the different low electronic terms of CO₂. If instead the one-step adiabatic dissociation channel of a vibrationally excited CO₂ molecule is used, over 7 eV is consumed in the process (3.42) [37]. In the interest of energy efficiency, the non-adiabatic process is clearly preferred.



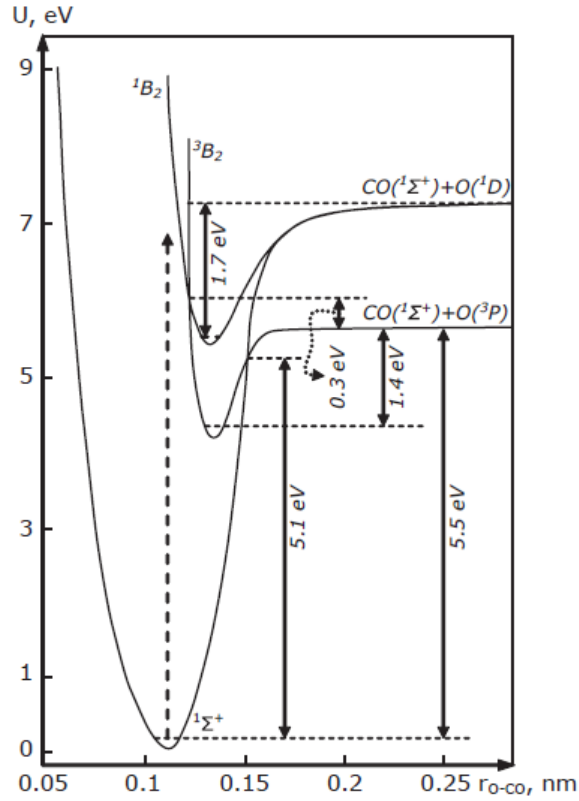
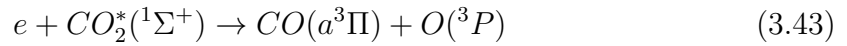


Figure 3.8: Energy level diagram of CO₂ [37].

3.2.2 Electronic Excitation

Dissociation by electronic excitation is a one-step process that results in the creation of an electronically excited CO molecule(3.43).



This dissociation mechanism is typically dominant in low - pressure discharges with high values of reduced electric field where vibrational excitation is suppressed. Energy efficiency is limited in plasmas with dissociation via electronic excitation because electron energy must exceed 14 eV/mol for dissociation to occur, which is significantly higher than the OC=O bond energy [37]. Also, the high electron energies required give rise to the excitation of various other states that do not efficiently contribute to dissociation, resulting in low energy efficiency. The maximum energy efficiency achieved

using the electronic excitation mechanism is only about 25% in an experimental non-thermal electric discharge due to the high CO cost of 11.5 eV/mol. Figure 3.9 shows various simulated theoretical results including some experimental results for energy efficiency of CO₂ dissociation stimulated by electronic excitation. Curves 1 and 2 represent the inclusion of singlet and triplet states, while curve 3 is of total energy efficiency with the dots showing experimental results.

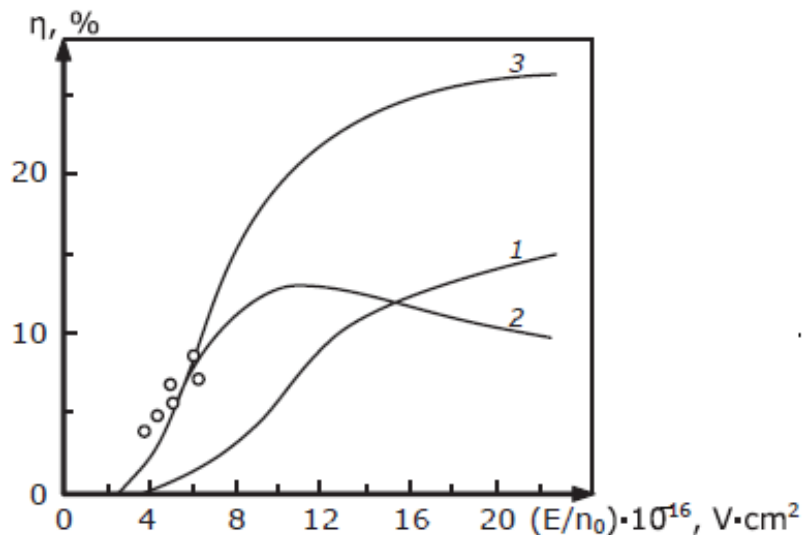


Figure 3.9: Electronic excitation energy efficiency [37].

3.2.3 Thermal Discharges

In thermal discharges, dissociation is achieved by a shift in thermodynamic equilibrium in the direction of CO formation. The thermal plasma simply provides the high temperatures needed for the shift to occur. Figure 3.10 shows simulated results of CO₂ dissociation as a function of gas temperature at a pressure of about 120 torr (0.16 atm). For significant conversion of CO₂ to CO, the gas temperature must reach at least 3000 K. These high temperature requirements actually limit the efficiency of the process. The products must be quickly quenched (at a rate on the order of 10⁷ K/s and greater) to prevent the recombination of CO and O to produce CO₂, which can be otherwise prevalent under those temperature conditions. Also, thermal

discharges distribute energy over all degrees of freedom, instead of selectively exciting the vibrational modes of CO_2 , essentially limiting energy efficiency to a maximum of 43% [37].

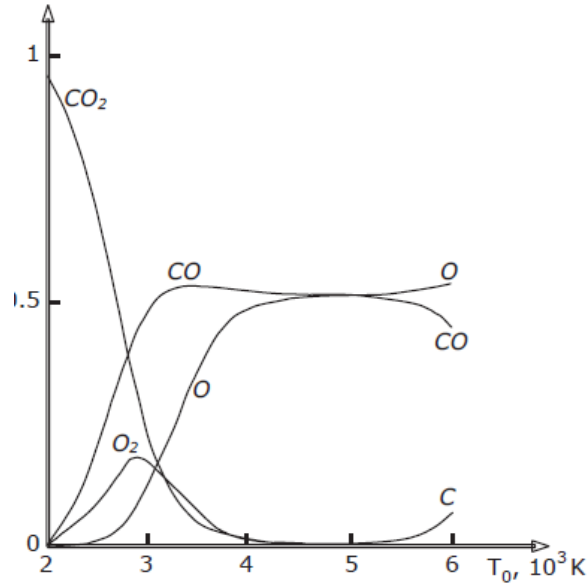


Figure 3.10: Equilibrium molar fraction products of CO_2 dissociation in thermal discharge [37].

3.2.4 Non-thermal Discharges

Non-thermal plasmas have the unique ability to activate the vibrational excitation of CO_2 molecules because of the characteristic low electron temperature in the range of $T_e = 1\text{-}2$ eV. At this electron energy, no less than 95% of all the discharge energy is transferred from electrons to CO_2 vibrational excitation based on the reaction rate coefficients for this process. The rate coefficient for vibrational excitation of the first vibrational state reaches a maximum value of $k_e \approx 1 \times 10^{-8}$ cm^3/s when $T_e \approx 1$ eV, while the vibrational energy losses from vibrational-translational (VT) relaxation are relatively slow, $k_{V-T} \approx 10^{-10}$ cm^3/s . This allows for the creation of a high population of vibrationally excited molecules, which leads to effective CO_2 dissociation. Figure 3.11 shows the rate coefficients for the main electron impact

excitation processes. Vibrational excitation shown in the solid line is the dominant process for low electron temperatures since the rate coefficient is the highest. Electronic excitation shown in the dotted line takes over around 7 eV and becomes the dominant process for electron impact excitation.

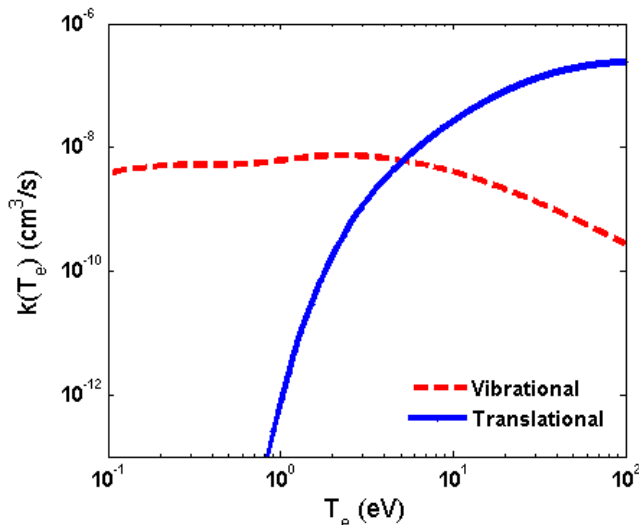


Figure 3.11: CO₂ electron impact rate coefficients. The first vibrational level and second electronic excitation level are shown as they are most dominant modes in this range of T_e .

In order to stimulate effective CO₂ dissociation through vibrational excitation, the population of vibrationally excited molecules must be maintained. This requires that the vibrational temperature, T_v , exceed the gas temperature, T_0 , resulting in a degree of thermal non-equilibrium between T_v and T_0 . The CO₂ molecules are linear in the form O=C=O and have three normal vibrational modes shown in Figure 3.12: asymmetric stretch mode, symmetric bending mode, and symmetric stretch mode. These vibrational modes only occur at the natural resonant frequency of the CO₂ molecule and have discrete energy levels.

Specifically, the asymmetric stretch mode of CO₂ is of concern because it is predominantly excited by electrons with $T_e = 1-3$ eV and the (VT) relaxation rate is slower for this mode than the symmetric vibrational modes. Also, the VV energy

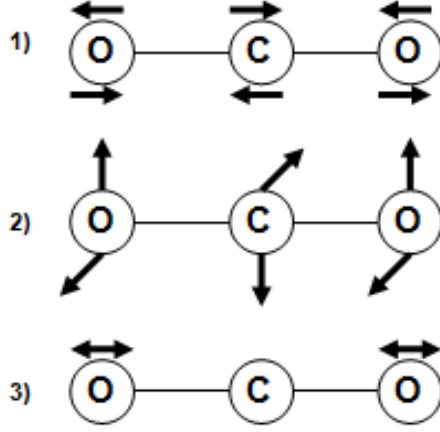


Figure 3.12: Vibrational modes of CO₂: 1) asymmetric stretch, 2) symmetric bending, 3) symmetric stretch [37].

exchange process is much faster for the asymmetric mode, which can intensify the population of highly excited species. Therefore, effective dissociation requires $T_{va} \geq T_{vs} > T_0$, where T_{va} is the asymmetric vibrational temperature and T_{vs} is the symmetric vibrational temperature.

This thermal non-equilibrium between T_v and T_0 increases as the plasma ionization degree increases, resulting in high energy efficiencies achieved in plasmas with high ionization degrees. The low gas temperatures characteristic of non-thermal discharges enable the existence of thermal non-equilibrium, and also protect against reverse reactions of the discharge products, CO and O. There is a critical vibrational temperature, T_v^{min} , above which most of the vibrational energy contributes to CO₂ dissociation. Below this value, vibrational energy is lost to VT relaxation. Typical values of T_v^{min} are around 1000 K. This leads to a restriction on the ionization degree which must also exceed a critical value for effective CO₂ dissociation to occur, as displayed in Equation 3.44:

$$\left(\frac{n_e}{n_0}\right)_{crit} = \frac{k_{VT}^s \cdot \epsilon_V(T_v^{min})}{k_{eV} \cdot \hbar\omega_a} \quad (3.44)$$

where k_{VT}^s is the VT relaxation rate coefficient for low vibrational levels, ϵ_V is the vibrational energy, k_{eV} is the rate coefficient for CO₂ electron impact vibrational

excitation, and ω_a is the frequency of the asymmetric vibrational mode. This threshold value is usually about $n_e/n_0 \geq 3 \times 10^{-7}$. In summary, a plasma source that is able to maintain vibrational-translational non-equilibrium has the potential to obtain energy efficiencies as high as 80-90% [37].

3.3 Plasma/Catalyst Systems

The following section will describe the use of catalyst material combined with plasma to enhance plasma-chemical reactions. First an introduction to catalysis will be given, citing the function of a catalyst in chemical reactions. Then a description of various plasma/catalyst systems will be given and their uses for general waste gas treatment. Finally, the specific uses of plasma/catalyst systems for CO₂ dissociation will be discussed.

3.3.1 Overview of Catalysis

Catalysts are substances that speed up reaction rates and improve chemical selectivity, allowing chemical processes to take place at temperature and pressure conditions under which they would otherwise not be able to proceed. Heterogeneous catalysis, the type that is of importance for this work, is a process by which the catalyst is instantaneously changed when reactants and products adsorb on the surface of the catalyst [85]. First the reactants adsorb on the surface, becoming activated by interaction with the catalyst, which causes a rapid and selective transformation of the reactants into adsorbed products. Then the products desorb from the surface, leaving the catalyst in its original state until the process begins again [85]. The selectivity, which is the ratio of rates for competing reactions, may also be manipulated via catalyst by preferentially increasing the rate of the rate-determining step of a desired stoichiometric reaction. Thus, catalysts can help achieve a specific outcome of products.

A catalyst is able to increase the reaction rate of a process by lowering the activation

energy, or energy barrier, of the reaction. This is accomplished by providing a surface on which adsorption and dissociation can occur and that can more easily transform reactants into products. Figure 3.13 shows how the activation energy, E_{act} , can be affected by the presence of catalyst material, leading to, in this case, an exothermic reaction given by a negative ΔH .

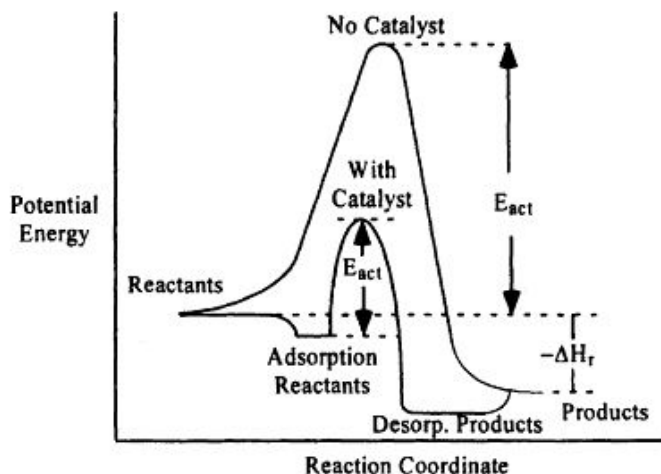


Figure 3.13: Catalytic effects on activation energy [85].

The reaction rate is a function of temperature and concentration, which can be illustrated by Equation 3.45 [85]. Here $k(T)$ is the rate constant defined by Arrhenius law with A as the pre-exponential factor, T as temperature, and R as the ideal gas law constant. In collision theory of catalyst reactions, A is proportional to the number of catalytic sites. The quantity $e^{(-E_{act}/RT)}$ is the probability of collisions that result in a reaction. C_i is given as the concentration of reactants and possibly products, which is taken in a product summation raised to empirically derived exponential factors α_i [85]. Thus, a catalyst can increase the reaction rate in two ways: by increasing the number of reaction sites (given by A), or by decreasing E_{act} (which results in an increase in the number of collisions that result in reactions).

$$r = k(T)f(C_i) = Ae^{(-E_{act}/RT)} \times \prod_i (C_i)^{\alpha_i} \quad (3.45)$$

One of the main mechanisms for increasing the number of available catalytic sites is to add a support surface for the catalyst species. The goal is to maximize the catalyst surface area, which can be done by using high-surface-area porous oxide materials as carriers, such as TiO_2 , Al_2O_3 , and SiO_2 . These porous surfaces provide an ideal medium for preparing well-dispersed, tiny and discrete crystallite catalyst particles. The high catalyst surface area is also maintained on a support by preventing migration at high temperatures [85].

There are two kinds of adsorption that can occur on a catalytic site: physisorption and chemisorption. Adsorption occurs when a chemical bond is formed between the adsorbing species and the adsorbing surface. This bond is favored when the adsorbent surface atoms have a propensity to decrease their surface energy. Physisorption is relatively weak, relying on attractive Van der Waals forces between adsorbate and adsorbent. This occurs as the condensation of gas molecules on a surface at low temperatures, with a typical Van der Waals layer separating the two species. In contrast, chemisorption occurs at high temperatures on the order of 1000 K and the adsorbate and adsorbent actually form chemical bonds at the surface. An illustration of both adsorption processes is shown in Figure 3.14. Chemisorption is the process of concern for this dissertation, as the reactions are at high temperatures and dissociation of reactive molecules can proceed when the energy gained from surface bonding exceeds the binding energy [85].

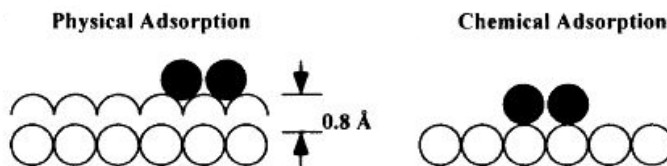


Figure 3.14: Illustration of surface adsorption [85].

Heterogeneous catalyst materials are composed of three main components: the active phase, a promoter, and a carrier or support. The active phases are usually

transition metals and/or their oxides and sulfides, which are dispersed in the form of microcrystallites of diameter 1-50 nm on to the porous support structure. Transition metals are used because of their multiplicity of low energy surface electronic states which can easily transfer electrons [85]. Some examples of active phase catalysts are Pt, Pd, Rh, Ni, Co, and Ru. The promoter is used to increase activity and stability. Specifically, textural promoters are used to help prepare and maintain a well-dispersed active phase. These can simultaneously be used as a support, and are of the form of inert high surface area oxides. Chemical promoters are added to the catalyst material to enhance activity or selectivity of the active phase [85]. These promoters usually consist of alkali and alkaline earth metals or metal oxides. Carriers, as previously noted, are used to evenly disperse and stabilize the active phase, and consist of high-surface-area metal oxides and carbons [85].

3.3.2 Types of Plasma/Catalyst Systems

When catalysts are combined with plasmas, they are usually incorporated into a non-thermal plasma (NTP) in one of two ways: with the catalyst placed inside the discharge zone (in-plasma catalysis (IPC)) or after the discharge zone (post-plasma catalysis (PPC)). Some studies have shown that the catalyst can be more effective at increasing gas conversion efficiencies when placed inside the discharge [12, 13]. These two configurations are illustrated in Figure 3.15. In either case, the plasma can be used to supply energy for catalyst activation and it can also provide the reactive gas species needed for reactions on the catalyst surface. For IPC systems, the catalyst is in contact with the discharge and, therefore, is also in contact with the short-lived excited species, radicals, photons, and electrons. In the PPC system, the catalyst is only exposed to the long-lived species that exit the discharge [109]. The catalyst material is typically introduced in the form of pellets, honeycomb monoliths, foam, or coating of the electrodes or reactor walls [13].

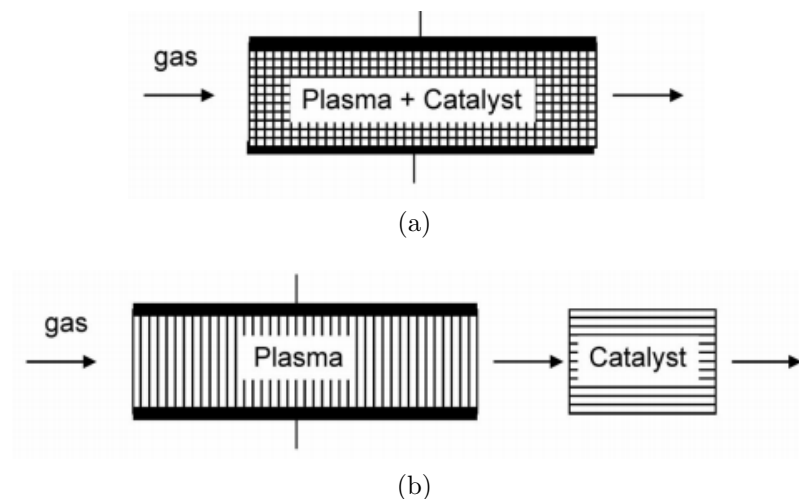


Figure 3.15: Plasma/catalyst configurations: a) catalyst placed inside the plasma, and b) catalyst placed post-plasma [109].

Given the direct interaction of IPC systems with the plasma, the discharge may affect catalyst performance and the catalyst may affect discharge performance. First the influence of the plasma discharge on catalysis will be addressed. As already mentioned previously, the plasma will provide a gas stream enriched with radicals and excited species which can accelerate thermal catalysis of the reactants and thus increase the energy efficiency of the process [13]. The plasma-treated catalyst may also result in reduced metal particle size and higher metal dispersion, both leading to higher catalyst reactivity and longer durability [13]. The catalyst can affect the plasma in several ways, as well. When catalyst material is placed inside the discharge in the form of a packed-bed reactor where there are numerous contact points between pellets and pellets/electrodes, the electric field can become enhanced depending on the dielectric constant of the pellet material. An enhanced electric field can lead to higher ionization and dissociation events, resulting in increased energy efficiency. Also, if the catalyst is able to adsorb the gaseous pollutants to be treated, this adsorption can increase the retention time of the pollutants in the discharge. This increased reaction time can lead to higher energy efficiency and possibly to improved selectivity. For PPC systems, the performance enhancements are much simpler. The main role

of the plasma is to change the gas composition before it reaches the catalyst, either providing chemically active species or pre-converting pollutants to more easily treated substances. [13].

Combined plasma/catalyst reactors have been established for various waste gas treatment systems such as NO_x removal, abatement of perfluorocarbons (PFCs), hydrocarbon reformation of methane, and removal of volatile organic compounds (VOCs). Typical catalysts used in these experiments are zeolites and metal oxides such as Al_2O_3 , TiO_2 , CuO , MgO , and ZnO [11, 18, 93]. Dielectric barrier discharges (DBDs) have frequently been studied for experimental plasma/catalyst systems where the catalyst can be packed into a cylindrical discharge tube or coated on one or both of the DBD electrodes. One study of NO_x removal in a DBD showed that the presence of a catalyst increased conversion efficiency to 65%, compared to just 24% when only the plasma was used [18]. Corona discharges are also commonly used for pollution abatement. In a study done for toluene degradation using a positive corona, 15 g of TiO_2 catalyst material were added to the discharge, resulting in an increased toluene removal rate from 27% to 82% [18].

There is a variety of experimental results similar to the examples given above showing the positive effects plasma/catalyst systems can have on gaseous pollution abatement. Though limited, there are also specific studies for plasma CO_2 dissociation combined with catalysis. One study has reported the effects of adding of porous $\gamma\text{-Al}_2\text{O}_3$ packed into a pulsed corona discharge [108]. With the plasma reactor alone, CO_2 conversion was only 3%. With the addition of the catalyst, the CO_2 conversion increased to 16% under the same operating conditions. A plot of these results is shown in Figure 3.16. This clearly demonstrates the capability of a catalyst to influence the conversion degree of CO_2 to CO in plasma systems. With the optimization of the plasma source and the correct catalyst, high energy efficiency could be achieved with a high conversion degree.

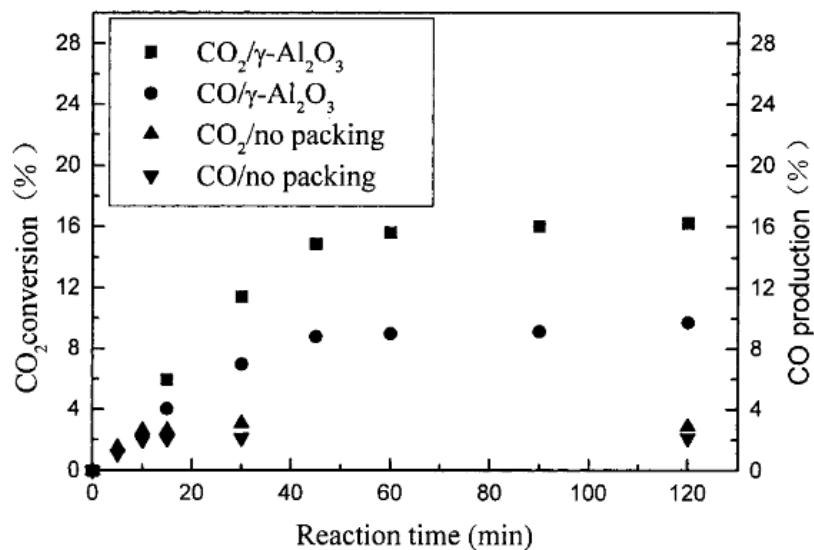


Figure 3.16: CO₂ conversion in an alumina-packed corona discharge [108].

3.4 Conclusions

This chapter has outlined the various complex behaviors describing plasma phenomena. There are several collisional processes that affect the energy exchange of charged and neutral species from ionization and excitation reaction mechanisms. For molecular dissociation of CO₂, vibrational excitation leads to the most efficient process. Thus, a NTP discharge capable of effectively stimulating the vibrational modes is an ideal candidate to study for CO₂ conversion. While there are many types of NTP discharges to choose from, RF and MW discharges have displayed some of the desired characteristics of high electron number density and thermal non-equilibrium between the electron temperature and the heavy particle gas temperature. The addition of catalyst material may prove to increase conversion rate without changing the energy input into the system, leading to a more energy efficient reaction than with the plasma alone.

CHAPTER IV

Preliminary Investigation in a Helicon Source

In Chapter III the physical processes in plasmas were discussed along with the characteristics of RF and MW discharges. Vibrational excitation was cited as the most effective means of CO₂ dissociation and the required plasma properties to achieve this were defined. In the following chapter, a preliminary experimental investigation of CO₂ dissociation in a RF plasma is discussed. First, a hypothesis will be given in Section 4.1 explaining the benefits of a RF plasma for CO₂ dissociation. Then the experimental setup and diagnostic tools will be described in Section 4.2. Section 4.3 gives the experimental results while Section 4.4 considers the basic energy efficiency requirements for such a plasma system to be viable for carbon emissions mitigation. Lastly, Section 4.5 provides some conclusions.

4.1 Hypothesis

4.1.1 Benefits of Helicon Source

The RF plasma used in this experiment is a low-pressure helicon discharge. As described in section 3.2, one of the essential requirements for stimulating vibrational excitation of CO₂ is creating thermal non-equilibrium between the electron temperature and the neutral gas temperature. Low-pressure RF plasmas are known for their non-thermal characteristics and have the ability to operate in three different modes,

capacitive, inductive, and helicon, offering a level of versatility unachievable in other systems. Another important factor for efficient CO₂ dissociation is ensuring a high ionization degree, $n_e/n_0 > 10^{-6}$. RF plasmas can achieve high ionization degrees, particularly when operating in inductive or helicon modes.

Specifically a RF helicon plasma was chosen for this work based on its ability to attain high electron densities on the order of 10^{14} cm⁻³ when operating at low pressure around 1 mtorr with 1 kW of RF power. Electron-neutral collisions are a primary mechanism for exciting vibrational modes of CO₂, thus the higher the electron density the more likely a collisional excitation process will occur. Helicon discharges also have the benefit of being electrodeless. When working with carbon containing compounds like CO₂ there is always a possibility of carbon deposition in the system. Plasma in contact with electrodes can result in carbon coating of the electrodes, degrading performance. Lastly, helicons are very efficient at generating high density plasmas, which can help improve overall CO₂ dissociation energy efficiency.

Given the helicon properties outlined above, it is expected that CO₂ will successfully dissociate into CO and O₂. A high conversion rate will most likely result from the expected high electron densities. The energy efficiency has the potential to be high if operated in helicon mode, provided that the plasma maintains a vibrationally excited population.

4.2 Research Design

4.2.1 Experimental Setup

Experiments were performed in the Cathode Test Facility (CTF) at the Plasmadynamics and Electric Propulsion Laboratory (PEPL) located at the University of Michigan. CTF consists of a cylindrical vacuum chamber measuring 0.61 m in diameter and 2.44 m in length used in conjunction with an Edwards XDS 35i dry

pump for chamber evacuation, reaching a base pressure of less than 3 mtorr. The RF plasma source is mounted on the side of the chamber on a port measuring 15 cm in diameter. Gas is injected into the chamber via a 15-cm-diameter by 50-cm-long quartz tube vacuum sealed to the side of the chamber by a rubber O-ring.

The helicon plasma source consists of a 13.56-MHz, 1-kW RF power supply connected to a double helix antenna via a pi-style matching network. The matching network reduces the reflected power to about 1% or less during operation. The antenna is wrapped around the quartz gas injection tube and is surrounded by three EM coils that provide an external peak magnetic field of 415 G along the centerline [71]. The electromagnetic coils are powered by a Lambda DC power supply capable of outputting a maximum current of 60 A. While electron density and electron temperature measurements were not taken during these tests, previous experiments performed in CTF under similar operating conditions near 300 mtorr have found that the electron density is about $10^9 - 10^{11} \text{ cm}^{-3}$ and electron temperature is typically in the range of 2-4 eV [70]. An illustration of the experimental setup is shown in Figure 4.1.

4.2.2 Diagnostics

A Stanford Research Systems RGA100 residual gas analyzer (RGA) is used in all experiments to identify the species present in the system. The maximum allowable operating pressure of the RGA is 10^{-4} torr, which is much lower than the plasma discharge operating regime of 50-300 mtorr. To accommodate the pressure requirements of the RGA, a differentially pumped subchamber is attached to the top of CTF in which the RGA is housed, reaching a base pressure of 10^{-9} torr. A variable leak valve is used to isolate the subchamber from the main plasma facility, while the subchamber is evacuated by a Varian V70LP turbomolecular pump backed by an Edwards E2M30 mechanical pump. A diagram of the RGA subchamber and its attachment to the

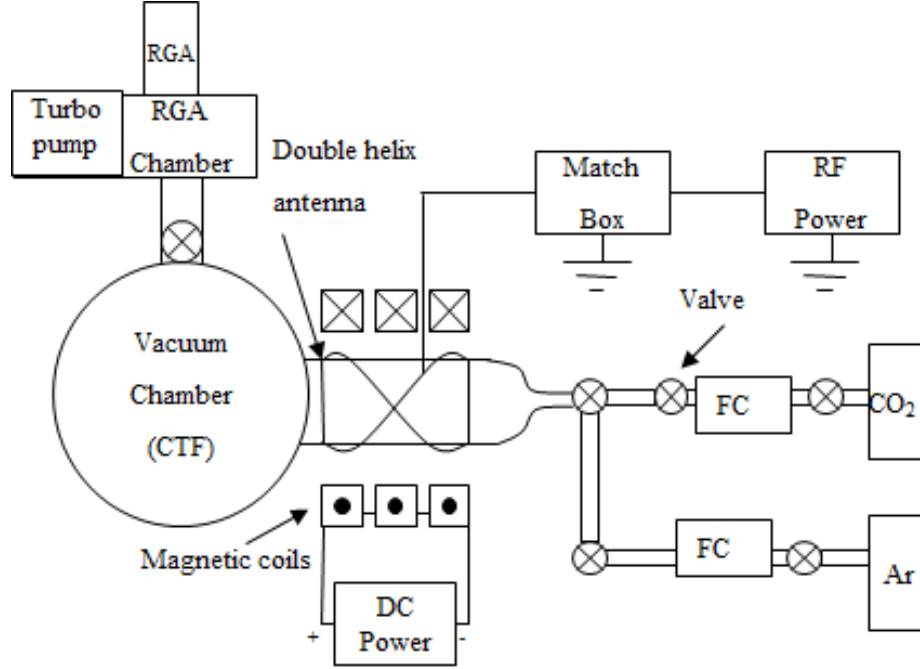


Figure 4.1: Experimental setup of helicon system.

main vacuum chamber is given in Figure 4.2.

In order to extract quantitative information from RGA spectra, a calibration must be performed for each gas species to be identified in the plasma. The RGA was calibrated using the method described by [71], in which a known fixed amount of argon flows into the plasma chamber with a varying amount of the target gas species (e.g. CO) to be identified. A calibration factor can be determined from the ratio of the measured partial pressures of Ar and the target gas, correlated with the known flow rates of each gas. Once the calibration factor is found, a flow rate of the species created in the plasma discharge can be calculated from Equation 4.1.

$$\dot{m}_i = \frac{\dot{m}_{Ar}}{CF} \frac{P_i}{P_{Ar}} \quad (4.1)$$

In Equation 4.1, \dot{m}_i is the plasma produced flow rate of the species in question, \dot{m}_{Ar} is the constant flow rate of Ar, CF is the calibration factor, P_i is the partial pressure of the target species in question, while P_{Ar} is the partial pressure of Ar. The ratio

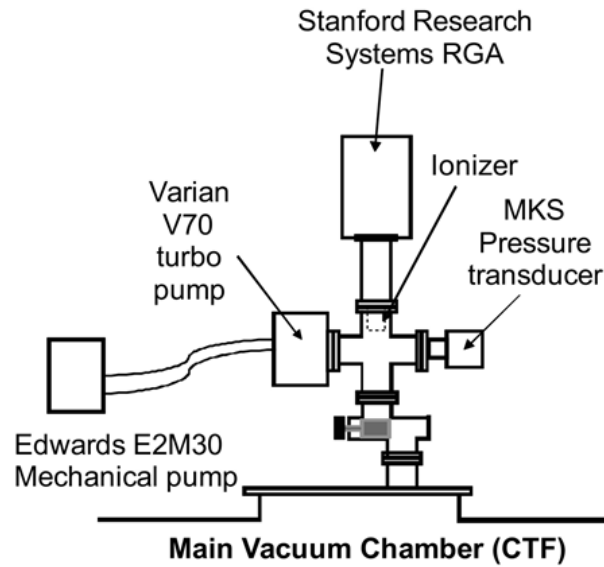


Figure 4.2: Diagram of RGA chamber [70].

of partial pressures can be plotted vs. the ratio of flow rates for CO_2 , CO , and O_2 and a linear relationship should be found. The slope of the line represents CF, as demonstrated in Figure 4.3a. A sample spectrum of the raw data taken by the RGA is shown in Figure 4.3b to demonstrate that CO_2 , CO , and O_2 are the main species present in the discharge.

For all RGA data presented here, results shown are the mean values of a sample of measurements. Error bars represent one standard deviation among the spread in the measurement sample. The sample size for the calibration data is three sets with three spectra for each data point. The sample size for the CO_2 plasma species measurements is two sets of data with three spectra for each data point.

4.3 Results

To determine the optimal operating conditions for CO_2 dissociation in the RF discharge, three parameters were varied: flow rate of CO_2 , RF power, and magnetic field strength. All results are presented for the combined CO_2/Ar plasma in which the

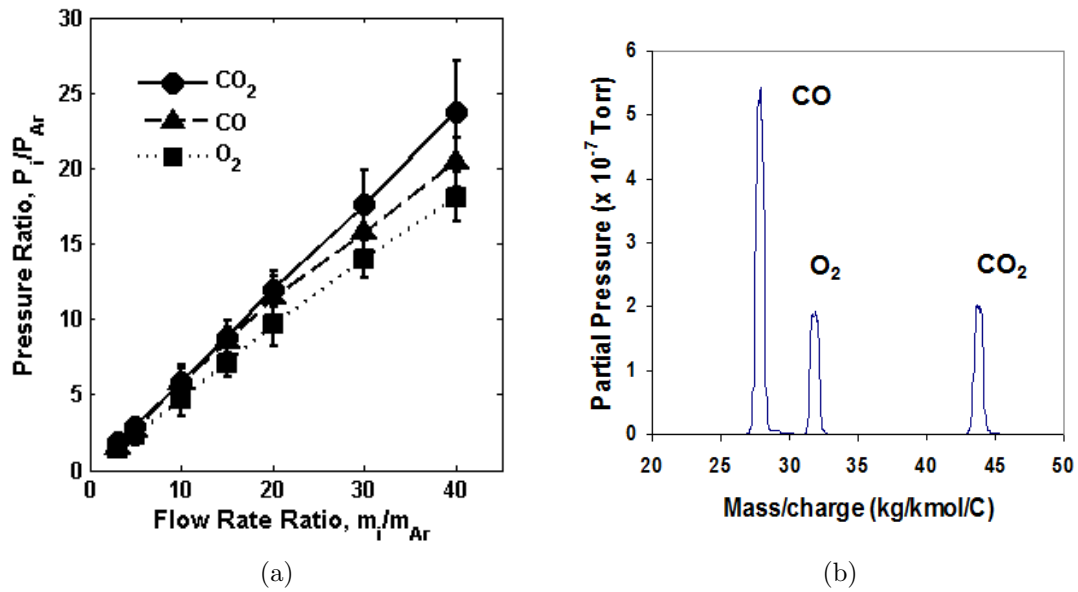


Figure 4.3: RGA data collection: a) calibration factor curve, b) sample RGA spectrum demonstrating CO_2 , CO , and O_2 as the main products.

flow rate of Ar remained constant at 10 standard cubic centimeter per minute (sccm) while the flow rate of CO_2 varied from 15 sccm up to 100 sccm. The flow rate of CO_2 was confined to 100 sccm to maintain a stable discharge. As the total flow rate increased, the pressure also increased inside the chamber and the discharge could not be sustained at powers under 700 W with CO_2 as the dominant input gas species. The total flow rate range corresponds to an operating pressure range of 80 to 280 mtorr in CTF.

For this set of experiments we were concerned with characterizing the efficiency of CO_2 dissociation with CO_2 as the majority gas in the system. The addition of Ar was solely used as a calibration gas and thus the flow rate of Ar remained constant throughout all tests. By increasing the ratio of Ar/ CO_2 , it is possible that more RF power would go into ionizing Ar, which is undesirable since we prefer all power to go into CO_2 dissociation to achieve high energy efficiency. RF power was manually set to 0, 250, 500, 750, and 1000 W in random order, and the applied DC current for the magnetic coils was set to 0, 30, and 60 A for each flow rate. The resulting maximum

axial magnetic fields at these currents are 0, 207, 415 G.

The RGA identifies gas species present in the plasma by ionizing gas molecules inside the RGA head and separating the species according to the mass/charge ratio. Given that the atomic masses of CO and N₂ are 28.0101 amu and 28.0134 amu respectively, the RGA is not capable of distinguishing between singly-ionized CO and singly-ionized N₂. To eliminate this ambiguity, a preliminary background scan was taken before any CO₂ flowed into the chamber. Assuming that there are no significant leaks in the vacuum system (a good assumption given the low base pressure), the partial pressure of N₂ should not increase with the introduction of CO₂. By subtracting the background scan from all subsequent scans, any resulting partial pressure measurements at the mass/charge ratio of 28 can be taken to correspond to singly-ionized CO.

Figure 4.4 displays the results of the flow rate of species created in the plasma as a function of power with no external magnetic field applied. The input flow rates are shown for 15 sccm and 100 sccm of CO₂ with 10 sccm of Ar. The decline of the CO₂ flow rate is evident in all cases as well as the rise in CO and O₂ flow rates, indicating dissociation has occurred.

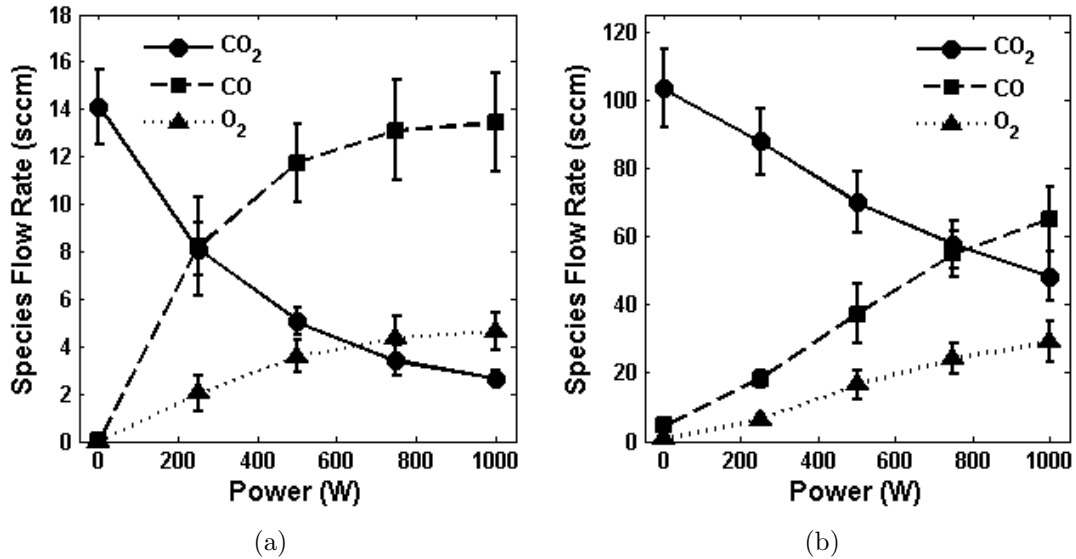


Figure 4.4: Output plasma species flow rate with $\vec{B} = 0$: a) 15 sccm input CO₂ flow rate, and b) 100 sccm input CO₂ flow rate.

From Equation 3.39 of Chapter III describing total CO₂ decomposition, we expect the flow rate of CO to be twice the amount of the flow rate of O₂, however at many of the data points the flow rate of CO is closer to three times that of O₂. This imbalance can be explained by looking at the reaction equations responsible for producing oxygen in the system. The main reactions for the creation of oxygen start with $CO_2 + M \rightarrow CO + O + M$, and ends with $CO_2 + O \rightarrow CO + O_2$. This process assumes that atomic oxygen is free to react with CO₂ to produce molecular oxygen. Instead, atomic oxygen may be participating in the reverse reaction of $O + CO \rightarrow CO_2$ before it can create O₂ and reach the RGA instrument. Additionally atomic oxygen can participate in reactions with carbon created in the discharge to create CO. Therefore, it is likely that atomic oxygen is being utilized in other reactions with carbon-containing species before reaching the RGA rather than creating molecular oxygen.

4.3.1 Applied Magnetic Field Effects

Previous studies of this RF plasma source have shown that the application of an axial magnetic field can produce two competing processes that will affect molecular dissociation. First, the magnetic field lines will confine electrons to the annular volume of the quartz tube closest to the antenna preventing electrons from diffusing to the core of the discharge. This can hinder electron impact reactions from taking place with CO₂ molecules. However, increasing electron confinement also increases the probability of electron collisions in the confined area that can lead to more electron attachment and dissociative attachment processes resulting in dissociation [70]. In Figure 4.5, the effects of the applied magnetic field on the production of CO from CO₂ are shown for (a) 0 A of current and (b) 60 A of current. There is almost no difference between the two cases, indicating that the applied magnetic field has little effect on CO₂ dissociation. The only noticeable difference occurs at the highest flow rate of 100-sccm-CO₂ at 1000 W of input RF power in which case the production of

CO increases from around 65 sccm for 0 A of current to about 78 sccm for 60 A of current. This may indicate that the plasma changes from a capacitive to inductive mode at higher flow rates when the magnetic field is applied. However, due to the ambiguous nature of the results, the effects of the applied magnetic field cannot be confirmed in this study.

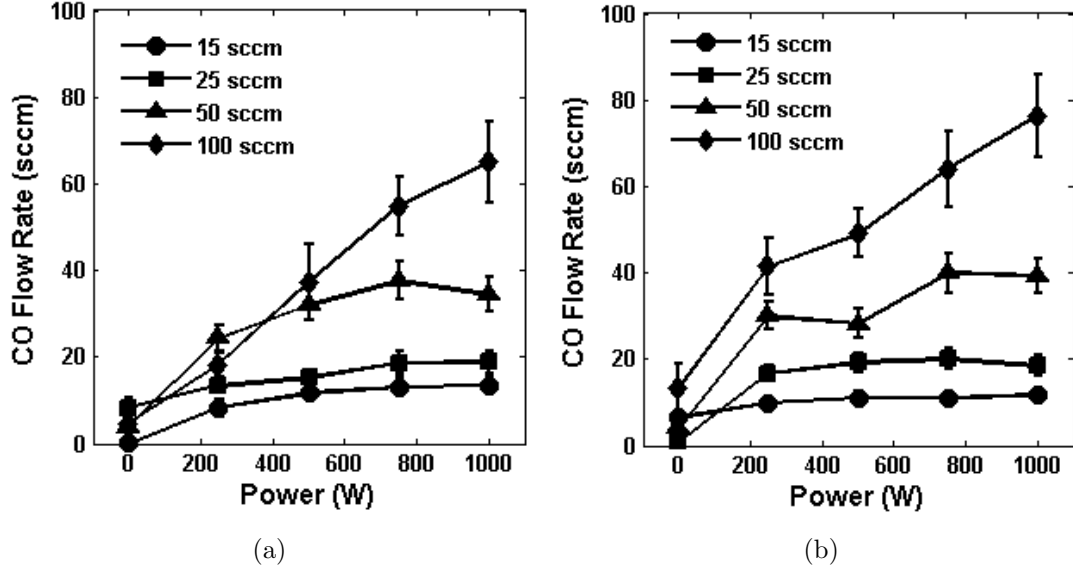


Figure 4.5: Magnetic field effects of CO production: a) 0 A of current, and b) 60 A of current.

4.3.2 Energy and Conversion Efficiencies

In order to determine the effectiveness of this RF discharge for CO₂ dissociation, the energy efficiency and conversion efficiency must be calculated. Energy efficiency as defined in Chapter III is shown again in (4.2) where $\Delta H = 2.9$ eV/mol for CO₂ dissociation and E_{CO} is the actual energy cost of one CO molecule in the system. The actual energy cost can be calculated by taking $E_{CO} = E_v/\alpha$, where E_v is the specific energy input in units of eV/mol and α is the conversion efficiency in units of percentage.

$$\eta = \frac{\Delta H}{E_{CO}} \quad (4.2)$$

$$E_v = \frac{power}{\dot{m}_{CO_2in}} \text{ (eV/mol)} \quad (4.3)$$

$$\alpha = \frac{\dot{m}_{CO_2out}}{\dot{m}_{CO_2in}} \quad (4.4)$$

Therefore the energy efficiency, η , can be written as:

$$\eta = \alpha \cdot \frac{\Delta H}{E_v} = \dot{m}_{CO_2out} \cdot \frac{2.9}{power} \quad (4.5)$$

The results for the calculated efficiencies are shown in Figure 4.6 plotted as a function of specific energy input. The highest energy efficiency achieved is only 3% for a flow rate of 100 sccm at 250 W of power corresponding to the lowest specific energy of 39 eV/mol. However, this operating condition also achieved one of the lowest conversion efficiencies of only 20%. As flow rates decrease, the energy efficiency also decreases while the conversion efficiency increases with respect to specific energy. The conversion efficiency reaches a maximum of about 90% for 15 sccm at 1000 W corresponding to a high specific energy greater than 1000 eV/mol. Given such a high specific energy, it is no surprise that the energy efficiency is very low, only about 0.2%. The inverse relationship between η and E_v is evident in Figure 4.6a as result of (4.5) where $\eta \propto 1/E_v$. In order to increase η the specific energy must decrease or the conversion efficiency must increase. However α is not independent of E_v ; Figure 4.6b shows that α increases as E_v increases. Therefore if we try to increase η by decreasing E_v , α will consequently decrease as well, negating any effects the decrease in E_v may have on η . To successfully increase η , the plasma system must be able to increase the conversion degree without increasing the specific energy input, which essentially requires using techniques other than increasing the input power to increase α . Until this can be accomplished, any plasma system built for CO₂ dissociation will always encounter a trade-off between energy efficiency and conversion efficiency.

The low energy efficiency would imply that electronic excitation must be the

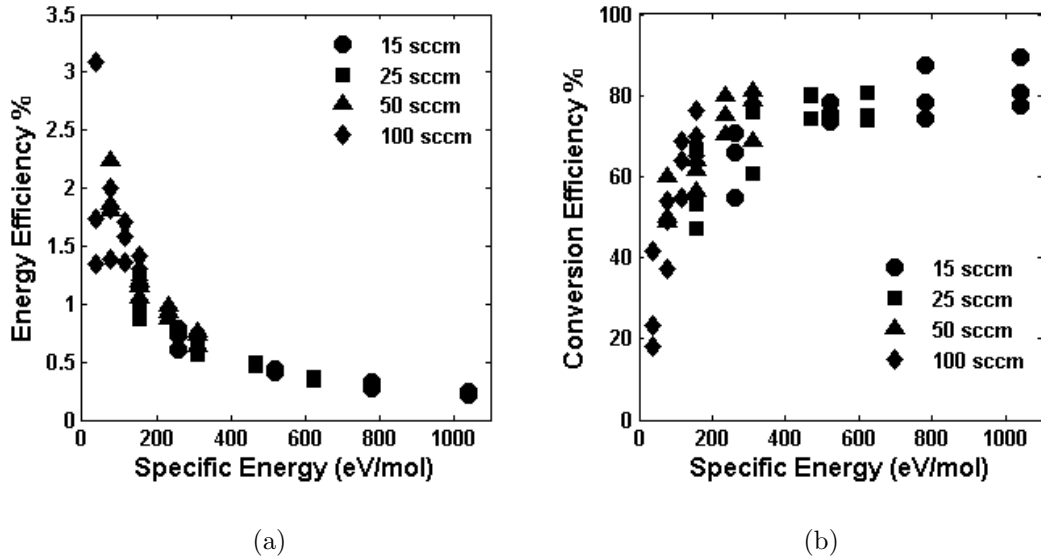


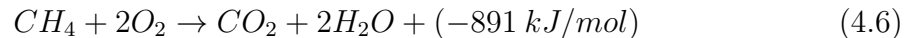
Figure 4.6: Efficiencies of CO₂ dissociation over all flow rates: a) energy efficiency, and b) conversion efficiency.

dominant mechanism of dissociation in this system. The one-step collisional process described in Equation 3.43 requires the electron energy to exceed 8 eV for dissociation to occur, which greatly exceeds the OC=O bond energy. This dissociation mechanism is typically dominant in low-pressure discharges with high values of reduced electric field, which describes the operating conditions used in this experiment. The high electron energies required give rise to the excitation of various other states that do not contribute to dissociation, resulting in low energy efficiency. Also, it is unlikely that helicon mode was ever reached during operation; most likely the discharge remained in capacitive or inductive mode. The operating pressure range on the order of 100 mtorr was too high to excite the helicon mode structure, which typically appears around 1 mtorr with power levels greater than 1 kW based on previous experiments using the experimental setup [60]. This experiment was limited to only 1 kW of input power. Thus, the high electron density characteristic of a helicon plasma was not present to help increase the electron impact events resulting in dissociation.

4.4 Efficiency Requirements

To determine if CO₂ reduction in a low-pressure RF plasma discharge is valid for large-scale applications aimed at reducing atmospheric CO₂ emissions, it is necessary to understand the energy efficiency requirements for such a system to be profitable from an energy standpoint. Therefore the energy required to dissociate CO₂ is be compared with the amount of energy that is released from burning natural gas and coal, and a discussion of how much CO₂ is emitted from burning these fossil fuels will follow. Normally all of the energy released during the combustion of coal and methane would be used to power a specific process. Here it will be proposed to use a portion of that released energy to dissociate the molecules of CO₂ produced during the process, creating a system in which fossil fuels can still be used to produce energy while simultaneously dissociating the CO₂ molecules that are a result of producing this energy.

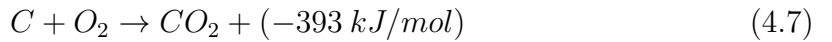
From Equation 3.39 we know that a plasma system used for CO₂ dissociation will require a cost of at least 2.9 eV for every CO₂ reduced to CO. Equation 4.6 describes the combustion of methane (CH₄), which releases 891 kJ/mol of energy, equivalent to 9.25 eV/mol, and creates one molecule of CO₂ for every molecule of CH₄ burned. However, we must consider the conversion efficiency of the natural gas power plant, which can reach as high as 60% [69], leaving us with only 5.55 eV/mol of energy to be consumed.



If the plasma system is 100% energy efficient, only 2.9 eV is required to dissociate the one molecule of CO₂ created by the combustion of one methane molecule. Let's propose that the remaining 5.55 eV released from methane combustion will be used to 'pay' for the dissociation of CO₂. By subtracting the 2.9 eV needed to reduce CO₂ to CO from the total energy output of methane combustion, the resulting net

energy gain is 2.65 eV. This 2.65 eV of energy can be considered ‘clean’ energy and free of any carbon footprint because the CO₂ molecule that is normally emitted into the atmosphere has been dissociated with the energy from combustion. However, realistically the system will not be 100% efficient. With this information, a minimum level of energy efficiency can be defined such that the system will ‘break even’ (i.e. 5.55 eV is released from combustion and 5.55 eV is used to produce one molecule of CO from CO₂). Using (4.2) as the definition of energy efficiency with $E_{CO} = 5.55$ eV/mol (recall that E_{CO} is the actual energy cost of one CO molecule in the system), it can be found that $\eta_{min} = 52\%$. If the energy cost of producing one CO molecule can be lowered, thereby increasing the energy efficiency greater than η_{min} , this will result in an overall net energy gain for the system. For example in the work presented by [87], a 2.4 GHz microwave plasma system operating at moderate pressure of 50 - 200 torr with up to 1.7 kW of microwave power was able to achieve an energy efficiency of 80% [87]. This will result in a net energy gain of 1.9 eV.

A similar analysis can be performed for the combustion of charcoal. Equation 4.7 describes charcoal combustion, which releases 393 kJ/mol of energy, equivalent to 4 eV/mol, and creates one molecule of CO₂ for each molecule of carbon burned. However, the conversion efficiency of convectional coal power plants is only around 35%, leaving just 1.4 eV/mol.



If the plasma system is 100% energy efficient, then 2.9 eV/mol is needed to dissociate CO₂, which is already more than the remaining energy gained from coal combustion. Therefore, there will be a net energy loss if this method is applied for reducing emissions from coal combustion.

This analysis has not included the energy conversion efficiency of the chosen plasma system, which could introduce an additional loss into the calculations, making this technology undesirable for the reduction of CO₂ emissions when any fossil fuel source

is supplying the electrical requirements. A better option may be to use renewable energy sources such as wind or solar power, which do not release any carbon into the atmosphere. However this analysis can provide a general baseline requirement for looking at CO₂ dissociation in plasmas.

4.5 Conclusions

A low-pressure RF plasma source has experimentally shown the capability of dissociating CO₂ to CO and O₂. While the discharge can generate high conversion efficiencies near 90%, the energy efficiency is less than 3% for almost all operating conditions. Therefore this helicon plasma system is not a good candidate for CO₂ emission reductions for either coal or natural gas combustion processes. However, a plasma system that is capable of achieving $\eta > 52\%$ (e.g., microwave discharge) has the possibility to apply this technology to natural gas combustion while still achieving a net energy output. Experimental results have shown that microwave discharges can achieve energy efficiency as high as 90% under certain operating conditions [37]. This high performance stems from the unique ability of microwave discharges to excite the vibrational modes of the CO₂ molecule, which is the most effective path to dissociation. The optimum operating conditions to excite vibrational modes of CO₂ include having a specific energy input of 1 eV/molecule, an electron temperature of 1 eV, and an ionization degree (n_e/n_o) $\geq 10^{-6}$ [37]. The rf plasma source studied in this work did not meet this criteria, which explains the low energy efficiency. However microwave sources operating at moderate pressures have shown that they can meet these conditions, and thus may be a good candidate for CO₂ dissociation.

CHAPTER V

Microwave Plasma/Catalyst System

The low energy efficiency results from the RF plasma in Chapter IV has led to the construction of an atmospheric pressure microwave plasma source, which comprises the bulk of the experimental work for this dissertation. The following chapter describes the development of the microwave plasma/catalyst system, beginning with an explanation of the benefits of microwave discharges for CO₂ dissociation in Section 5.1. The experimental MW system will be illustrated in Section 5.2, followed by the method for introducing catalyst material into the discharge in Section 5.3. The diagnostic techniques and corresponding methods of data analysis will be explained in Section 5.4. The computational program GlobalKin used to model the species reaction mechanisms in the microwave plasma is described in Section 5.5. Lastly, a summary will follow in Section 5.6.

5.1 Benefits of Microwave Plasmas

As briefly stated at the end of Chapter IV, microwave discharges have the potential to achieve high energy efficiencies of CO₂ dissociation. Figure 5.1 shows a plot of energy efficiency as a function of specific energy for various experimental and simulated discharge systems. It is evident that some systems can reach close to $\eta \approx 90\%$. Curves 3 and 4 show simulated results for a non-equilibrium plasma with supersonic flow:

(3)M = 5 and (4)M = 3.5. The open circles, \circ , solid diamonds, \blacklozenge , deltas, Δ , and crosses, \times , represent experimental results in different microwave discharges. The solid circle, \bullet , shows data taken from experiments in supersonic microwave discharges. Other plasmas represented on this plot are thermal discharges with quenching in curves 5-9, experimental RF-ICP discharges, \odot , and arc discharges, $\otimes, *$ [37]. Microwave discharges clearly dominate at attaining the highest energy efficiency, which happens to occur for conditions of $E_v \approx 0.3 - 1$ eV/mol.

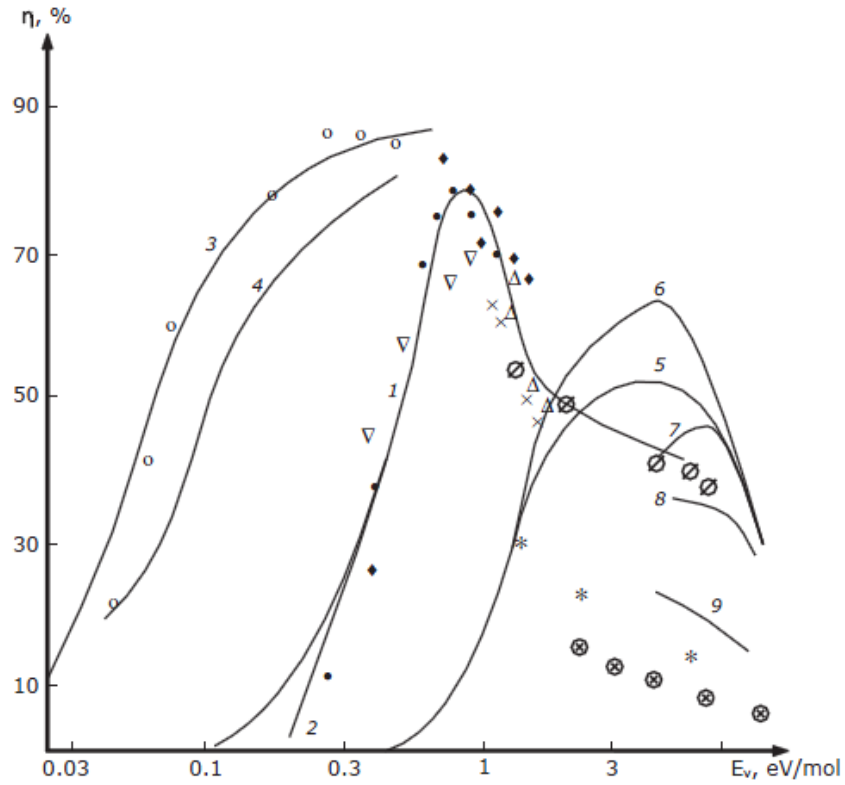
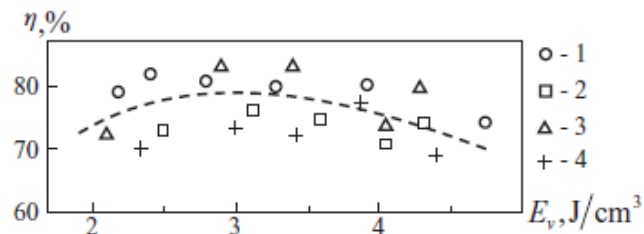


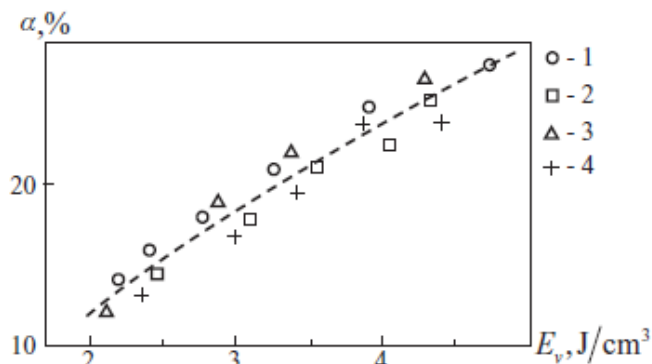
Figure 5.1: Energy efficiency of CO_2 dissociation in various discharges [37].

The experimental microwave systems that reached $\eta = 80 - 90\%$ were performed under non-equilibrium conditions at moderate pressures of 50 - 200 torr with power levels in the 1.5-kW range. CO_2 flow rates were in the range of 0.15 - 2 L/s, resulting in low values of specific energy near 0.8 eV/mol. However the same tradeoff between energy efficiency and conversion efficiency was found in these experiments that was noted in Section 4.3 of the previous chapter. Figure 5.2 summarizes the experimental

results of energy and conversion efficiency for a fixed pressure of 120 torr. Energy efficiency peaks at 80% with a corresponding conversion efficiency of about 20% [37]. Conversion efficiency continues to increase with higher values of E_v , while η begins to decline. However the addition of catalyst material may be able to boost conversion efficiency while maintaining energy efficiency, as discussed in Section 3.3.



(a)



(b)

Figure 5.2: Efficiencies of CO₂ dissociation in a microwave plasma at 120 torr: a) energy efficiency, and b) conversion efficiency. 1) and 2) are data points from different mass-spectral measurements, 3) data from manometric measurements, 4) data from flow-control-based measurements [37].

Another drawback of this microwave system is that it requires the use of a vacuum pump to maintain the pressure around 100 torr. When looking to scale up the system for industrial operation, a vacuum pump brings added cost/energy and complexity. Thus, a system that can achieve similar energy efficiencies at atmospheric pressure would be ideal. Surface wave discharges excited by microwaves have the potential to achieve non-thermal conditions at atmospheric pressure. Figure 5.3 shows spectroscopic results of temperature and density from a surface wave plasma at atmospheric pressure

excited by a 2.45 GHz microwaves. Figure 5.3a clearly shows a non-equilibrium between the electron temperature and the gas temperature for the neon discharge. Gas temperature measurements were obtained from the rotational spectrum of the OH radical present due to trace amounts of water in the discharge. The electron temperature was estimated from the line-to-continuum method using three neon emission lines. High electron densities on the order of 10^{14} cm^{-3} for argon, neon, and helium discharges are plotted in Figure 5.3b, indicating an ionization degree greater than 10^{-6} when operating at atmospheric pressure. Thus, atmospheric pressure surface wave discharges offer a promising option for a cost effective CO_2 dissociation solution.

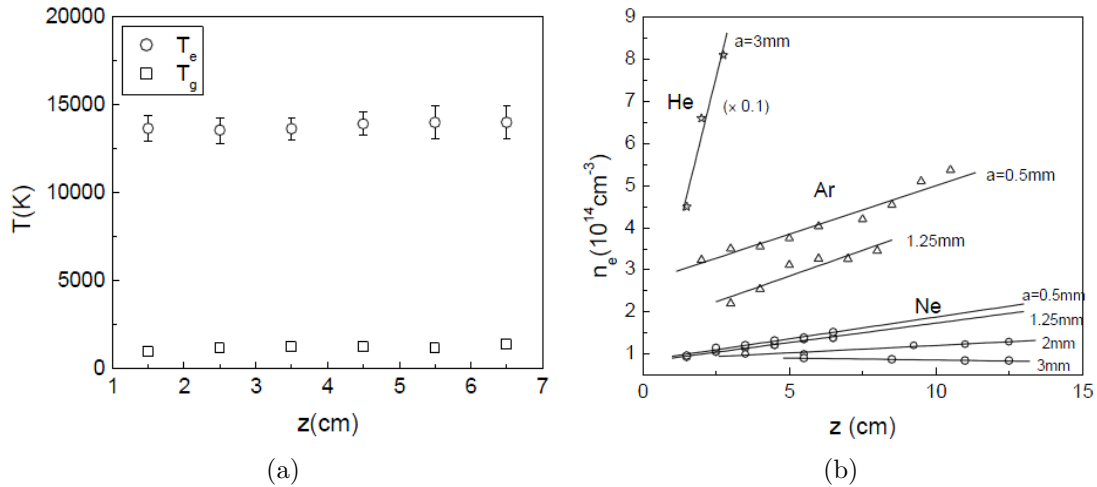


Figure 5.3: Experimental results of a non-thermal surface wave plasma operating at atmospheric pressure: a) electron and gas temperatures, and b) electron density. Density measurements plotted as a function of axial position for different capillary discharge tube diameters denoted by the value of a [88].

5.2 Experimental Setup

5.2.1 Microwave System

All experiments were performed at PEPL in the atmospheric pressure microwave system illustrated in Figure 5.4. The system consists of a water-cooled magnetron head that launches a 2.45-GHz wave powered by a 2-kW power supply, model SM840E

from Alter Power Systems. The power supply has an operating range from 10-100% full power. A water-cooled three-port circulator with 3-kW power capability load attaches to the magnetron head to prevent any reflected power from damaging the magnetron. Any reflected power is diverted to a water-cooled dummy load instead. A dual directional coupler placed next to the circulator is used for forward power and reflected power measurements. Here, crystal detectors convert the RF output signal from the coupler to a DC voltage to be read on analog meters via coaxial cables. Next to the directional coupler, a manual three-stub tuner is used to match the impedance of the plasma to that of the MW power in order to establish the most efficient coupling of microwave energy to the plasma. For the tuner used here, three stubs of metallic element are spaced at $1/4$ guide wavelength intervals and offset $1/16$ guide wavelength from center to be inserted into the waveguide. To enable high power operation, a $1/4$ -wave choke around the stub is used to eliminate electrical current at the interface between the stub and the waveguide wall [52].

The plasma is sustained by the water-cooled *Surfaguide* device, which launches a surface wave along the plasma column [10, 65, 67], as previously described in Section 3.1.3. The *Surfaguide* consists of a standard rectangular waveguide with a reduced height section which the discharge tube pierces perpendicularly through the wide waveguide wall. This reduced height section of waveguide provides a maximum electric field where the MW field crosses the discharge tube, allowing for a highly efficient plasma source. A diagram of the *Surfaguide* is shown in Figure 5.5a.

Extending above and below the *Surfaguide* are two bronze cylindrical waveguides, 33 cm in length, which encase the discharge tube to prevent the emission of microwave radiation. The diameter of the waveguide was designed at the cutoff frequency for a 2.45-GHz wave. Taking Equation 3.33 for the cutoff frequency and taking into account

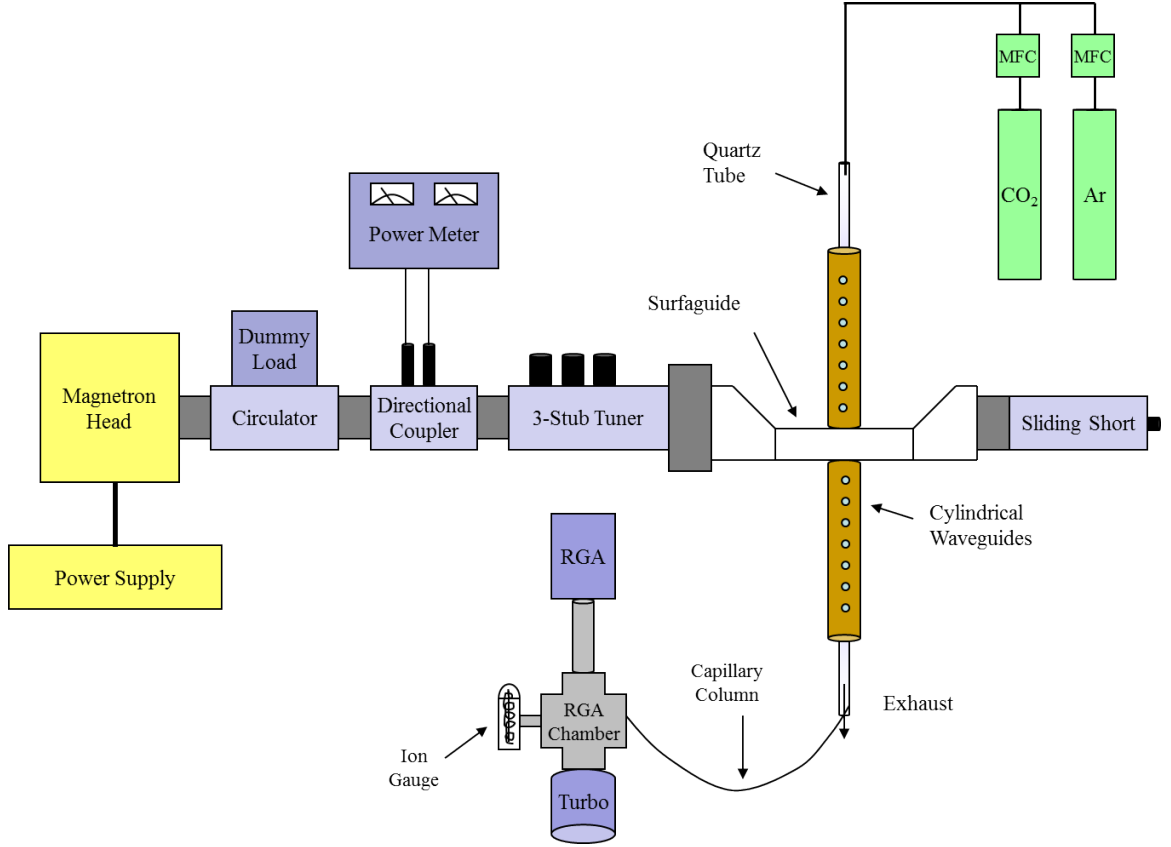


Figure 5.4: Microwave plasma setup.

the eigenvalue solution for the TM_{01} wave mode, the definition of ω_α becomes:

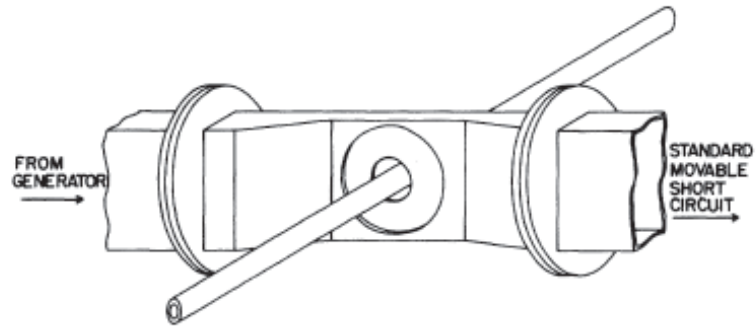
$$\omega_{01} = \frac{\chi_{01}}{\sqrt{\mu\epsilon}R} = c \cdot \frac{2.405}{R} \quad (5.1)$$

where χ_{01} is the first root of the $J_0(R)$ Bessel function, and R is the waveguide radius. For optimization of the *Surfaguide*, the diameter of the cylindrical waveguide should be chosen to achieve cutoff at 2.45 GHz. Thus using Equation 5.1, the diameter is calculated to be 4.6 cm. In order to visualize the plasma and use emission spectroscopy diagnostics, 5-mm inner-diameter (ID) holes spaced 3.8 cm apart were placed axially along one face of each cylindrical waveguide. The hole diameter was designed to

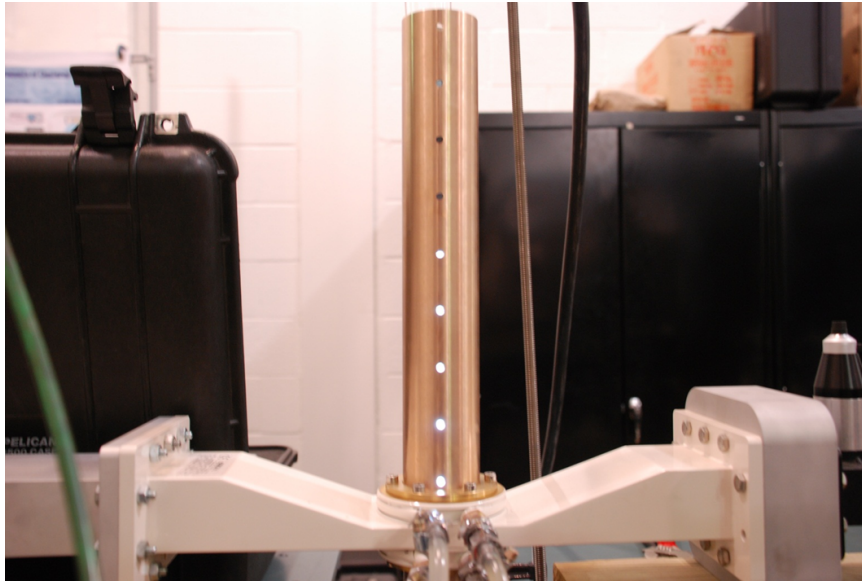
provide a microwave shielding effectiveness (SE) of around 20 dB using Equation 5.2:

$$SE = 20 \cdot \log_{10} \left(\frac{\lambda}{2l} \right) \quad (5.2)$$

where λ is the microwave wavelength and l is the hole diameter.



(a)



(b)

Figure 5.5: Diagram of *Surfaguide*: a) illustration of *Surfaguide* with discharge tube piercing perpendicularly [66], b) picture of actual *Surfaguide* with extending cylindrical waveguide pieces.

Lastly, a sliding short circuit is placed after the *Surfaguide* to help with tuning of the plasma by creating a resonant cavity. Resonant cavities propagate EM energy at specific fundamental frequencies to create efficient wave propagation and absorption

into the discharge. Positioning of the sliding plunger on the end of the short circuit will vary the position of the standing wave created in the waveguide, enabling optimization of the electric field at the location of the plasma load. All waveguide components are rectangular of size WR284 (inner dimensions 2.84×1.34 in), except for the *Surfaguide* and sliding short which are WR340 (inner dimensions 3.40×1.70 in). Thus a waveguide step transition was used to connect the WR284 flange to the WR340. Though WR284 is rated for use in the MW frequency range of 2.60-3.95 GHz, it can be successfully used for 2.45 GHz at power levels below 6 kW. The WR340 is good for power levels up to 20 kW [52].

Ar and CO₂ gas is axially injected from the top of the discharge tube. A combination of Unit and Alicat flow controllers ranging between 10-20 standard liter per minute (slm) are used to regulate the gas flow. Given the potential toxicity of the exhaust gas due to the creation of CO, the exhaust was transferred via tubing to an outside ventilation fan. A port on the end of the discharge tube allows for gas collection at the RGA via fused silica capillary tubing. In order to physically ignite the plasma under atmospheric pressure conditions, a Tesla coil is used capable of outputting between 10,000 and 50,000 V at a frequency around 500 kHz. Using the Tesla coil, a spark is generated at the top of the discharge tube near the axial gas injection location. The microwaves that propagate along the axial direction of the tube will interact with the spark-created electrons to stimulate plasma ignition. This is a quick and effective way of starting the plasma without having to produce a large electric field from the microwave source.

5.2.2 Oil-Cooled Discharge Tube

The design of the discharge tube initially began as a simple 1-cm ID quartz discharge tube. The diameter was chosen based on previous experimental reports and on an analysis of the plasma skin depth. Given that the EM surface wave travels on

the interface between the plasma and the surrounding dielectric, it is necessary to have an estimation of how the EM wave will interact with the flowing gas particles to create chemically active species. The skin depth provides a basic calculation for describing penetration depth of the wave into the plasma. Skin depth is defined as:

$$\delta = \sqrt{\frac{2}{\omega\sigma\mu_0}} = \frac{5.03}{\sigma^{1/2}(\text{Ohm}^{-1} \cdot \text{cm}^{-1}) \cdot f^{1/2}(\text{MHz})} \quad (5.3)$$

where $\omega/2\pi = f$ is the MW frequency, μ_0 is the permittivity of free space, and σ is the plasma conductivity given in Equation 5.4.

$$\sigma = \frac{n_e e^2}{m_e \nu_{en}} = 2.82 \times 10^{-4} \frac{n_e(\text{cm}^{-3})}{\nu_{en}(\text{s}^{-1})} \quad (5.4)$$

Here n_e is the electron density, e is the electron charge, m_e is the electron mass, and ν_{en} is the electron-neutral collision frequency [61]. The collision frequency can be taken as $\nu_{en} = k(T_e) \cdot N_g$, where $k(T_e)$ is the reaction rate coefficient as a function of electron temperature, and N_g is the neutral gas density [37]. Gas density can be calculated using the Ideal Gas Law, $PV = nk_B T$, and $k(T_e)$ can be estimated for $T_e = 1$ eV (chosen based on results shown in Figure 5.3a) from the electron impact cross section of CO₂ for momentum transfer as 6×10^{-8} cm³/s. Using an estimation of electron density of 10^{13} cm⁻³ with a gas temperature range of $T_g = 300 - 3000$ K, the calculated skin depth layer has a range of 7.4 mm to 23.5 mm, corresponding to gas temperatures of 3000 K and 300 K, respectively. Given that it is expected the gas temperature will be closer to the higher end of that range due to melting of the quartz tube, the discharge tube diameter should remain close to 7.4 mm for the electric field to interact with gas particles radially across the tube. This calculation of conductivity uses the cold plasma approximation assuming $\omega \ll \omega_{pe}, \nu_{en}$ [61]. This relation holds true for a wave oscillation frequency, ω , of 2.45 GHz and an electron density of 10^{13} cm⁻³ used to calculate the plasma frequency, ω_{pe} , resulting in the

relation $2.45 \times 10^9 \text{ s}^{-1} \ll 2.84 \times 10^{10} \text{ s}^{-1}, 1.4 \times 10^{11} \text{ s}^{-1}$.

Initial experiments with this tube resulted in melting of the quartz for a pure Ar discharge above 250 W. Any substantial flow rates of CO_2 ($\dot{m} > 100 \text{ sccm}$) require power levels of at least 750 W, so a cooling system had to be developed. The solution was a quartz cooling jacket that surrounds the 1-cm ID, 80-cm long discharge tube. The cooling jacket consists of a larger ID quartz tube of 38 mm that extends 66 cm axially along the central portion of the discharge tube. A cooling fluid other than water must be used to flow through the jacket, since water, as a polar molecule, will interact with and absorb microwave power. A pure silicone fluid named polydimethylsiloxane (PDMS), was chosen as the cooling fluid for its low microwave absorption (loss tangent of $\tan \delta = 3.5 \times 10^{-4}$ [90]), low viscosity, and high optical transmission characteristics [90,91].

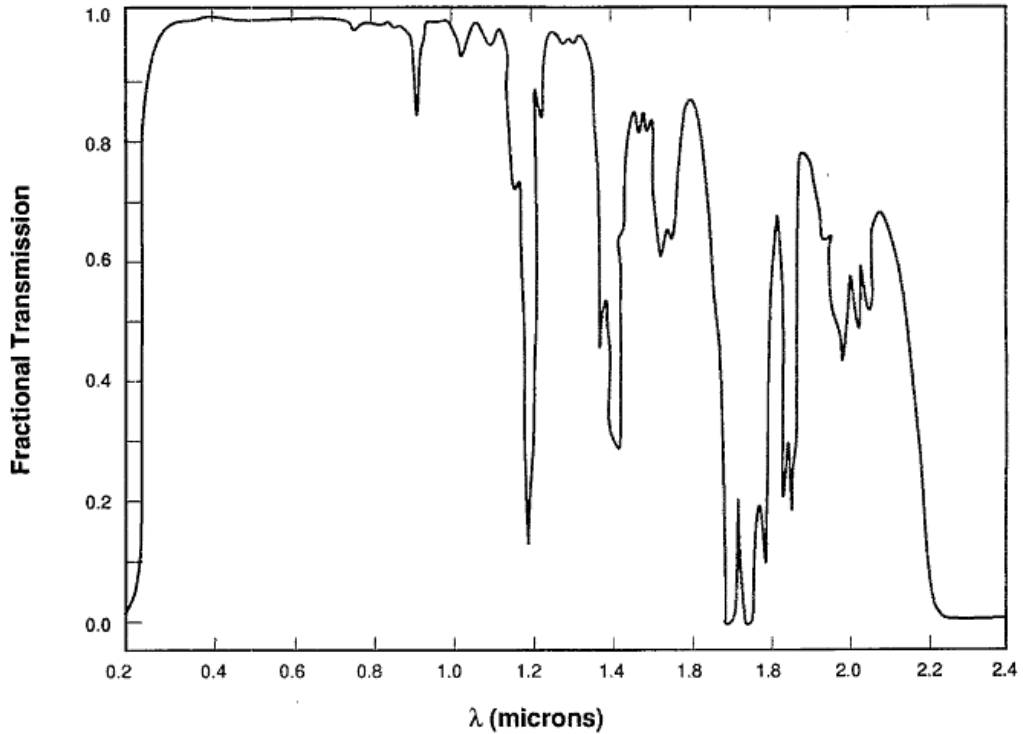


Figure 5.6: Optical and IR transmission of the cooling fluid [90].

PDMS is non-toxic and non-flammable, and can be operated over a wide temperature range $-73^\circ\text{C} - 260^\circ\text{C}$. The microwave absorption has been experimentally

determined for a 2.45 GHz wave to be 0.2 W/cm per kW incident microwave power, which is comparable to that of quartz making it an attractive choice for use with microwave plasmas [90]. Figure 5.6 shows the optical and IR transmission characteristics of the fluid, indicating near 100% transmission in the optical region. A 5-centistokes viscosity PDMS fluid purchased from Clearco passes through a recirculating chiller with heat exchanger, Polyscience Model 6860T, to regulate the fluid at a desired temperature as it cools the discharge tube. For all experiments, the PDMS was set to 7°C and varied on average $\pm 3^\circ\text{C}$ during operation. The PDMS was injected into the cooling jacket via ports of 0.95-cm quartz tubing. Images of the discharge tube with cooling jacket are shown in Figure 5.7.

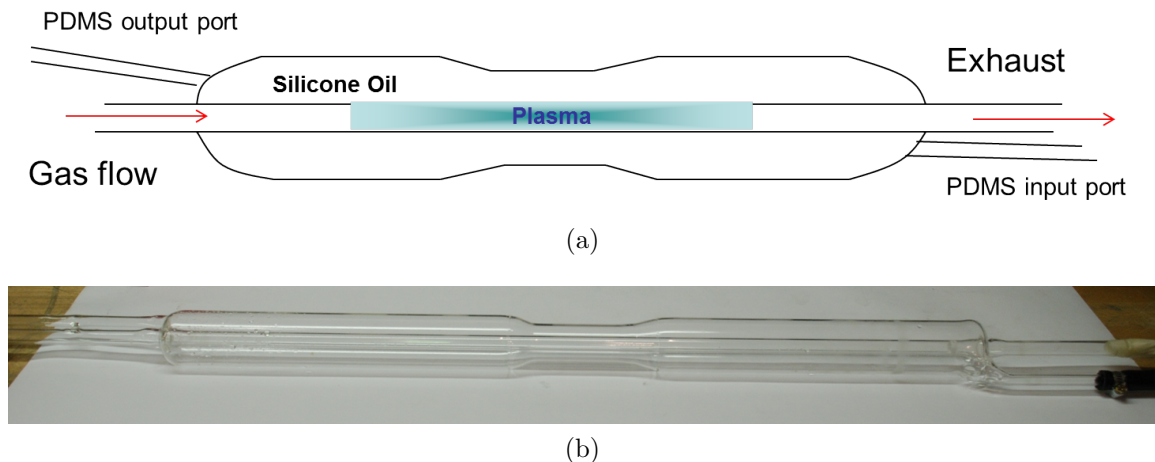


Figure 5.7: Discharge tube with cooling jacket: a) illustration of discharge tube, b) picture of actual discharge tube.

5.3 Catalyst Material

5.3.1 Rhodium-Coated Monoliths

The catalyst material was designed and constructed through collaboration with the University of Michigan Chemical Engineering Department. One of the simplest methods of introducing the catalyst into the plasma system is via cylindrical honeycomb structures called monoliths. Figure 5.8a shows a picture of the actual catalyst monoliths

used in the experimental system. The length of each monolith is about 2 cm and the diameter is just under 1 cm to fit snugly into the quartz discharge tube. The monolith structure is constructed of cordierite (chemical formula $(\text{Mg,Fe})_2\text{Al}_4\text{Si}_5\text{O}_{18}$), a ceramic material with good thermal and electrical insulating capabilities. The melting temperature of this material is 1200°C , and it can be assumed that the plasma temperature is exceeding 1200°C given that the quartz tube had melted, which begins around 2000°C . Hence, the catalyst cannot be placed directly into the discharge region, and is instead placed downstream of the discharge, held in place by a notch in the quartz tube. In this configuration shown in Figure 5.8b, the hot plasma exhaust will flow through the monolith before exiting the discharge tube. During the experiment, a new catalyst was placed into the tube for every change in the CO_2 flow rate operating condition.

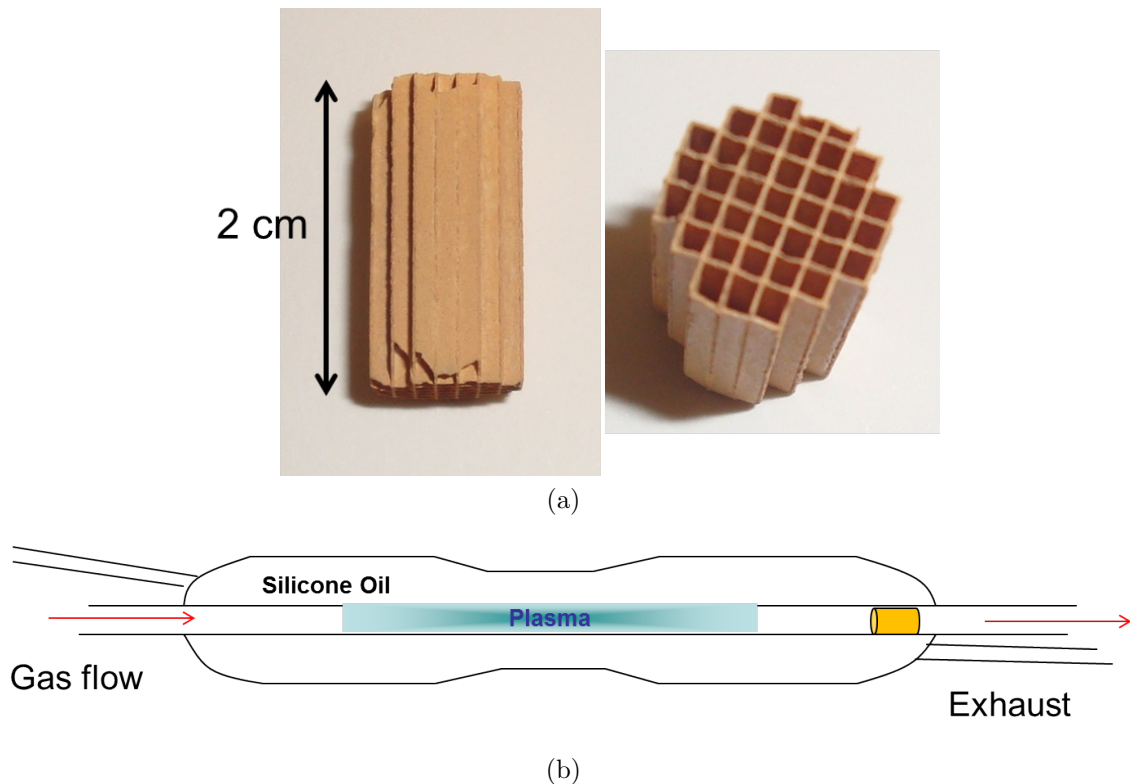


Figure 5.8: Mounting of catalyst material into discharge tube: a) picture of actual catalyst-coated monolith structure, b) illustration of monolith insertion.

The catalyst coating was chosen to be Rh/TiO₂, specifically a 5.5 wt% washcoat loading of 2.5 wt% Rh on TiO₂. Rhodium was chosen for the active phase due to its reported performance in other experimental systems studying CO₂ dissociation. For example, a study performed by [8] compared the effects of different rare metal catalysts on CO₂ dissociation when coated inside an AC glow discharge reactor at atmospheric pressure. A mixture of 2.5% CO₂ in He was passed through the plasma creating CO and O₂ with 80% selectivity. Of the different metal catalyst coatings used, rhodium had the highest reactivity, followed by platinum, copper, palladium, and silver. The CO₂ conversion efficiency as a function of mass flow rate is shown in Figure 5.9, while the energy efficiency is given in Figure 5.10. It is evident that Rh consistently achieved the highest conversion degree over the other metals, and had the highest energy efficiency for the highest CO₂ flow rate tested.

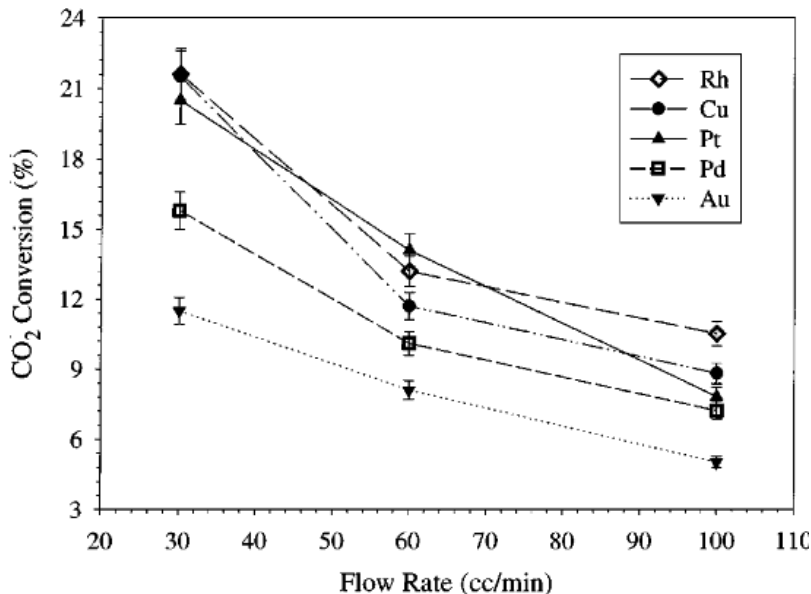


Figure 5.9: CO₂ conversion efficiency for 2.5% CO₂ in He mixture. [8]

The catalyst support, TiO₂, was chosen for its reported ability to increase CO₂ activation. Specifically an experimental investigation was done by [76] comparing CO₂ dissociation on different nickel supported catalysts Ni/Al₂O₃, Ni/SiO₂, and Ni/TiO₂. The rate constant of dissociation was experimentally determined for the reaction over

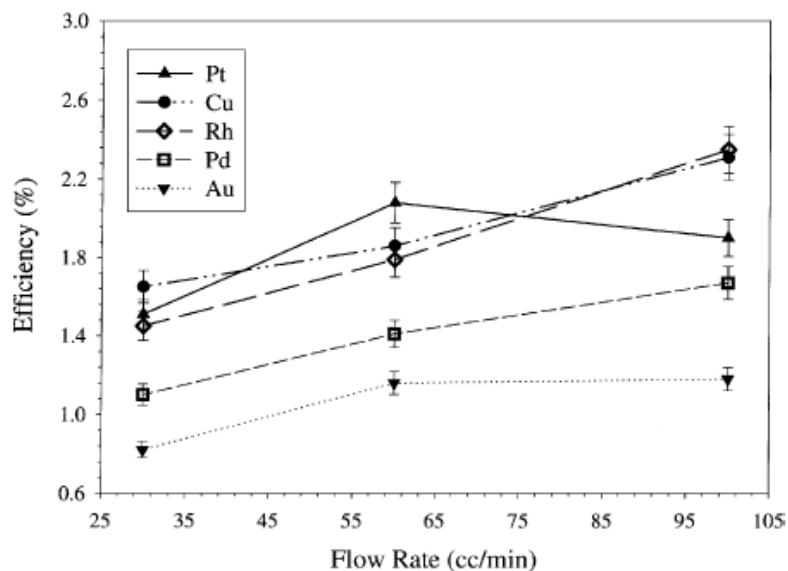


Figure 5.10: CO₂ dissociation energy efficiency for 2.5% CO₂ in He mixture. [8]

each catalyst and the TiO₂ support produced a rate constant about 4 times higher than the other two supports. Another study performed for CO₂ reformation of methane over supported Pt catalysts similarly showed that TiO₂ achieved the highest activity compared to Pt/ZrO₂, Pt/CrO₃, and Pt/SiO₂ [7]. Additionally, a spectroscopic study done on the photoactivation of CO₂ on Rh/TiO₂ has shown that dissociation can occur on the surface of the catalyst [83]. The infrared spectroscopic results showed CO bands in addition to the established spectral features of TiO₂, indicating dissociation had occurred.

5.4 Diagnostics

5.4.1 Residual Gas Analyzer

Similar to the mass spectrometry (MS) diagnostics used in the helicon source experiment discussed in Section 4.2.2, the Stanford Research Systems RGA100 is used in all experiments to identify the species present in the system. Given that the plasma system operates at atmospheric pressure, a comparable differentially pumped RGA

chamber is needed to accommodate the low-pressure requirements of the RGA. Thus the same four-port subchamber is used in this experiment as shown in Figure 4.2, evacuated by the turbomolecular pump attached to one port, the RGA on another port, and an ion gauge for pressure measurement on the third port. Unlike the previous configuration, the fourth port attaches to a capillary column instead of a vacuum chamber. A 0.102-mm ID fused silica capillary column 2 m in length is used to sample gas flowing out of the plasma exhaust. One end of the capillary column is at atmospheric pressure and is inserted into the exhaust end of the discharge tube for plasma species measurement. The low-pressure end of the column is attached to the RGA chamber. The length and ID of this capillary are sufficient to maintain a pressure of 6×10^{-5} torr inside the RGA chamber, while remaining open to atmospheric pressure at one end.

For RGA data analysis, the same empirical formula, Equation 4.1, is used to gain quantitative information from RGA partial pressure readings. Given the operating conditions have changed to atmospheric pressure, with much higher flow rates of Ar and CO₂ (on the order of 1000's of sccm instead of 10's of sccm), new calibration curves were formed. The resulting curves are shown in Figure 5.11, where the curves for each gas are of noticeably different lengths because different flow rate ranges were used for each species with constant Ar flow rate of 8 slm.

As in the error analysis described in Section 4.2.2, all RGA results presented here are the mean values of a sample of measurements. Error bars represent one standard deviation among the spread in the measurement sample. The sample size for the calibration data is four sets with three spectra for each data point, unlike the three data sets used previously. The sample size for the CO₂ plasma species measurements is two sets of data with three spectra for each data point, as before.

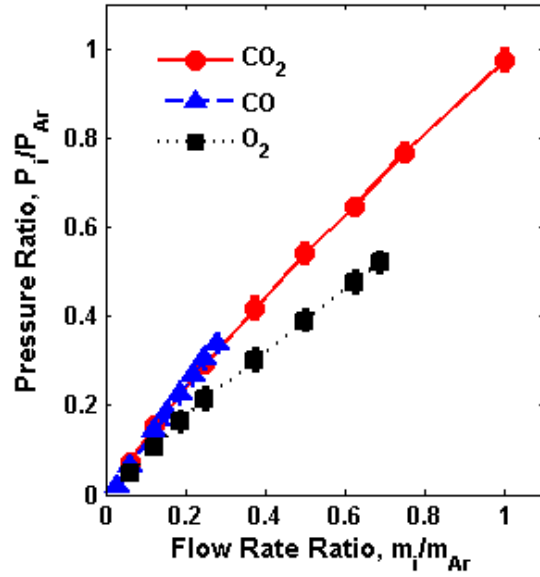


Figure 5.11: RGA calibration curve for capillary configuration.

5.4.2 Optical Emission Spectroscopy

The Ocean Optics HR4000 spectrometer is used to take optical emission spectroscopy (OES) data, capable of measuring emission in the range of 200-1100 nm. With the insertion of a 5 micron slit, data is taken in the visible region from 400 nm - 800 nm with an optical resolution of 0.22 nm at full width at half maximum (FWHM). An Ocean Optics 74-UV fused silica collimating lens with a range of 200-2000 nm is attached to an optical fiber cable 400 microns in diameter which transmits light to the spectrometer. When focused for collimation, beam divergence is 2° or less, depending on fiber diameter, and the lens can be adjusted for UV-VIS or VIS-NIR setups. The collimating lens is mounted on the cylindrical waveguide hole in the position closest to the center of the plasma, where emitted visible light is at its brightest. An illustration of the OES setup is shown in Figure 5.12. Due to the wavelength restrictions of the spectrometer, the C₂ Swan Band system is the only molecular spectra observed during experiments. Thus all OES analysis is completed using the C₂ system.

The spectrometer was calibrated for wavelength using an Ocean Optics HG-1

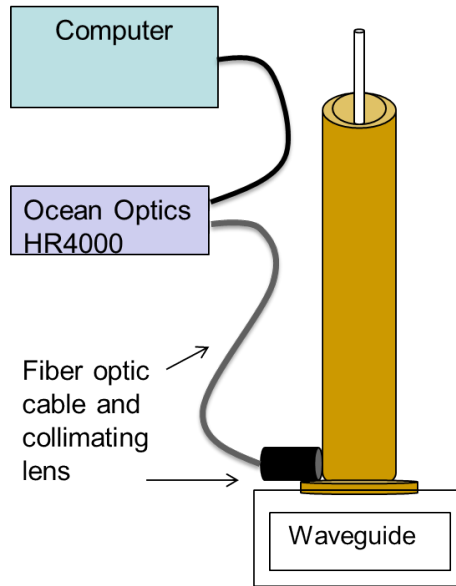


Figure 5.12: Optical emission spectroscopy setup.

mercury-argon lamp as instructed by the spectrometer manual. An intensity calibration was performed using a tungsten filament as a blackbody source. Approximately 3.6-3.8 A of current flowed through the filament, resulting in an operating temperature of around 3000 K for the filament. The relative intensity spectrum of the filament was captured by the spectrometer and used to calculate an intensity calibration factor, Q . Since the tungsten filament can be treated as a blackbody source, Planck's blackbody radiation equation (5.5) can be used to plot the actual blackbody curve for tungsten.

$$I = \frac{2hc^2}{\lambda^5} \cdot \frac{1}{e^{\frac{hc}{\lambda kT}} - 1} \quad (5.5)$$

Here I is intensity, h is Planck's constant, λ is wavelength, and T is the temperature of the tungsten filament. The calibration factor, Q , can be found by taking the intensity ratio of the true (calculated) tungsten blackbody curve to the measured relative tungsten spectrum recorded by the spectrometer. Thus to find the true intensity of any recorded spectrum, the recorded relative emission intensity must be multiplied by Q . Figure 5.13 demonstrates the difference between a relative spectrum and the

corrected spectrum for the experimentally observed C₂ Swan Band system.

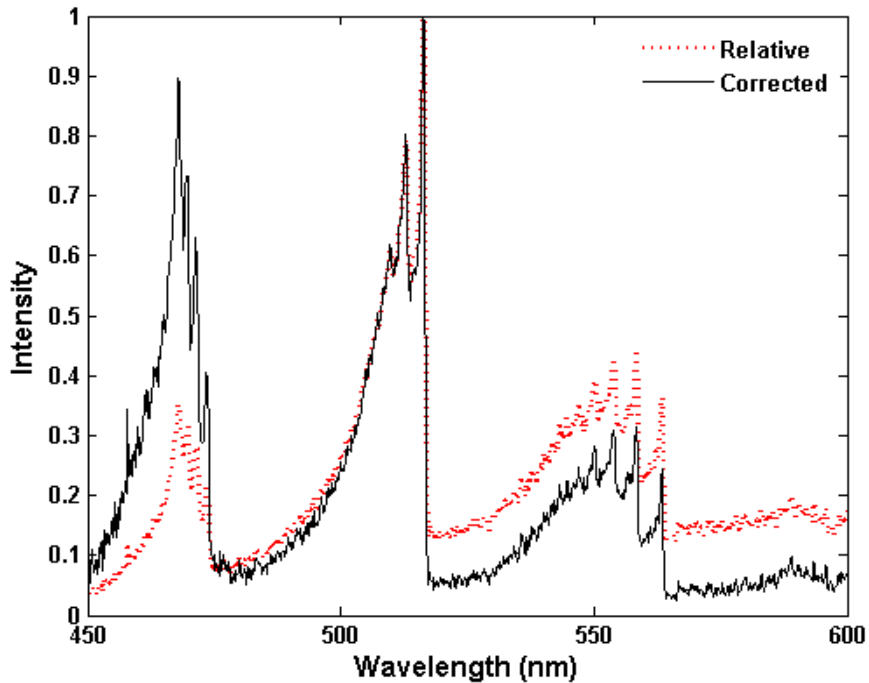


Figure 5.13: Relative vs. corrected spectrum of the C₂ Swan Band

Temperature analysis of the emission spectrum is performed using the program SPECAIR version 2.2 available for free download here [15]. SPECAIR is a radiative modeling program used to model the absolute intensity spectral radiation emitted by air plasmas in the range of 80 nm to 5.5 μm . This is a widely used program for analyzing atmospheric pressure air plasmas as shown here [59, 63, 95, 97, 100]. SPECAIR specializes in air plasma species and can model 37 molecular transitions of NO, N₂, N₂⁺, O₂, CN, OH, NH, C₂, and CO as well as the atomic lines of N, O, and C. The program has several user inputs including different values for electronic, rotational, translational, and vibrational temperatures. The system specifications include operating pressure, wavelength range, species mole fractions, and radiative transitions. For the given user inputs, SPECAIR will output a simulated spectrum which can be compared to experimental results. Thus by varying the temperature inputs for a specific operating condition until the computed spectrum matches the

experimental spectrum, an estimation of plasma temperatures can be found. An example of the agreement between simulated and experimental spectra for the C₂ Swan Band is shown in Figure 5.14.

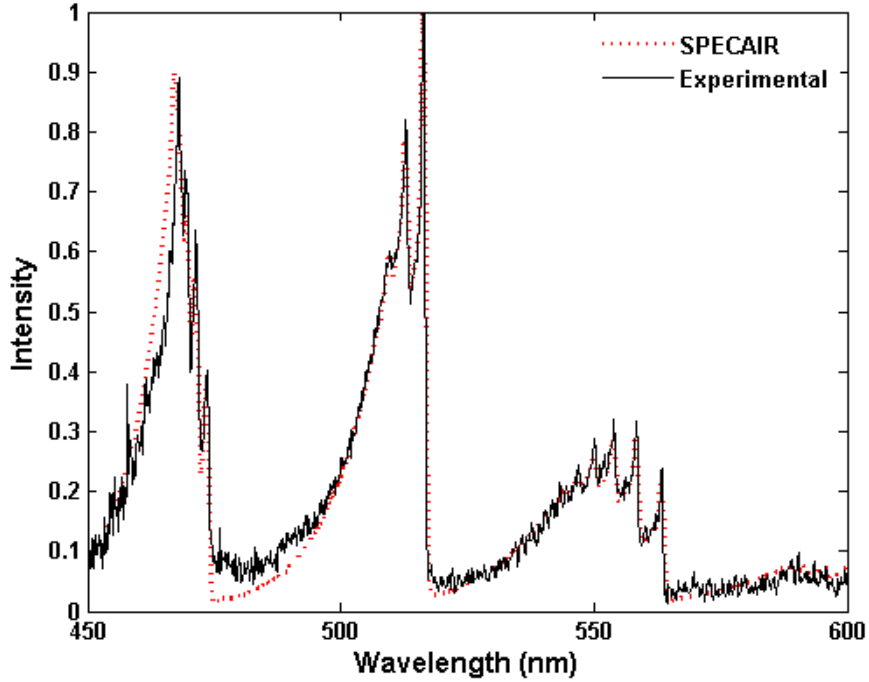


Figure 5.14: Comparison of SPECAIR spectrum to experimental spectrum

Before the simulated spectrum can be compared to experimental spectrum, it must first be corrected for instrumental broadening from the spectrometer. All observed spectra will be broadened due to the finite resolution of the spectrometer, which is a function of the slit width and grating used. For temperatures in the range of 300-6000 K, instrumental broadening is the main contribution to spectral line broadening [80]. The instrumental broadening can be well approximated by a Gaussian profile as a function of wavelength, λ [56, 80]:

$$G(\lambda_0) = \frac{2}{\Delta\sqrt{\pi}} \exp\left(-\frac{(\lambda - \lambda_0)^2}{(\Delta/2)^2}\right) \quad (5.6)$$

where Δ is the instrumental broadening, taken as the spectrometer resolution at

FWHM measured at wavelength λ_0 . A convolution of the slit function (5.6) with the SPECAIR spectrum will provide an appropriately broadened simulated spectrum which can be accurately compared to the observed spectrum.

The relationship between molecular emission spectra and temperature is complex. As excited electrons inside molecules transition to different energy states, quanta of energy, called photons, are released or absorbed in the process. The wave number, ν of the emitted or absorbed photon is given by:

$$\nu = \frac{E_1}{hc} - \frac{E_2}{hc} \quad (5.7)$$

where E_1 and E_2 are the energy states [41]. The energy of the emitted photon is the sum of the energies of the electronic, vibrational, and rotational transitions. The wavelength of such a transition can be defined in the Dunham series format as:

$$\lambda_{B_{v''},J''}^{C_{v',J'}} = \left\{ n_a \sum_{p=0}^5 \sum_{q=0}^2 Y_{pq}^C \left(v' + \frac{1}{2} \right)^p [J'(J'+1)]^q - Y_{pq}^B \left(v'' + \frac{1}{2} \right)^p [J''(J''+1)]^q \right\}^{-1} \quad (5.8)$$

where n_a is the index of refraction and Y_{pq} are constants related to the rovibrational transition [3]. The vibrational quantum numbers for the transition from state E' to E'' are given by v' and v'' , respectively. Likewise J' and J'' represent the rotational quantum numbers. The values of Y_{pq} for the Swan system ($d^3\Pi_g \leftrightarrow a^3\Pi_u$) can be found here [3, 16].

The emission intensity corresponding to an emitted photon due to a transition from an upper state to a lower state is given by:

$$I_{J''}^{J'} = \frac{K}{\lambda^4} q_{v',v''} \exp\left(-\frac{E_{v'}}{k_B T_v}\right) S_{J',J''} \exp\left(-\frac{E_{J'}}{k_B T_r}\right) \quad (5.9)$$

where K is a geometrical constant, λ is the wavelength of the transition given by (5.8), T_v is the vibrational temperature, and T_r is the rotational temperature. The term $q_{v',v''}$

is called the Frank-Condon factor and values for the C₂ system are found here [3, 16]. $S_{J',J''}$ is the line strength intensity called the Hönl-London factor, which is described in more detail in Appendix A.

Finally, the related upper state energies $E_{J'}$ and $E_{v'}$ for rotational quantum number J' and vibrational quantum number v' , respectively, are given below [3]. The combination of Equations 5.8, 5.9, and 5.10 can give a computed emission spectrum for a specific rotational and vibrational temperature.

$$E_{J'} = hc \sum_{p=0}^5 \sum_{q=1}^2 Y_{pq}^C \left(v' + \frac{1}{2} \right)^p J'^q (J' + 1)^q \quad (5.10a)$$

$$E_{v'} = hc \sum_{p=1}^5 Y_{p0}^C \left(v' + \frac{1}{2} \right)^p \quad (5.10b)$$

The Swan system has three observed vibrational band heads in the experimental emission spectrum, $\Delta v = 0$ at 516.5 nm, $\Delta v = 1$ at 563.5 nm, and $\Delta v = -1$ at 473.7 nm. Using SPECAIR, the rotational temperature can be manipulated to broaden or narrow the vibrational band width of the simulated spectrum until matching the experimental spectrum. Similarly, the vibrational temperature can be adjusted to increase or decrease the intensities of rotational band heads in relation to one another until a match is found. The electronic temperature can be calculated from the comparison of intensities of two or more atomic emission lines of the same atom. However, the experimental spectrum contains only one clear atomic emission line for oxygen at 777 nm. Though variation of the electronic temperature in SPECAIR does result in changes of the emission intensity, which can be used to match the temperature to an experimental spectrum. Because of fast collisional relaxation at atmospheric pressure, the translational gas temperature is taken to equal the rotational temperature for all spectra simulations [58, 63].

5.5 GlobalKin

5.5.1 Description of Model

GlobalKin is a zero-dimensional global kinetics plasma simulation used primarily to model the plasma chemistry of gas phase reactions [4, 17, 96]. The model is comprised of three main modules used to perform the calculations. An external Boltzmann solver is used to solve Boltzmann's equation to obtain the electron energy distribution functions (EEDFs), which are needed to compute rate coefficients for electron-impact reactions. The rate coefficients are an input for the reaction chemistry and transport module, which generates differential equations describing the time evolution of species densities and temperatures. These differential equations are integrated using the third module, a stiff ordinary differential equation (ODE) solver which presents results for species density and temperature as a function of time or position. A schematic diagram of the three modules and how they interact is shown in Figure 5.15.

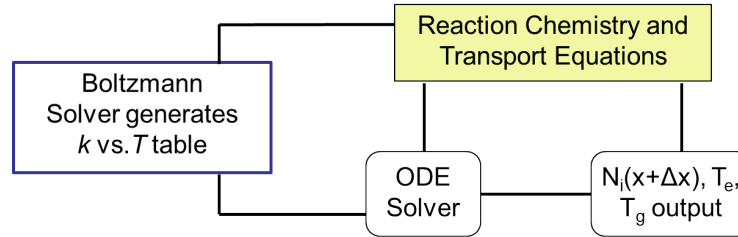


Figure 5.15: Diagram of GlobalKin modules.

For a given set of plasma species and reaction equations, the chemistry and transport module will first begin to develop continuity equations for each neutral (N_i) and charged (N_i^\pm) species, as shown in Equations 5.11 and 5.12, respectively [96]. The first two terms of Equation 5.11 account for diffusion to and from the wall, where D_i is the regular diffusivity of species i in the mixture and the sum over all species. The constant γ_j is the wall reactive sticking coefficient, and f_{ji} is the returned fraction of species j as species i from the wall. The term S_i is the source term for reactions, and the last term accounts for the change in gas temperature (T_g) due to gas expansion

assuming constant pressure operation. Similarly in Equation 5.12, there are diffusion losses to the wall and a source term for reactions. Here $D_{a,i}$ represents the ambipolar diffusivity of species i , which is a function of ion and electron mobilities [4, 96].

$$\frac{dN_i}{dt} = -\nabla \left(-\gamma_i D_i \nabla N_i + \sum_j \gamma_j f_{ji} D_j \nabla N_j \right) + S_i - \frac{N_i}{T_g} \frac{dT_g}{dt} \quad (5.11)$$

$$\frac{dN_i^\pm}{dt} = -\nabla (-D_{a,i} \nabla N_i) + S_i \quad (5.12)$$

The above equations can be simplified using the assumption of a spatially uniform plasma. Thus the second order partial derivatives can be approximated by a diffusion length term of $1/\lambda^2$:

$$\frac{dN_i}{dt} = \frac{1}{\lambda^2} \left(-\gamma_i D_i N_i + \sum_j \gamma_j f_{ji} D_j N_j \right) + S_i - \frac{N_i}{T_g} \frac{dT_g}{dt} \quad (5.13)$$

The source term, S_i , for gas phase reactions and electron-impact reactions takes into account the reactants (left-hand-side, LHS) and products (right-hand-side, RHS) for a given reaction. Given in Equation 5.14, the term a_{ij} is the stoichiometric coefficient of species i in reaction j for each side of the reaction [4, 96]. The reaction rate coefficient, k_j , is computed from EEDFs for electron-impact reactions and from Arrhenius expressions for gas phase reactions.

$$S_i = \sum_j (a_{ij}^{RHS} - a_{ij}^{LHS}) k_j \prod_l N_l^{a_{lj}^{LHS}} \quad (5.14)$$

The differential equation for electron energy can be described using a power balance equation. The only source considered in the model for electron energy is the energy transferred from the applied electric field to electrons in the form of Joule heating.

The first term in Equation 5.15 represents this energy source.

$$\frac{d}{dt} \left(\frac{3}{2} n_e k_B T_e \right) = \vec{j} \cdot \vec{E} - \sum_i n_e \frac{2m_e}{M_i} k_{m_i} N_i \frac{3}{2} k_B (T_e - T_i) - \sum_l n_e k_l N_l \Delta \epsilon_l \quad (5.15)$$

The second term of (5.15) represents energy loss from elastic collisions while the last term is energy loss from inelastic collisions. Here M_i is the mass of the heavy collisional partner, T_i is the heavy gas temperature, k_B is Boltzmann's constant, and $\Delta \epsilon_l$ is the required energy for the excitation process to occur [4, 96].

A similar differential equation can be constructed for T_g using energy balance principles:

$$\begin{aligned} \frac{d}{dt} (N c_p T_g) = & \sum_i n_e \frac{2m_e}{M_i} k_{m_i} N_i \frac{3}{2} k_B (T_e - T_i) + \sum_j n_e k_j N_j \Delta \epsilon_j \\ & - \sum_j \Delta H_j - \frac{\kappa}{\Lambda^2} (T_j - T_w) - \frac{d}{dt} \left(\frac{1}{2} M_w N v_x^2 \right) \end{aligned} \quad (5.16)$$

Unlike the electron energy equation, elastic and inelastic collisions are contributing sources for the gas temperature equation, represented by the first two terms. Energy losses appear in the last three terms. First, ΔH_j is the heat of reaction for process j . The next term represents conduction loss to the wall, where κ is the mixture averaged thermal conductivity, Λ is the diffusion coefficient, and T_w is the wall temperature. The last term accounts for energy loss as the gas expands and flow velocity, v_x , increases, where M_w is the mixture averaged molecular weight [4, 96].

Each of these differential equations outlined above requires the input of a reaction rate coefficient, which are dependent upon the EEDFs generated by the external Boltzmann solver. The Boltzmann module solves Boltzmann's equation (5.17) to determine the EEDF [61].

$$\frac{\partial f}{\partial t} + \mathbf{v} \cdot \nabla_r f + \frac{\mathbf{F}}{m} \cdot \nabla_r f = \left(\frac{\partial f}{\partial t} \right)_{collision} \quad (5.17)$$

The EEDF, $f(\epsilon)$, obtained from (5.17) is then used to compute reaction rate coefficients, k_i , for electron-impact reactions:

$$k_i = \int_0^{\infty} f(\epsilon) \left(\frac{2\epsilon}{m} \right)^{1/2} \sigma(\epsilon) d\epsilon \quad (5.18)$$

Here ϵ is the electron energy in eV and $\sigma(\epsilon)$ is the electron-impact cross section. A database of cross sections for any given input reaction is accessed in GlobalKin for this computation. For gas phase reactions, the Arrhenius equation is used to compute the rate coefficient, shown in Equation 5.19 where A is the pre-exponential factor, E_a is the activation energy, and b is the gas temperature exponent, all empirically derived [102]. The factor R_u is the universal ideal gas constant. GlobalKin accesses a database of the empirical factors for computation.

$$k(T_g) = AT_g^n \cdot \exp(-E_a/R_u T_g), \quad (5.19)$$

Using this information, the Boltzmann module generates a table of values for average electron energy, reaction rate coefficients, and transport coefficients for a range of reduced electric field (E/N) values which are imported to GlobalKin for further calculations. Since the gas composition can be constantly changing and affecting the EEDF, the Boltzmann solver is invoked at specific user-defined intervals throughout the computation to maintain an updated EEDF for each computation. The differential equations can now be solved using the ODE solver described here [9].

5.5.2 CO₂ Microwave Plasma Model

The Ar/CO₂ experimental discharge can be modeled in GlobalKin using 26 different neutral, charged, and excited species of Ar, CO₂, O, O₂, O₃, CO, and C. To correspond with these species, there are 201 reaction equations of electron-impact and gas phase reactions, shown in Appendix B. Given the importance of vibrationally excited species,

Table 5.1: Additional electron impact reactions for vibrational species

(a) CO ₂ (V) reactions	
Momentum Transfer	$e + CO_2(V) \rightarrow CO_2(V) + e$
Vibrational De-excitation	$e + CO_2(V) \rightarrow CO_2 + e$
Dissociative Attachment	$e + CO_2(V) \rightarrow O^- + CO + e$
Electronic Excitation	$e + CO_2(V) \rightarrow CO_2(V) + e$
Ionization	$e + CO_2(V) \rightarrow CO_2(V)^+ + e + e$
Momentum Transfer	$e + CO_2(V)^+ \rightarrow CO_2(V)^+ + e$
Dissociative Recombination	$e + CO_2(V)^+ \rightarrow CO + O$
(b) CO(V) reactions	
Momentum Transfer	$e + CO(V) \rightarrow CO(V) + e$
Vibrational De-excitation	$e + CO(V) \rightarrow CO + e$
Dissociation	$e + CO(V) \rightarrow C + O + e$
Electronic Excitation	$e + CO(V) \rightarrow CO(V) + e$
Dissociative Ionization	$e + CO(V) \rightarrow C^+ + O + e + e$
	$e + CO(V) \rightarrow O^+ + C + e + e$
Momentum Transfer	$e + CO(V)^+ \rightarrow CO(V)^+ + e$
Dissociative Recombination	$e + CO(V)^+ \rightarrow C + O$

cross sections for vibrationally excited CO₂ and CO (CO₂(V) and CO(V)) were added to the GlobalKin database. The additional reaction mechanisms are displayed in Table 5.1.

The microwave plasma is modeled under plug flow conditions, in which gas concentrations are calculated as a series of infinitely thin 'plugs'. Each plug has a different composition from the ones before and the ones after it, traveling in the axial direction of the tube. The plugs are considered perfectly mixed and radially uniform in composition, however species densities are constantly changing in the axial direction. Thus, densities are computed as a function of length along the discharge tube. Figure 5.16 shows a diagram of a plug flow reactor. The physical characteristics of the plug flow reactor are modeled to mimic the experimental microwave system. Thus the discharge tube radius is given to be 5 mm, and the input gas flow rate is 10 slm for Ar and ranges from 1-8 slm for CO₂. The length of the reactor is considered from the axial position of plasma formation to the end of the tube to be 65 cm.

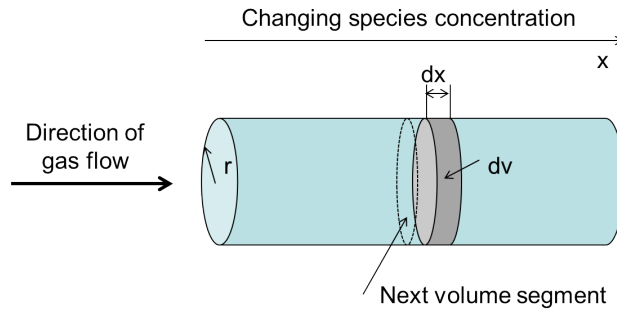


Figure 5.16: Plug flow diagram.

Under the plug flow regime, microwave power deposition is specified as a function of downstream position. In the experimental system, microwave power is at a maximum in the center of the discharge tube and decreases in both axial directions away from the tube. The total plasma length is estimated at 25 cm, after which point microwave power ceases to be applied to the discharge tube. While the length of the plasma may vary slightly with power in experimental systems, the plasma length and power deposition profile was kept constant for all computations. Changes in plasma length did not have a significant effect on the final species calculations. The power deposition profile is shown in Figure 5.17 for four different microwave power levels. Here the total power is specified along with the relative distribution of power as a function of position.

5.6 Summary

In summary, this chapter has served to provide a layout and motivation of the experimental design. A detailed description of the atmospheric pressure microwave system has been given along with the chosen configuration of adding catalyst material into the discharge. The primary diagnostic tools, MS and OES, have also been described along with a description of the computational program used to model the plasma system.

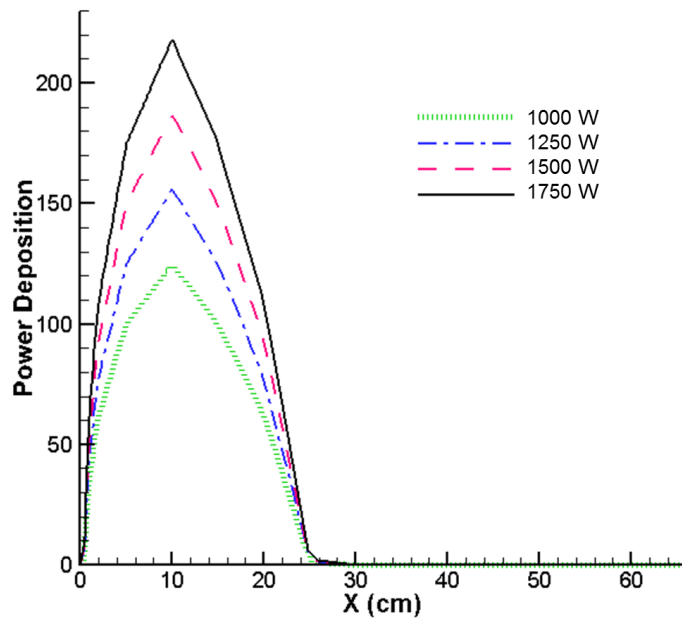


Figure 5.17: Power deposition profile.

CHAPTER VI

Results and Discussion

The results of experimental and computational work performed for the systems described in Chapter V will now be presented. First in Section 6.1 the results of CO₂ dissociation in the plasma system alone will be discussed along with the plasma properties derived from OES measurements. Next the results of the plasma/catalyst system along with the control test using an uncoated monolith inserted into the plasma will be shown in Section 6.2. A comparison of computational results from GlobalKin simulations with the pure plasma system is given in Section 6.3. A discussion of all results will follow in Section 6.4 along with a cost analysis comparison of existing technological approaches. Lastly a summary of the experimental and computational work will be given in Section 6.5.

6.1 Plasma System Results

6.1.1 Initial Plasma Observations

The experimental parameters that were varied include microwave input power, CO₂ flow rate, and Ar flow rate. In order to sustain a discharge with CO₂ flow rates greater than 1 slm, microwave power is required to be equal to or exceed 1 kW. Thus, the power level ranged from 1-2 kW for all tests. As described in Section 5.1, the ideal value for specific energy input to achieve energy efficient dissociation is around

$E_v = 1$ eV/mol. Therefore at the stated power level used, this corresponds to CO₂ flow rates in the range of 15-31 slm. Due to operating constraints at atmospheric pressure, experimental CO₂ flow rates range from 1-16 slm. At such high flow rates, CO₂ alone is not able to sustain a discharge and Ar is required to be injected simultaneously. In the previous experiments described in Chapter IV, Ar is only used at small flow rates as a calibration gas for RGA data analysis. However in the microwave atmospheric pressure plasma, Ar functions as a calibration gas as well as a discharge stabilizing gas. The presence of Ar helps to sustain the discharge by providing electrons to the plasma. Therefore, experimental Ar flow rates were significantly higher than previously used, varying from 6, 8, and 10 slm.

Initially the plasma is ignited using the Tesla coil with a background gas of pure Ar. Then CO₂ gas is injected and flow is slowly increased until reaching the desired operating condition. The presence of CO₂ changes the discharge characteristics dramatically. As CO₂ is introduced into the discharge, the energy switches to vibrational excitation of CO₂ rather than ionization; hence the need for Ar since it can be easily ionized. Figures 6.1 and 6.2 show how the optical emission spectrum changes with the addition of 1 slm CO₂ into a background of 8 slm Ar at 1 kW of input power. The strong intensity Ar neutral lines from 700-800 nm are the dominant species present in the spectrum for the pure Ar discharge. With the addition of CO₂ in Figure 6.2, most of the Ar neutral lines suffer a significant reduction in intensity and the dominant spectral lines become the C₂ Swan band system showing band heads at (0,0), (1,0), and (0,1), 516, 473, 562 nm respectively [79]. A weaker O I line is also present at 777 nm as well as O II around 425 nm.

The absence of the Ar neutral lines indicates that most of the Ar is becoming ionized and serving as the main electron production mechanism. The presence of the Swan system indicates that carbon is being generated either from CO₂ or CO. It is unlikely that the reaction $CO_2 \rightarrow C(s) + O_2$ is responsible because of the high-energy

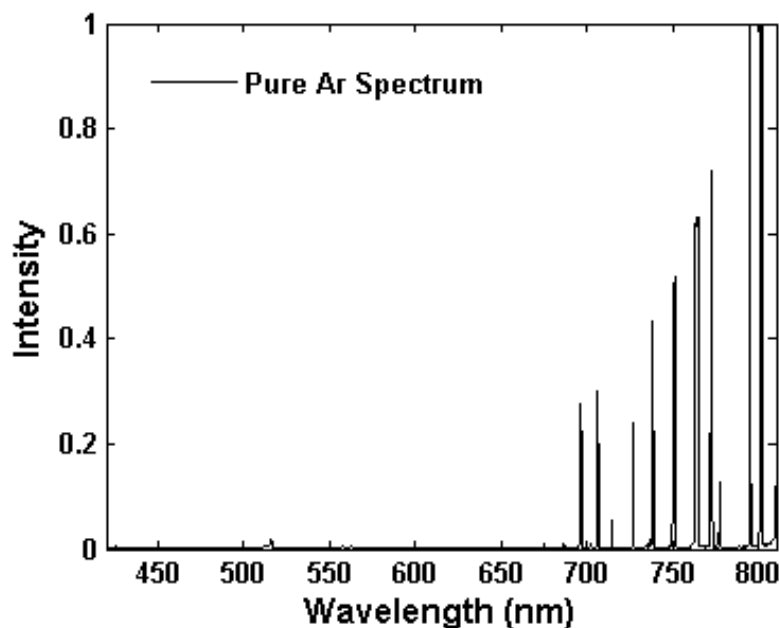


Figure 6.1: Pure Ar normalized emission spectrum at 1 kw. Ar flow rate is 8 slm.

electrons required, $\Delta H = 11.5$ eV/mol. However the reaction $CO + CO \rightarrow CO_2 + C$ requires only 5.5 eV/mol with activation energy $E_a = 6$ eV. This leads to the formation of C atoms in the gas phase free to combine with other carbon atoms to form C_2 . This reaction is accelerated by vibrational and electronic excitation of CO molecules, which is easily stimulated in non-equilibrium plasmas [37]. The intensity of the C_2 band is actually about two orders of magnitude weaker than the Ar emission intensity, due to the rapid reverse reaction $C + CO_2 \rightarrow CO + CO$ with $E_a = 0.5$ eV. There are no CO_2 bands in the spectrum because CO_2 is transparent in the visible region [79].

In addition to changes in the emission spectrum, the plasma also visibly changes in color and discharge characteristics. These changes were observed in a simple 1-cm ID quartz discharge tube, prior to the addition of the cooling jacket. Without the oil-cooling jacket impeding view, the discharge could be clearly examined. Figure 6.3a shows the pure Ar discharge as light blue in color and very contracted and filamentary. With the addition of only about 1% CO_2 as shown in Figure 6.3b, the discharge becomes a light green color and less contracted. The plasma length also shortens with

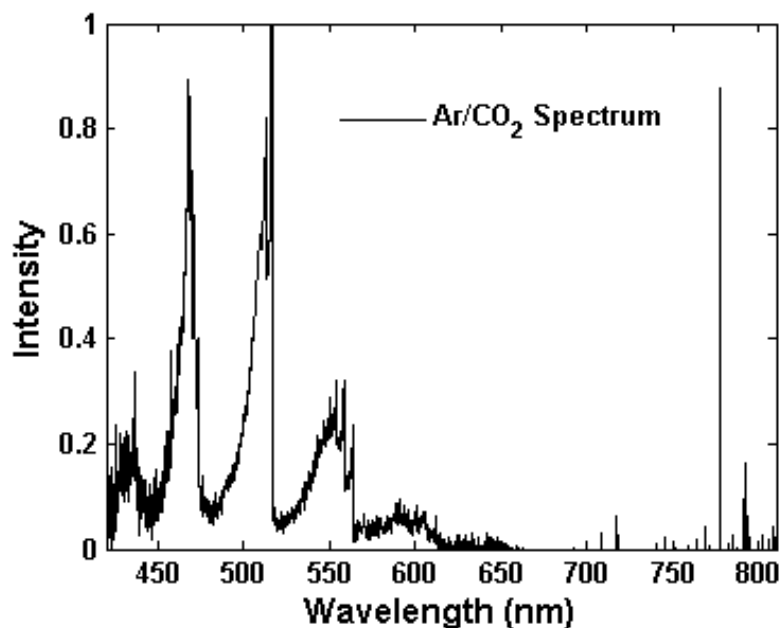


Figure 6.2: Normalized Ar/CO₂ emission spectra at 1 kw. Ar flow rate is 8 slm and CO₂ flow rate is 1 slm.

the addition of CO₂. The strong change in color demonstrates that Ar is no longer the primary excited species in the plasma, with the C₂ system having strong emission in the green visible spectrum.

6.1.2 Mass Spectrometry of the CO₂/Ar Plasma

Variations in the CO₂:Ar flow rate ratio were investigated to determine an optimal operating condition for efficient CO₂ dissociation. The flow rate ratio remained constant while microwave input power was varied from 1-2 kW. As CO₂ flow rate increased past 4 slm, the microwave forward power required to maintain a stable discharge was at least 1.5 kW. The three stub tuner waveguide used to match the plasma impedance to the magnetron kept reflected power below 10 W for all operating conditions.

As with the experimental MS results described in Chapter IV, care must be taken with data analysis to ensure the values reported at 28 amu/ q_e represent singly ionized

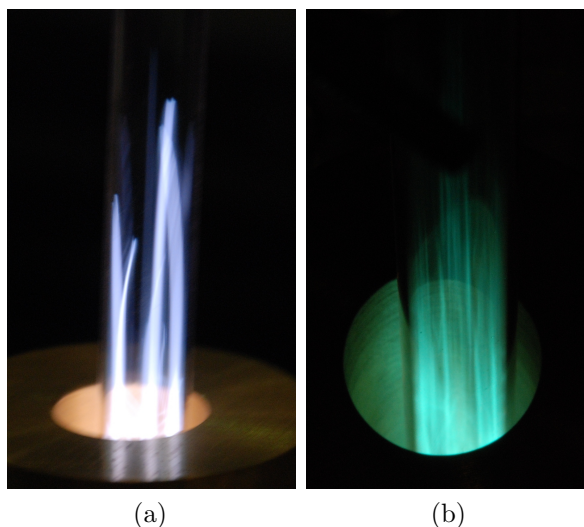


Figure 6.3: Pictures of plasma with 700 W input power: a) pure Ar discharge, b) Ar plasma with 1% CO₂ added.

CO and not N₂. To circumvent this problem, an initial background RGA scan is taken of the air to determine an initial gas composition. Then Ar flow is injected into the discharge tube and another background scan is recorded for the Ar-dominant environment. In this way, the Ar peak at mass/charge ratio 40 can be corrected for any initial Ar in the air, and the CO peak can be corrected for any nitrogen still remaining in the discharge tube after the injection of Ar. Thus any initial Ar found in the air scan will be subtracted from all subsequent Ar peaks, and any remaining peak at 28 amu/ q_e existing in the Ar background will be subtracted from all subsequent peaks at 28 amu/ q_e once CO₂ is added. The Ar background will serve to correct for any initial remaining oxygen and CO₂ in the system as well. This method provides assurance that any peaks for mass/charge ratios 16, 28, 32, and 44 properly correspond to O, CO, O₂, and CO₂ created in the plasma system.

Figure 6.4 shows an example of an untreated RGA spectrum for air and Ar. The dotted curve representing air shows a dominant peak at 28 for N₂ and another peak at 32 for O₂. There is also a small peak at 14 which can represent doubly ionized N₂ or atomic nitrogen. Once 8 slm of Ar is injected into the discharge tube, 40 becomes

the dominant peak corresponding to singly ionized Ar, with a smaller peak at 20 for doubly ionized Ar. The other peaks found in the air spectrum become insignificant. The RGA spectrum changes once more when CO₂ is added, as shown in Figure 6.5. This spectrum is the result of adding 4 slm of CO₂ to the existing 8 slm of Ar, with 1.5 kW of MW power applied. Given the high flow rate of Ar, 40 remains the highest peak in the spectrum, followed by CO₂ at 44. There are smaller peaks for singly ionized species at 12, 16, 28, and 32 for C, O, CO, and O₂, respectively. Doubly ionized Ar is also still present at 20.

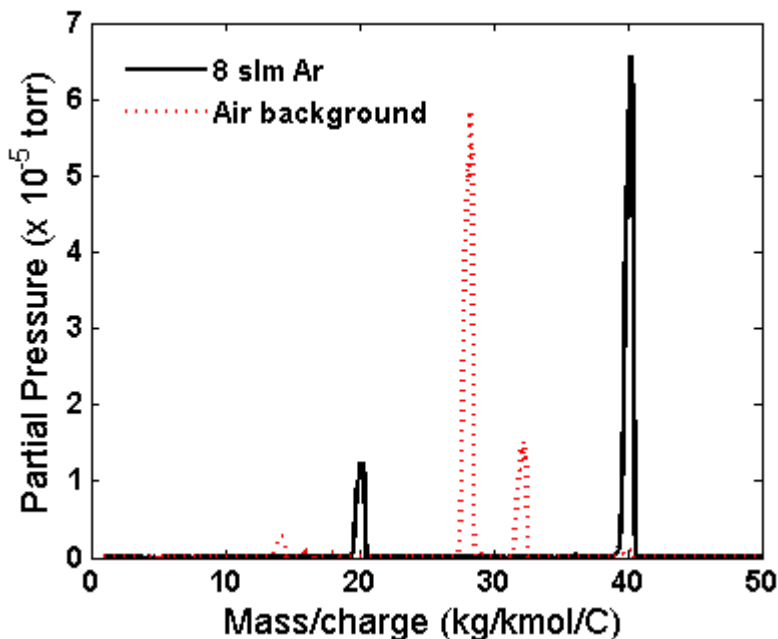


Figure 6.4: RGA background scans for air and Ar

6.1.2.1 Effects of Flow Rate and Power

As expected, increased MW input power leads to increased production of CO and O₂, demonstrated in Figure 6.6. Here the output flow rates of CO and O₂ as determined from MS data are plotted as a function of power for two different CO₂ input flow rates: 4 slm and 1 slm. For both species there is a steady increase in flow rate as power increases to 1.75 kW. There is also an increase in flow rate as the input

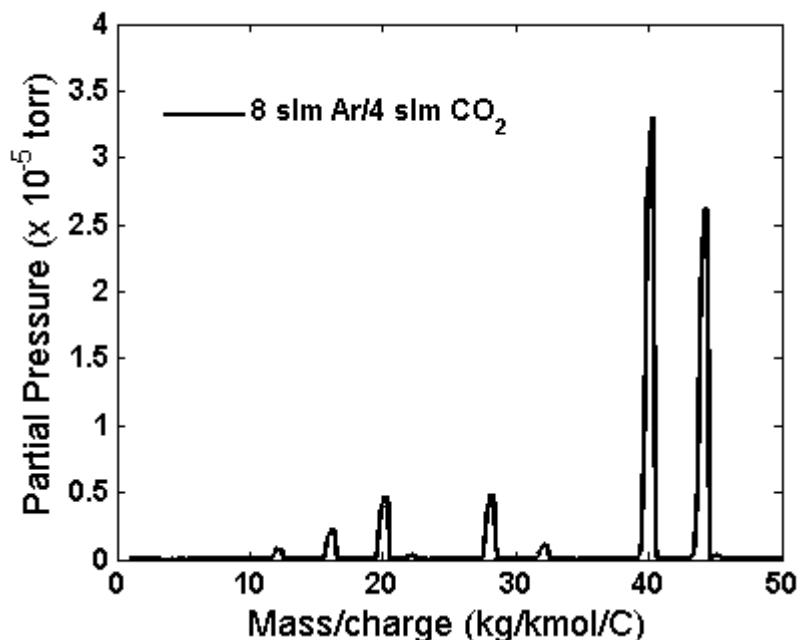


Figure 6.5: Ar/CO₂ RGA scan for 8 slm Ar and 4 slm CO₂

CO₂ increases. Each CO₂ flow rate operating condition is plotted for three different Ar flow rates: 6, 8, and 10 slm.

There is no well-defined correlation shown in these figures between Ar flow rate and CO₂ flow rate. For a more definite view, CO production as a function of Ar flow rate is plotted in Figure 6.7. Three different CO₂ input flow rates are shown for a MW power of 1.75 kW. For all three conditions, the production of CO remains relatively constant as the Ar flow is varied. Therefore, it will be taken that Ar flow rate has no effect on CO production in this experimental system. Ar is used for electron production in the plasma, and electron collisions provide the mechanisms for dissociation to occur. However at a constant MW power, electron density may not increase as Ar gas flow is increased. Therefore higher Ar flow rates will not affect the collisional processes benefiting dissociation, resulting in no net change in CO production.

Figure 6.6 already provides some evidence that CO₂ input flow rate has an effect on CO production. A clearer trend can be shown in Figure 6.8. Here CO production is plotted as a function of CO₂ flow rate ranging from 1-12 slm for constant MW power

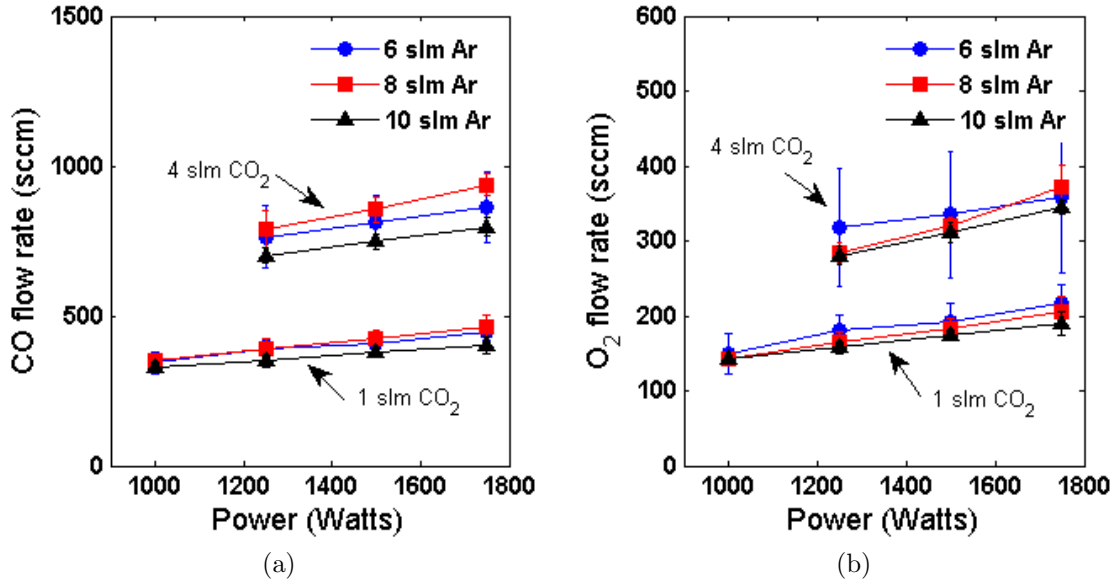


Figure 6.6: CO and O₂ production as a function of power. Two different CO₂ input flow rates, 1 and 4 slm, as well as three different Ar flow rates, 6, 8 and 10 slm, are displayed.

1.75 kW. As expected, CO flow rate increases almost linearly with CO₂ flow rate for both Ar flow rates. Thus for a given set power, there is a direct linear relationship between CO production and CO₂ input flow. This result is expected based on the equation for total CO₂ decomposition, $CO_2 \rightarrow CO + 1/2O_2$. If the conversion rate of CO₂ to CO was 100% for each operating condition presented in 6.8, the slope of this plot should equal unity.

6.1.2.2 Dissociation Efficiencies

Using species identification data from the RGA, the efficiencies of CO₂ dissociation can be evaluated following the methods presented in Section 4.3. From Equation 4.5, $\eta = \alpha \cdot (\Delta H/E_v)$, the energy efficiency of CO₂ conversion to CO can be calculated. Once again, α is the conversion efficiency defined by the ratio of CO output flow rate to CO₂ input flow rate, ΔH is the theoretical enthalpy of dissociation, and E_v is the specific energy input. Figure 6.9 shows the results of calculated energy efficiency for all operating conditions tested. CO₂ input flow rate ranges from 1-16 slm, power

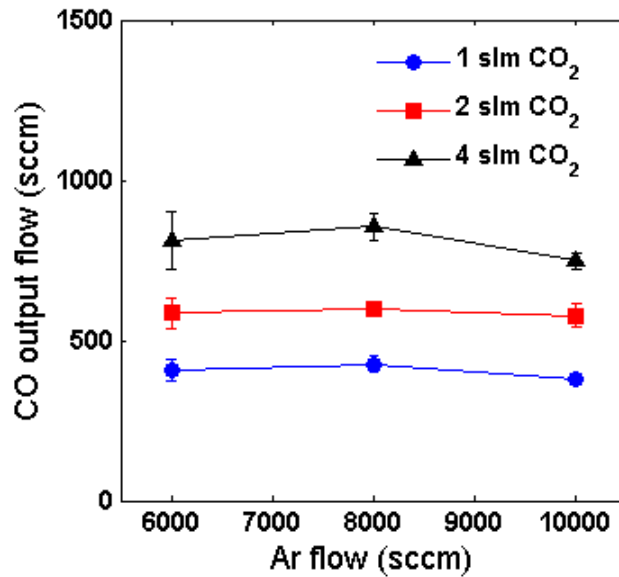


Figure 6.7: CO production as a function of Ar flow. Power is kept constant at 1.75 kW and three different CO₂ flow rates, 1, 2, and 4 slm, are displayed.

ranges from 1-2 kW, and Ar flow rate ranges from 6-10 slm.

Figure 6.9 shows an inverse relationship between energy efficiency and specific energy. This is consistent with the results presented in Section 4.3, and is derived from the simple expression of Equation 4.5. The highest value for energy efficiency is around 20%. This corresponds to the operating condition with the highest amount of CO₂ input flow rate, 16 slm, with 1.5 kW of MW power. Likewise, the lowest value of energy efficiency corresponds to the lowest CO₂ flow rate, 1 slm, at 1.75 kW. As discussed in Section 5.1, the ideal range for specific energy values to achieve energy efficient dissociation is around 0.3-1 eV/mol. However the lowest value of specific energy experimentally tested in the MW system is only 1.5 eV/mol, which gave the result for highest energy efficiency. Perhaps if higher CO₂ flow rates were tested at the same power level, energy efficiency would increase.

Similarly, the calculated conversion efficiency is shown in Figure 6.10. As with the results of Chapter IV, there is a trade-off between energy efficiency and conversion efficiency. Thus the highest conversion appears for the lower CO₂ flow rate of 1 slm

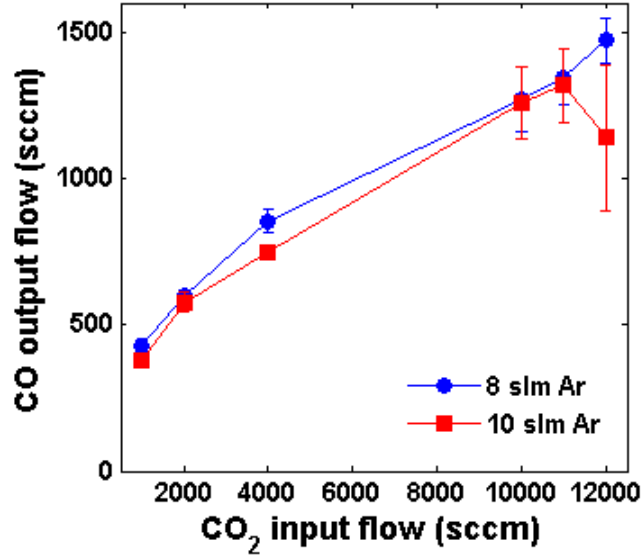


Figure 6.8: CO production as a function of CO₂ flow. Power remains constant at 1.75 kW, while CO₂ flow rate is varied from 1-12 slm for two different Ar flows of 8 and 10 slm.

reaching almost 50%, while the lower conversion corresponds to the highest CO₂ flow rate of 16 slm resulting in only 10%. It is no surprise that the highest conversion rate occurred for the highest value of specific energy tested, about 27 eV/mol. If higher values of specific energy were tested, no doubt conversion efficiency would continue to increase, possibly approaching 100%. However, the energy efficiency of such a case would be miniscule.

Energy efficiency of CO₂ conversion in this system is lower than expected, given the non-equilibrium and high electron density characteristics of atmospheric pressure surface wave discharges outlined in Section 5.1. For the lower value of $E_v = 1.5$ eV/mol tested here, experimental and computational results in other discharge systems reported efficiencies around 50% as previously shown in Figure 5.1, which is what was expected to be achieved in this system. Therefore the CO₂ plasma must behave differently than the noble gas plasmas created with Ar, Ne, and He, whose density and temperature measurements were reported in literature [67, 88]. Plasma temperature measurements gained from OES of the CO₂ discharge may provide some insight into this unexpected

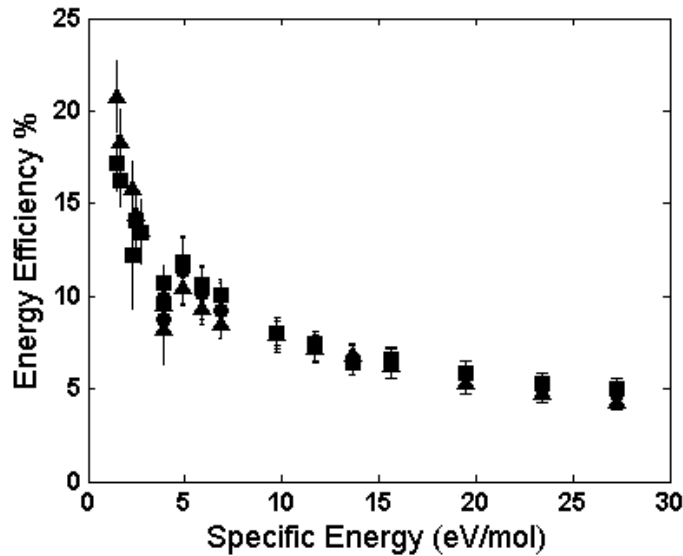


Figure 6.9: Energy efficiency of CO_2 dissociation. All operating conditions of CO_2 flow rate, 1-16 slm, are displayed for all three different Ar flow rates (6 slm = ●, 8 slm = ■, 10 slm = ▲) and the corresponding power levels from 1-2 kW.

behavior.

6.1.3 Optical Emission Spectroscopy of the CO_2/Ar Plasma

6.1.3.1 SPECAIR Temperature Evaluation

Plasma temperature evaluation by OES was limited to the C_2 Swan system, as already discussed in Section 5.4. Using the Ocean Optics HR4000, optical emission spectra were taken for each operating condition and compared to the simulated spectra generated by SPECAIR. While the translational temperature was assumed equivalent to the rotational temperature and did not affect the computed spectrum, the rotational, vibrational, and electronic temperatures all had significant effects on the Swan system.

Figure 6.11 shows the experimental emission spectrum for the operating condition 10 slm Ar, 1 slm CO_2 , and 1 kW of power. Species molar fractions for this operating condition are computed from MS data and inserted into SPECAIR for spectra computation. Accompanying the experimental spectrum are different results for the simulated spectrum assuming a constant electronic temperature and vibrational temperature

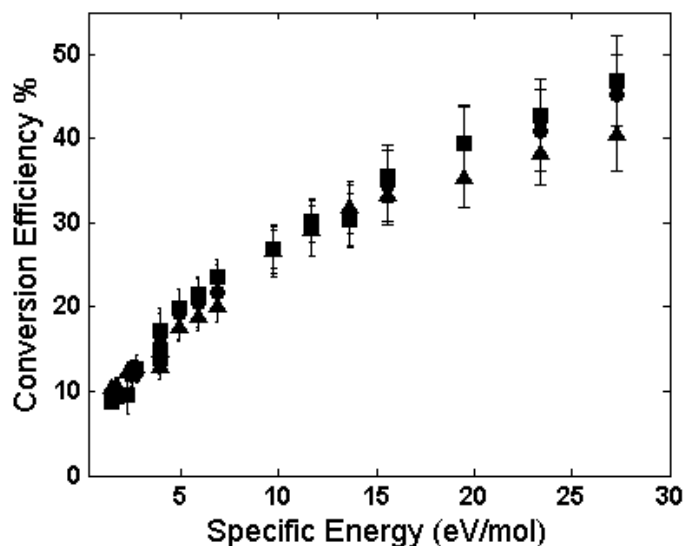


Figure 6.10: Conversion efficiency of CO_2 dissociation. All operating conditions of CO_2 flow rate, 1-16 slm, are displayed for all three different Ar flow rates (6 slm = ●, 8 slm = ■, 10 slm = ▲) and the corresponding power levels from 1-2 kW.

while varying the rotational temperature. When $T_r = 6050$ K, there is a good match between the experimental spectrum and the computed spectrum. However, when the temperature is increased to 9050 K, the band width increases and the peak intensities decrease. As T_r is reduced to 3050 K, the band width significantly narrows and the overall intensity drops, however the (0,0) band head at 516 nm remains around unity with the experimental peak.

A similar examination can be performed for the vibrational temperature. In this case, the rotational and electronic temperatures remain constant while T_v is varied. Figure 6.12 shows the computed spectrum variation for different values of vibrational temperature using the same operating conditions described for Figure 6.11. With T_r left constant at 6050 K and $T_{el} = 13900$ K, a value of $T_v = 7600$ K provides a close match to the experimental spectrum. When T_v is increased to 10600 K, the intensity of the (1,0) band head at 474 nm increases while the intensity for the (0,0) and (0,1) bands decrease. There is also an increase in band width for the (1,0) band and a decrease in width for the (0,0) band. A decrease in T_v to 4600 K leads to a large

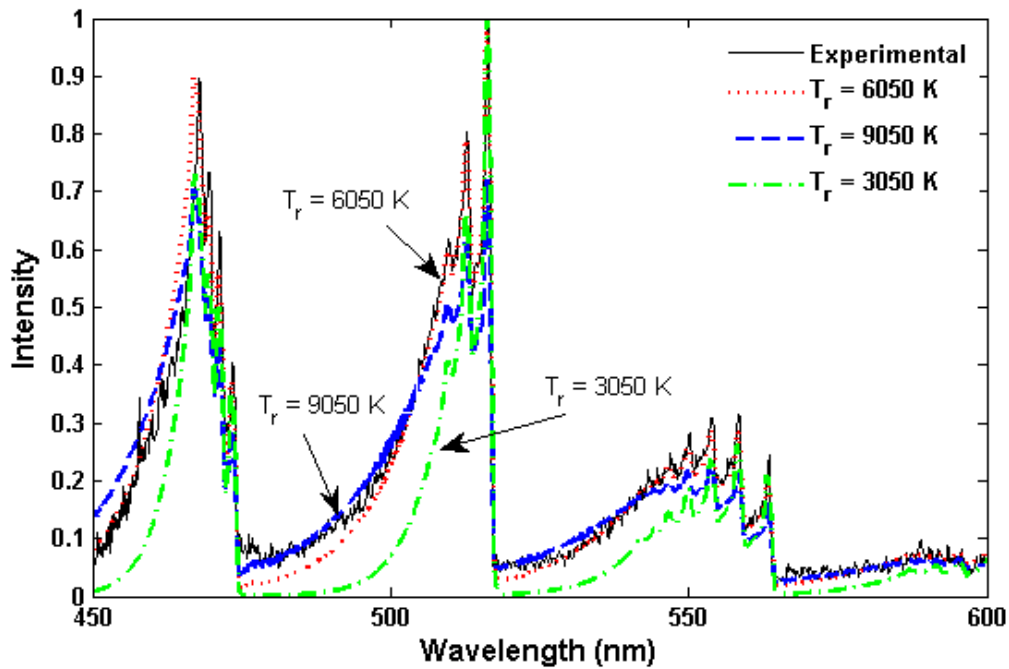


Figure 6.11: Effects of T_r on SPECAIR spectrum. Simulated for experimental condition Ar:CO₂ = 10:1 at 1 kW with constant $T_v = 7600$ K and $T_{el} = 13900$ K.

decrease in the intensity of the (1,0) band and decreases for the other two bands as well. Additionally, all three bands experience a narrowing of band width.

Unlike vibrational and rotational temperature, the electronic temperature has the most influence over the intensity of atomic oxygen emission lines, particularly the 777 nm line relevant for this experimental spectrum. Figure 6.13 illustrates the changes electronic temperature will have on the simulated spectrum. With constant $T_v = 7600$ K and $T_r = 6050$ K, the electronic temperature of 13900 K provided the best match to the experimental spectrum. A decrease in temperature to 10900 K results in a drastic reduction in emission intensity for the 777-nm line, but does not significantly affect the Swan system. When the temperature increases to 16900 K, the emission intensity exceeds that of the experimental 777 nm line, and also causes a large drop in intensity and band width for the entire Swan system.

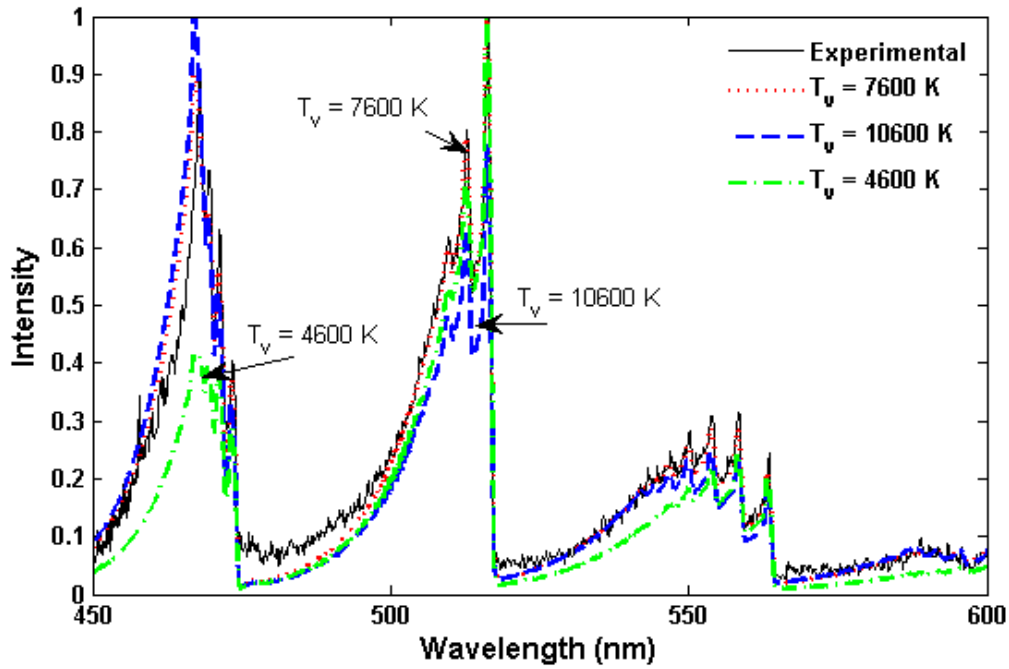


Figure 6.12: Effects of T_v on SPECAIR spectrum. Simulated for experimental condition Ar:CO₂ = 10:1 at 1 kW with constant $T_r = 6050$ K and $T_{el} = 13900$ K.

6.1.3.2 Plasma Temperatures

Through an understanding of how each temperature can affect the computed spectrum, an ideal match for all three temperatures with the experimental spectrum can be found. The results for plasma temperatures generated from SPECAIR simulations are shown in Figure 6.14. The results represent CO₂ flow rates from 1-8 slm with 10 slm Ar for power levels 1-2 kW. Given the MS results presented in the previous section, it is assumed that the C₂ emission spectra is not influenced by Ar flow rate. Unlike efficiencies, the temperatures seem independent of specific energy as well. The results show thermal non-equilibrium between the electronic temperature and the vibrational and rotational temperatures, $T_{el} \gg T_v \approx T_r$. The electronic temperature remains steady around 1.2 eV (14,000 K), which is near the expected value for electron temperature of 1 eV based on the reported results discussed in Section 5.1. However the rotational temperature is in thermal equilibrium with the vibrational temperature

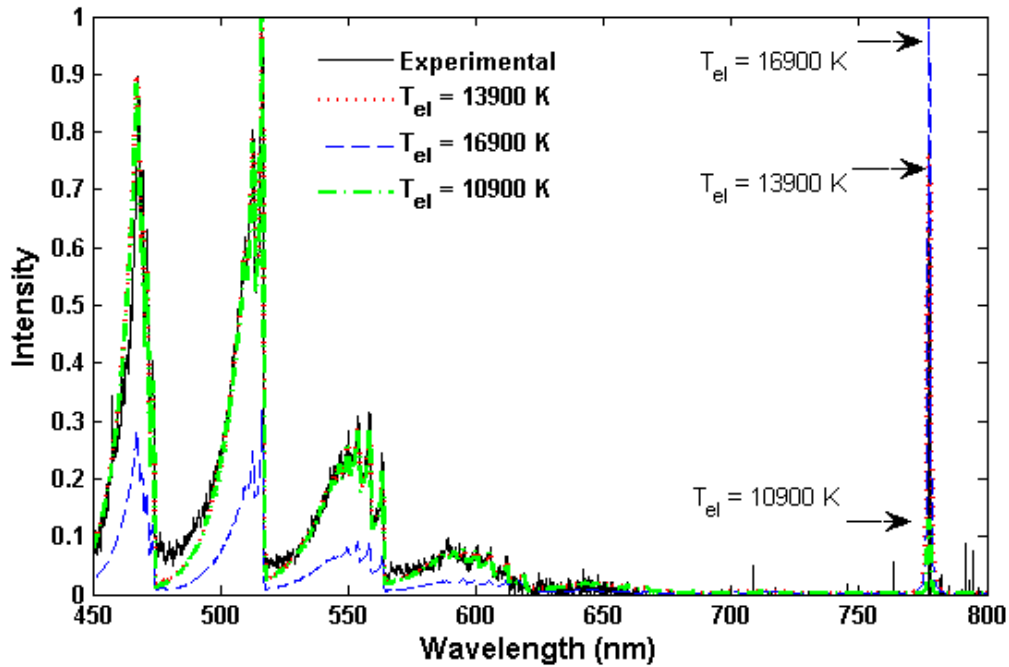


Figure 6.13: Effects of T_{el} on SPECAIR spectrum. Simulated for experimental condition Ar:CO₂ = 10:1 at 1 kW with constant $T_r = 6050$ K and $T_v = 7600$ K.

at 6000 K, significantly higher than the reported values near 300 K (Figure 5.3).

The C₂ Swan system has been used in several systems to evaluate the temperature of a gas [2,64,75,80]. A similar system using a microwave plasma torch at atmospheric pressure evaluated vibrational and rotational temperatures using the Swan system for CO₂ and CO₂-N₂ plasmas [2]. The results indicated thermal equilibrium between T_r and T_v , with temperatures around 6500 K for the pure CO₂ system and around 5500 K for the CO₂(97%)-N₂(3%) discharge. Another study reported temperature values for a pulsed laser irradiation plasma plume on a graphite target [89]. The resulting C₂ emission spectrum indicated rotational temperatures in the range of 5000-6000 K. These temperature values are all in agreement with the experimental temperatures plotted in Figure 6.14 of $T_r \approx 6000$ K.

However there is still some uncertainty as to whether the C₂ system is an adequate indicator of the gas temperature. Emission spectra from the 2nd positive system of N₂ (C³Π_u - B³Π_g) is typically used for gas temperature measurement in air and

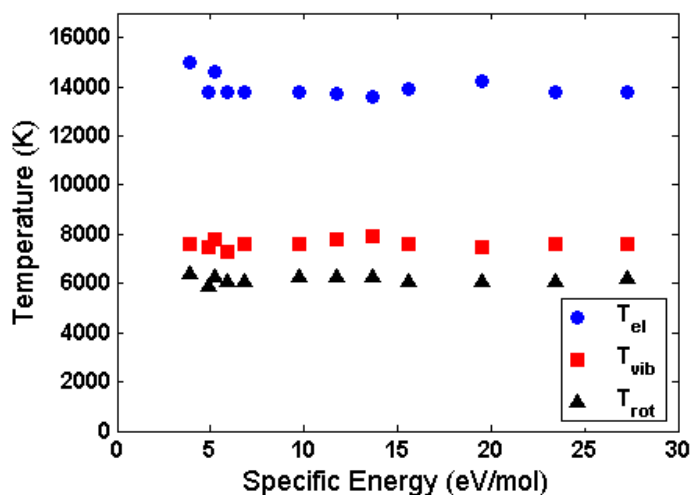


Figure 6.14: Plasma temperature results from SPECAIR simulations. Results presented for CO₂ flow rates 1-8 slm, Ar flow rate 10 slm, and power from 1-2 kW.

nitrogen discharges [63]. Other radiative excited species like C₂, OH, or CN can cause a tendency to overestimate the temperature because these species result from chemical reactions, and thus the residual chemical energy can increase the measured temperature [63,111]. Also, given that the molar fraction of C₂ is less than 1% in the experimental discharge presented here, the rotational temperature may not accurately describe the entire bulk gas temperature.

However, others have tested how well the C₂ gas temperature matches the temperature obtained using the N₂ 2nd positive system. These experiments were performed in a moderate pressure (0.5-10 torr) inductively coupled plasma source with a background gas mixture of C₂F₆, O₂, N₂, and Ar [3]. Rotational temperature measurements obtained from N₂ and C₂ emission in the same plasma were found to agree reasonably well, 5270 K and 5500 K respectively [3]. The vibrational temperature determined from the C₂ $\Delta v = 0$ band was 8700 K, which is close to the $T_v = 8000$ K reported in this work. Thus in some discharge systems, C₂ emission may be an accurate thermometer for gas temperature.

An estimate of the gas temperature can be calculated using thermodynamic

principles to determine if the experimentally measured gas temperature resides in the expected range. Equation 6.1 gives the relation between input power and specific enthalpy, assuming constant pressure:

$$P = \dot{m}\Delta h = \dot{m}c_p\Delta T_g \quad (6.1)$$

where P is power, \dot{m} is mass flow rate of the Ar/CO₂ gas mixture, and h is specific enthalpy, which equals the multiplication of the specific heat capacity (c_p) by the change in gas temperature (ΔT_g). The specific heat capacity can be calculated using Equation 6.2:

$$c_p = \left(\frac{\gamma}{\gamma - 1} \right) \cdot \frac{R_u}{M} \quad (6.2)$$

where $\gamma = c_p/c_v$ (c_v is the specific heat capacity assuming constant volume) and M is the molecular weight of the gas species [84]. An average specific heat capacity for the Ar/CO₂ gas mixture can be calculated using the following formula:

$$\langle c_p \rangle = \frac{\dot{m}_{Ar}c_{pAr} + \dot{m}_{CO_2}c_{pCO_2}}{\dot{m}_{Ar} + \dot{m}_{CO_2}}. \quad (6.3)$$

Using Equations 6.1-6.3, an estimated change in temperature can be calculated for a given input power and Ar/CO₂ flow rate mixture. For a power range of 1-2 kW and CO₂ flow rate range of 1-8 slm with Ar flow rate constant at 8 slm, the estimated change in gas temperature ranges from 2200 - 13100 K. Given this gas temperature estimation, it is plausible that the experimentally measured gas temperature is accurate near 6500 K.

Though the temperature results shown in Figure 6.14 indicate weak thermal non-equilibrium between T_{el} and T_r , the local thermodynamic equilibrium between T_r and T_v can provide some explanation for the lower-than-expected efficiencies of CO₂ conversion shown in Figure 6.9. As described in Section 3.2, vibrational excitation

of CO₂ provides the most effective pathway for dissociation. However not only must vibrational excitation be stimulated, but the population of vibrationally excited species must also be maintained. In order to maintain this population, there must be thermal non-equilibrium between translational and vibrational temperatures. Under these conditions the vibrational-translational (VT) relaxation rate coefficient is relatively slow compared to vibrational excitation. The VT relaxation rate coefficient can be approximated by Equation 6.4, assuming relaxation is primarily related to the symmetric vibrational modes [37]:

$$k_{VT} \approx 10^{-10} \cdot \exp(-72/T_g^{1/3}) \text{ cm}^3/\text{s}. \quad (6.4)$$

When the gas temperature is close to room temperature in thermal non-equilibrium with T_v , $k_{VT} \approx 2 \times 10^{-14} \text{ cm}^3/\text{s}$. Using the gas temperature measured from the C₂ spectra of 6000 K, the rate coefficient increases two orders of magnitude to $k_{VT} \approx 2 \times 10^{-12} \text{ cm}^3/\text{s}$.

In addition to the influence of gas temperature on VT relaxation rates that affect dissociation, higher gas temperatures also leave the dissociation products unprotected against reverse reactions. High gas temperature leads to the oxidation reaction of CO, $CO + O_2 \rightarrow CO_2 + O$. The reaction rate coefficient for CO oxidation can be computed as a function of gas temperature using the Arrhenius rate equation cited previously in Equation 5.19. Tabulated values of the empirical values A and E_a relevant to CO₂ reactions can be found in Appendix C. When the CO oxidation occurs at room temperature, the reaction rate coefficient is insignificant, $k = 5 \times 10^{-31} \text{ cm}^3/\text{s}$. However when the rate coefficient is calculated for $T_g = 6000 \text{ K}$, the rate becomes much more important as a reaction mechanism for CO₂ generation: $k = 1 \times 10^{-13} \text{ cm}^3/\text{s}$. In order to prevent this reverse reaction from occurring in high temperature discharges, substantial quenching on the order of $10^8 - 10^9 \text{ K/s}$ must be used. Thus the result of

high gas temperature in the experimental system provides some explanation for the lower energy efficiency values.

6.2 Plasma/Catalyst Results

6.2.1 Control Test with Uncoated Monolith

Before the effects of catalyst material on CO₂ dissociation can be examined, a control test using an uncoated ceramic monolith must be performed. Therefore any subsequent changes to efficiency can be accurately attributed to the Rh catalyst. In these experiments, operating conditions were repeated from the plasma-only system to include CO₂ flow rates from 1-8 slm, Ar flow rates 8 and 10 slm, and power from 1-2 kW. Based on the previous results, it is assumed that variation in Ar flow rate has no significant affect on CO₂ conversion. For all experiments performed, the uncoated monolith is placed approximately 25 cm downstream of the center of the discharge tube. For every change in CO₂ flow rate, the previously-inserted monolith is replaced by an unused monolith.

6.2.1.1 Plasma/Monolith Efficiencies

Energy efficiency for the plasma/monolith system is presented in Figure 6.15. The curve follows a similar trend as displayed in Figure 6.9, with energy efficiency increasing as specific energy decreases. Since CO₂ flow rate was tested only up to 8 slm in this system, the highest energy efficiency achieved with the monolith should be lower than the $\eta = 20\%$ achieved for 16 slm CO₂ in the pure plasma system. However, for 8 slm CO₂ in the pure plasma system $\eta = 12\%$, while for the plasma/monolith system $\eta = 10\%$. Similarly at high values of E_v , $\eta = 5\%$ in the pure plasma system, and $\eta = 4\%$ in the plasma/monolith system. Hence there is a small decrease in overall energy efficiency observed for the plasma/monolith system.

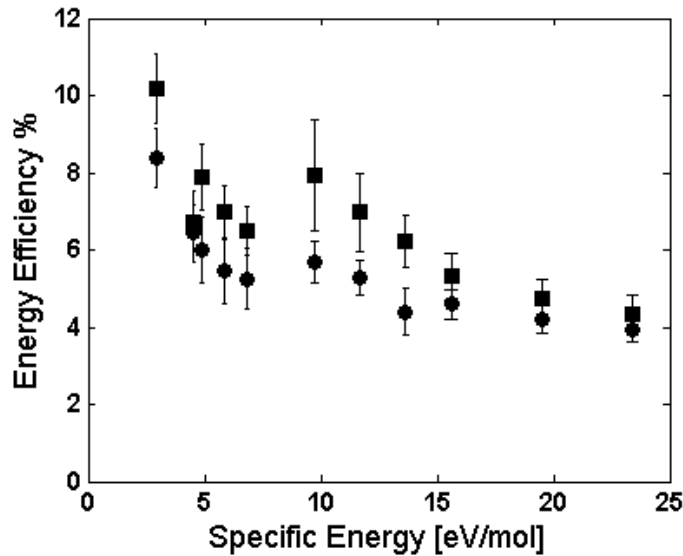


Figure 6.15: Energy efficiency of CO_2 dissociation with uncoated monolith. All operating conditions of CO_2 flow rate, 1-8 slm, are displayed for two different Ar flow rates (8 slm = ●, 10 slm = ■) and the corresponding power levels from 1-2 kW.

Conversion efficiency is displayed in Figure 6.16. The same small decrease in conversion efficiency is observed here when compared to the pure plasma system. The highest conversion rate for 1 slm CO_2 at 1.5 kW of power is near 35%, while the same operating condition in the pure plasma system reaches about 45%. The lowest conversion rate for 8 slm CO_2 is about 10%, while at the same CO_2 flow rate in the pure plasma system $\alpha = 15\%$. These results conclude that the presence of the ceramic monolith has a small but obvious effect on CO_2 conversion. An examination of the optical emission spectrum may provide some insight into this phenomena.

6.2.1.2 Plasma/Monolith Temperatures

In a similar method described in Section 6.1, the emission spectrum of the C_2 Swan system is evaluated to determine plasma temperature measurements. Figure 6.17 shows the temperature results from matching simulated SPECAIR spectra to experimental spectra. While the vibrational temperature appears to remain unchanged at 8000 K, the electronic and rotational temperatures have experienced some changes in

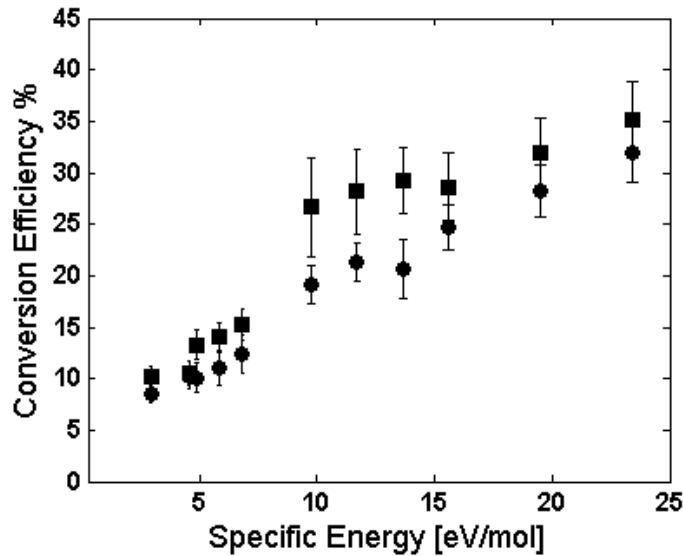


Figure 6.16: Conversion efficiency of CO₂ dissociation with uncoated monolith. All operating conditions of CO₂ flow rate, 1-8 slm, are displayed for two different Ar flow rates (8 slm = ●, 10 slm = ■) and the corresponding power levels from 1-2 kW.

comparison with the pure plasma system shown in Figure 6.14. Here the electronic temperature is between 11,000-12,000 K (~ 1 eV), whereas in the pure plasma system $T_{el} = 14,000 - 15,000$ K. The rotational temperature is about 500 K higher (greater than the ± 100 K error in matching the simulated spectra to the experimental spectra) than the pure plasma system, reaching 6500 K. From these results it appears that the plasma has moved closer to reaching equilibrium between T_{el} and T_r . Consequently, T_r is also closer in equilibrium to the vibrational temperature. As already discussed, systems described by $T_v \approx T_r$ result in lower energy efficiency, which can explain the slight drop in efficiency with the presence of the uncoated monolith.

6.2.2 Rh/TiO₂ Catalyst Test

A monolith coated with Rh/TiO₂ was inserted into the discharge at the same location as the uncoated monolith. All operating conditions for CO₂ and Ar flow rates are identical to the conditions tested with the uncoated monolith, with only a few slight variations in MW power for 6 and 8 slm CO₂. Similarly, a new catalyst-coated

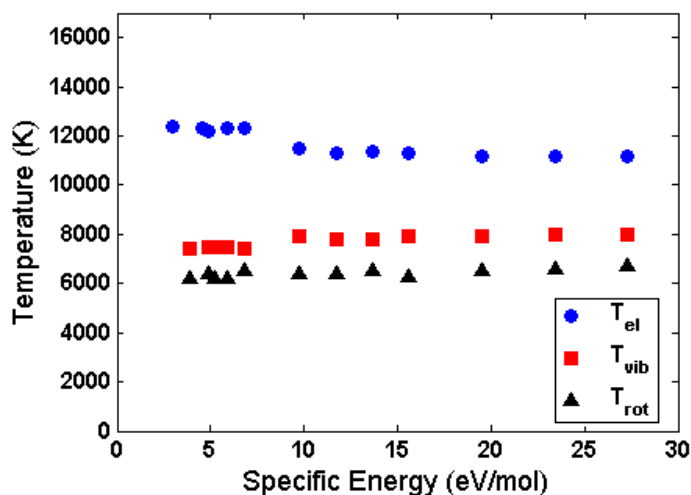


Figure 6.17: Plasma/monolith temperature results from SPECAIR simulations. Results presented for CO₂ flow rates 1-8 slm, Ar flow rate 10 slm, and power from 1-2 kW.

monolith is inserted into the discharge tube for every operating condition with a change in CO₂ flow rate. Again it is assumed that Ar flow rate has no effect on CO₂ conversion.

6.2.2.1 Plasma/Catalyst Efficiencies

The results for energy efficiency in the plasma/catalyst system are shown in Figure 6.18. The same trend of $\eta \propto 1/E_v$ is evident in the results. However the energy efficiency experiences an even larger drop with the addition of Rh catalyst. Here $\eta_{max} = 6\%$, half the energy efficiency for the same operating condition in the pure plasma system, and lower still than the plasma/monolith system. Likewise, the lowest value of η reaches about 2-2.5%, unlike the pure plasma system with $\eta = 5\%$.

Figure 6.19 displays results for conversion efficiency. As expected based on the energy efficiency results, the conversion efficiency is lower than the pure plasma system. Maximum conversion reaches 20% while the pure plasma system reached about 45% for the same operating condition. For the lowest value of specific energy tested at 8 slm CO₂, the conversion rate drops to 8%, which is about half the value achieved in

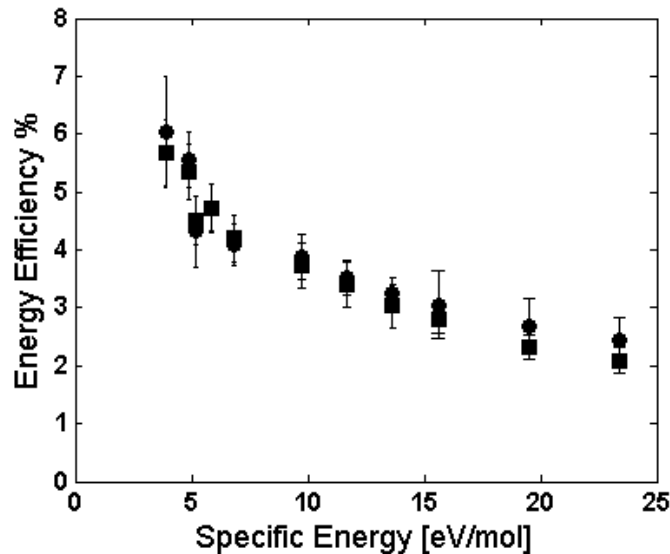


Figure 6.18: Energy efficiency of CO₂ dissociation in the plasma/catalyst system. All operating conditions of CO₂ flow rate, 1-8 slm, are displayed for two different Ar flow rates (8 slm = ● , 10 slm = ■) and the corresponding power levels from 1-2 kW.

the pure plasma system. Unfortunately the Rh/TiO₂ catalyst material had a negative effect on the CO₂ conversion process to CO.

6.2.2.2 Plasma/Catalyst Temperatures

Perhaps analysis of the optical emission spectra can provide some insight into how the plasma properties are affected by the presence of the catalyst material. Figure 6.20 gives results for the plasma temperature measurements taken from analysis of the C₂ system. The electronic temperature remains almost constant for all operating conditions at 12,000 K (~ 1 eV). Similarly, vibrational temperature remains right around 7700 K until low values of specific energy are reached where T_v increases to 8000 K. Rotational temperatures are also constant around 6500 K until increasing to almost 7000 K at low specific energy values. The temperature results are not significantly different from the plasma/monolith system shown in Figure 6.17, indicating there must be another influence causing lower efficiencies in this system.

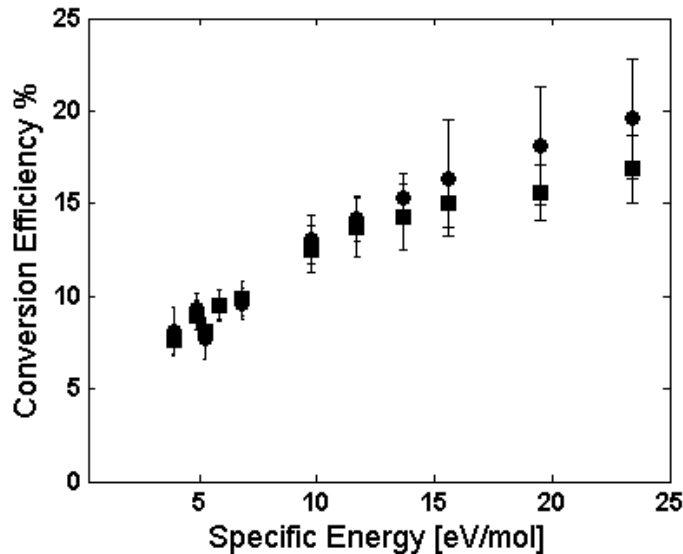


Figure 6.19: Conversion efficiency of CO_2 dissociation in the plasma/catalyst system. All operating conditions of CO_2 flow rate, 1-8 slm, are displayed for two different Ar flow rates (8 slm = ●, 10 slm = ■) and the corresponding power levels from 1-2 kW.

6.3 Computational Results

The microwave plasma was simulated using the GlobalKin model described in Section 5.5. The primary simulations were chosen to duplicate the experimental operating conditions, using identical Ar/ CO_2 flow rate ratios and MW power levels. Two additional CO_2 flow rates of 0.5 slm and 1.5 slm were also simulated to demonstrate a more complete data set for the calculated efficiency curves. Additionally, a variety of Ar flow rates and operating pressures outside of the experimental testing conditions were simulated to determine the theoretical effects of such operating conditions on the conversion efficiency of CO_2 to CO.

6.3.1 Simulated Efficiencies

Figure 6.21 compares simulated conversion efficiencies to experimental results. The efficiencies are calculated using the computed final gas density of CO at the end of the discharge tube. Using conservation of mass, the density of CO can be converted to

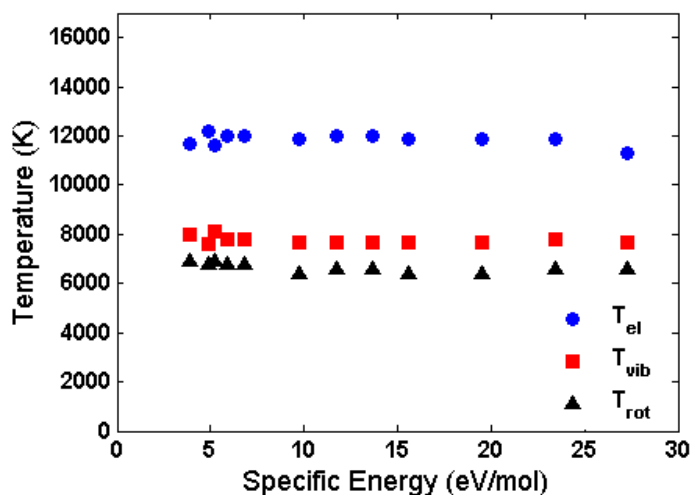


Figure 6.20: Plasma/catalyst temperature results from SPECAIR simulations. Results presented for CO₂ flow rates 1-8 slm, Ar flow rate 10 slm, and power from 1-2 kW.

flow rate. Then using Equation 4.4 and taking the ratio of final CO flow rate to the input CO₂ flow rate, the conversion efficiency is calculated. While the overall trend for simulated conversion efficiency follows the experimental results, the simulated curve is shifted towards lower efficiencies. Additional simulated operating conditions are shown at higher values of E_v (a lower CO₂ flow rate), that were not experimentally tested. At these higher values of E_v for CO₂ input flow of 0.5 slm, the simulated curve appears to align more closely with an extrapolation to the experimental curve for conversion efficiency. However, at low specific energy values the computational results drop nearly to zero, deviating greatly from the experimental curve.

The conversion efficiency results translate directly to the energy efficiency results of Figure 6.22, via Equation 4.5. The disparity between computational and experimental energy efficiency results is very large for low values of E_v . Similarly, at high values of E_v , the model falls almost directly in line with an extrapolation to the experimental curve. These results clearly demonstrate that another mechanism, unaccounted for in the model, is responsible for CO production in the experimental system, especially at high flow rates of CO₂.

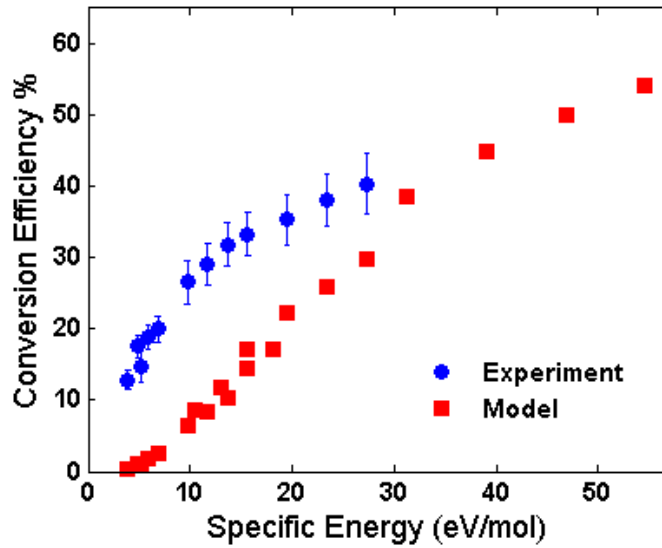


Figure 6.21: Computational conversion efficiencies for Ar flow rate of 10 slm, CO₂ flow rate from 1-8 slm , and 1-2 kW of power.

6.3.2 Simulated Plasma Properties

Through Equations 5.15 and 5.16, GlobalKin can compute the electron temperature and gas temperature in the simulated plasma. Since the model is run in plug flow mode, species densities and plasma temperatures are given as a function of axial position along the discharge tube. For accurate comparison with the optical emission temperature results of the experimental system, the simulated temperature and electron density values are taken at the center of the discharge tube, close to the position of the light-collecting collimating lens. In this location the experimental plasma was its brightest and hottest, and where most of the plasma-chemical reactions took place.

The results for T_e are shown in Figure 6.23. The simulated plasma electron temperature increases monotonically with specific energy, while the experimentally measured temperature is unaffected by E_v . The computational results imply that as the molar fraction of CO₂ increases at low E_v , the electron energy decreases as it is transferred to heavy particles via collisions. However, the electrons maintain more energy in the simulated plasma than in the experimental plasma, since T_e is nearly

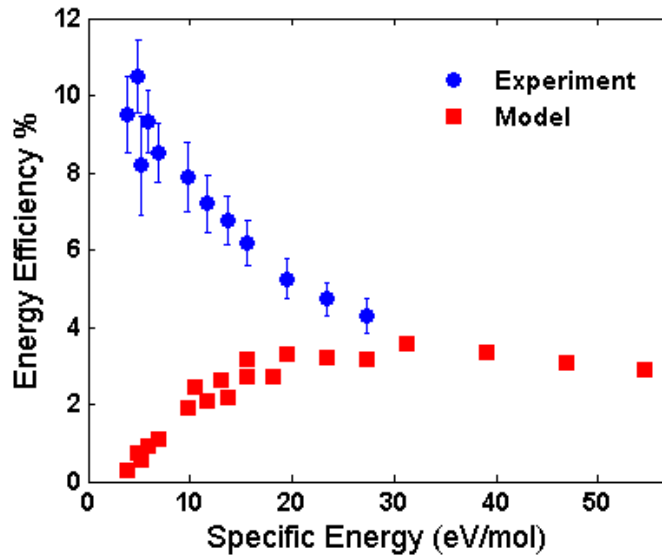


Figure 6.22: Computational energy efficiencies for Ar flow rate of 10 slm, CO₂ flow rate from 1-8 slm , and 1-2 kW of power.

twice as large in the simulation as in the experimental results.

While electron temperatures for experimental and computational results are close (ranging between 1-2 eV), the experimentally measured gas temperature is significantly higher than the computed gas temperature. The simulated gas temperature remains almost constant around 1000 K, presenting characteristics of a clear non-thermal discharge, as indicated by the results of Figures 6.23 and 6.24. The experimentally observed plasma temperatures would indicate a tendency towards thermal equilibrium, though. The simulated gas temperature is unbelievably low, given that the plasma was causing the quartz discharge tube to melt which occurs around 2000 K. However these results may support the argument that the C₂ emission spectra is over estimating the gas temperature due to chemiluminescence, since carbon is created as a result of a chemical process. Chemiluminescence can result in an exaggerated emission intensity because of residual heat emitted from chemical reactions to produce C₂, causing an overestimation of temperature.

Equation 5.16 (which describes the differential equation for computing T_g), shows that the main contribution to gas heating is from elastic and inelastic collisions.

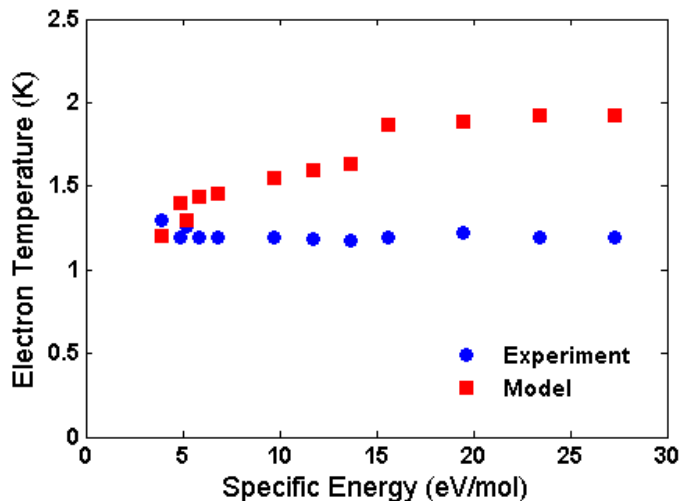


Figure 6.23: Computational electron temperature.

Similarly Equation 5.15 (describing T_e), shows that collisions are the main loss process. Given that the simulated T_e is higher and the simulated T_g is lower than the experimental results, it is likely that some important collisional processes have been excluded from the model which could affect the plasma temperatures. The simulated temperatures indicate that not as much collisional energy is being transferred from electrons to heavy particles.

The simulated plasma electron density is plotted in Figure 6.25. There is a trend of decreasing electron density with decreasing E_v that mimics the electron temperature trend. It is expected that for a given power level, lower CO_2 flow rates (higher E_v) result in more energy available per molecule, which can stimulate more dissociation and ionization events. Unfortunately there are no experimental results of electron density for comparison, though the simulated n_e can be compared to other reported experimental systems. In the systems summarized by Figure 5.3b, the electron density was experimentally determined to be in the range of $1 - 9 \times 10^{14} \text{ cm}^{-3}$ for atomic gases He, Ar, and Ne. Other reports of pure Ar discharges at atmospheric pressure has shown n_e reach 10^{15} cm^{-3} [51, 73]. However for an $\text{N}_2 + 1.6\% \text{ H}_2$ discharge operating at atmospheric pressure, the electron density drops to around $8 \times 10^{12} \text{ cm}^{-3}$ [36]. Thus

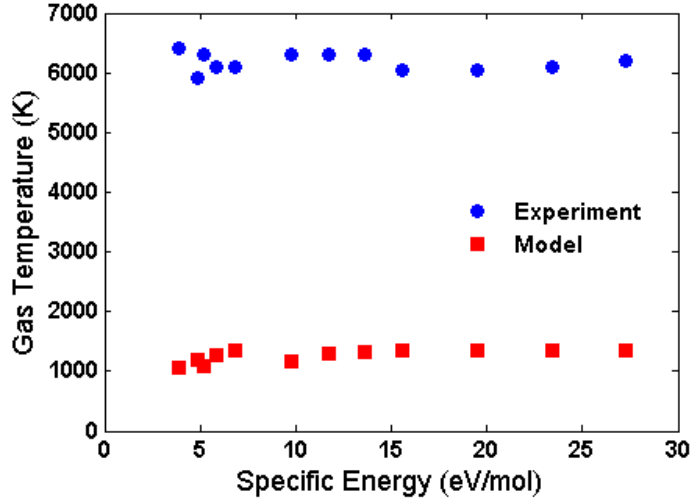


Figure 6.24: Computational gas temperature.

for molecular gas discharges, the electron density is lower. This agrees with the earlier observation that CO_2 is difficult to ionize, requiring the presence of Ar (or another noble gas) as an electron source.

An estimation of the electron density can be calculated using the Saha-Boltzmann Equation for atomic ionization to verify the computational results. This calculation assumes that the plasma temperatures are in local thermodynamic equilibrium, i.e., $T_e = T_g = T$. Equation 6.5 describes how electron density is related to gas temperature and atomic emission lines [39, 103]:

$$n_e = \frac{I'_i}{I'_{i+1}} 6.04 \times 10^{21} (T)^{3/2} \exp \left[\frac{(-E_k^{i+1} + E_k^i - \chi)}{k_B T} \right] \left[\frac{1}{\text{cm}^3} \right] \quad (6.5)$$

with

$$I'_i = \frac{I \lambda_{lk}}{A_{lk} g_k}. \quad (6.6)$$

Here, the index $i = 1$ denotes emission from neutral atoms while $i = 2$ represents singly ionized atoms, etc. The value λ_{lk} is the wavelength of the transition from state $l \rightarrow k$, I is the relative intensity of the emission line, χ is the ionization energy for the lowest ionic state, and E_k , A_{lk} , and g_k are constants related to the atomic transition,

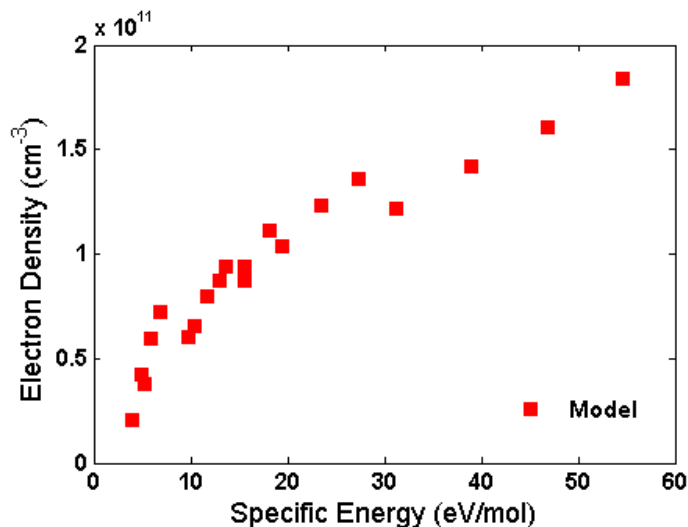


Figure 6.25: Computational electron density.

whose values can be found in the NIST Atomic Spectra Database [112].

Since atomic transitions are required for Equation 6.5, a pure Ar emission spectrum at 1 kW will be utilized for the calculation. The Ar neutral emission line at 706.72 nm and the singly ionized Ar emission line at 686.12 nm are used. Using the experimentally measured gas temperature $T = T_g = 6000 - 6500$ K, the electron density is calculated to be $2 \times 10^{10} - 7 \times 10^{11} \text{ cm}^{-3}$. If values of $T < 6000$ K are used, the electron density drops considerably to below 10^8 cm^{-3} . Thus, this estimation for n_e aligns well with the simulated electron density values, and supports the results for experimentally measured T_g .

6.3.3 Flow Rate and Pressure Effects

The effects of Ar flow rate and operating pressure were simulated in GlobalKin for conditions outside of the capabilities of the experimental system. Figure 6.26a shows the conversion efficiency of CO_2 to CO as a function of Ar flow rate for two different constant CO_2 input flow rates. The Ar flow rate was computationally varied from 1-12 slm, MW power was kept constant at 1.75 kW, and operating pressure was set to 760 torr (1 atm). There is a clear trend that higher Ar flow rate leads to higher

conversion efficiency, in contrast to the experimental results that showed no effect of Ar flow rate on dissociation. This Ar flow rate trend is most likely an artifact of the simulation's method for calculating initial species density. The user defines a total gas flow rate and the initial molar fractions of each gas species. The program also assumes a constant pressure throughout the simulation. Thus at constant CO_2 gas flow rate, an increase in Ar flow rate decreases the CO_2 molar fraction and effectively the density. At constant power, this results in the equivalent effect of decreasing CO_2 flow rate into the system. As already shown in the experimental results, a decrease in CO_2 flow rate increases conversion efficiency as the energy distribution increases per molecule. These computational results may suggest that total pressure does not remain constant in the discharge tube.

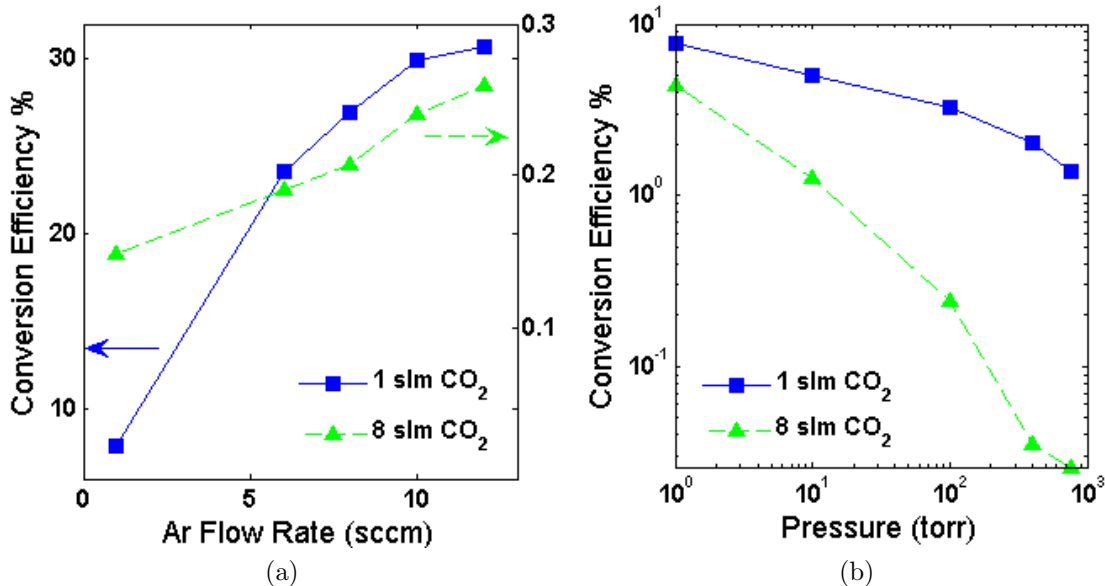


Figure 6.26: Computational results for operating conditions outside the experimental test plan: a) CO_2 conversion as a function of Ar flow rate with constant power of 1.75 kW and constant pressure of 760 torr, b) CO_2 conversion as a function of pressure with constant power of 1 kW and constant Ar flow rate of 10 sccm.

Figure 6.26b demonstrates the effects of pressure on the simulated conversion efficiency. The pressure is varied from 760 torr to 1 torr at constant MW power of 1 kW and constant Ar flow rate of 10 sccm. For both constant input flow rates

of CO₂, the conversion efficiency increases as operating pressure decreases. This trend is expected based on the high energy efficiencies of CO₂ dissociation reported for low pressure microwave discharges. The collision frequency necessarily decreases with pressure, and with less collisions there is less energy transfer between electrons and heavy particles. Hence, the discharge moves to further non-equilibrium at lower pressure which results in more efficient CO₂ dissociation and a greater conversion degree. As already discussed in Section 3.2 non-equilibrium discharges are uniquely effective at stimulating the vibrational modes of CO₂, resulting in efficient dissociation processes.

6.4 Discussion

6.4.1 Experimental Results

The follow section will provide a summary of the MS results for all three tests of the plasma alone, the plasma/monolith, and the plasma/catalyst systems. There will also be a more detailed look at the temperature results for each case. First a summary of energy efficiency, η , and conversion efficiency, α , is given in Figure 6.27. A clear decreasing trend in both η and α is evident when the uncoated-monolith is inserted and more so once the catalyst is used. The plasma temperature results can provide some explanation to this phenomenon, with temperature changes for each experiment more clearly analyzed in Figures 6.28 - 6.30.

As shown in Figure 6.28, the electronic temperature for the plasma/monolith and plasma/catalyst systems is obviously lower than for the original discharge. Though the vibrational temperature in Figure 6.29 does not show any clear pattern between the three experiments, all temperatures seem to oscillate mostly between 7500-8000 K. Figure 6.30 shows that the rotational temperatures for the plasma/monolith and plasma/catalyst systems are slightly higher than the pure plasma system, indicating

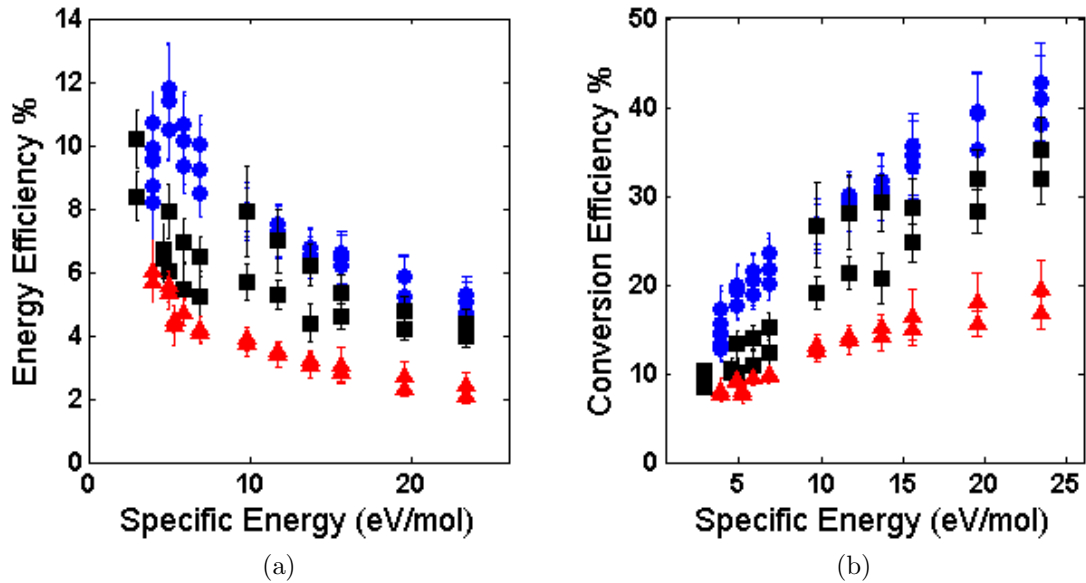


Figure 6.27: Summary of efficiency results for all three experiments: ● for the pure plasma system, ■ for the plasma/monolith system, and ▲ for the plasma/catalyst system.

the shift towards further equilibrium between T_v and T_r . The uncoated monolith and the catalyst-coated monolith must be affecting the plasma, particularly at high CO_2 flow rates.

It is probable that the geometry of the monolith caused a physical change in the plasma by impeding the exiting gas flow. Without the monolith insert, the plasma flows through the discharge tube with a clear circular cross-sectional area of 79 mm^2 . However the monolith cross section consists of a honeycomb-like pattern of square-shaped holes from which gas must travel through. Each monolith has a diameter just under 10 mm to fit snugly into the discharge tube, resulting in approximately 30 holes per cross section, each with an inner area of 1.4 mm^2 . Thus with the presence of the monolith, the total gas-flow cross section becomes 45 mm^2 , a 43% reduction. From conservation of mass shown in Equation 6.7 with the substitution $\rho = P/RT$ using the Ideal Gas Law, there must be a change in particle velocity, pressure, or temperature when the cross-sectional area changes. Here \dot{m} is mass flow rate, ρ is gas density, v is

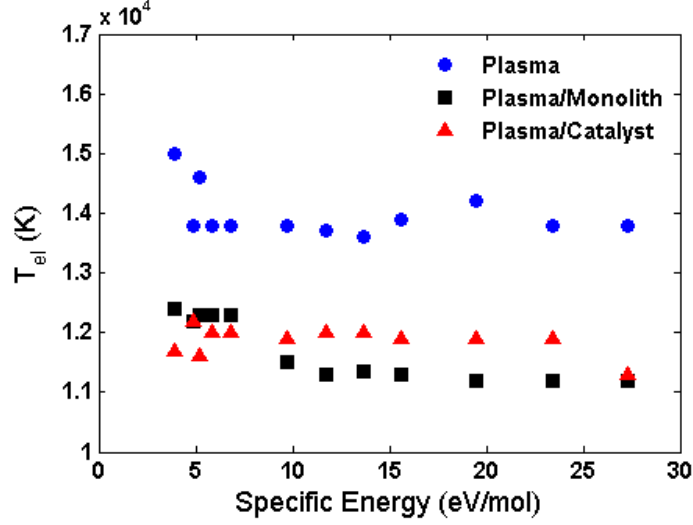


Figure 6.28: Summary of T_{el} results for all three plasma experiments

velocity, A is cross-sectional area, P is pressure, and R is the ideal gas constant.

$$\dot{m} = \rho v A = \frac{P}{RT_g} v A \quad (6.7)$$

While the total mass flow rates of each input species C, O and Ar must be conserved, the complex chemical reactions taking place in the plasma are causing changes in species density and velocity. Without a pressure gauge to record the pressure inside the tube, there is no way to determine if the pressure is changing before or after the placement of the monolith. There is most likely some amount of overall gas cooling once gas leaves the discharge region and begins exiting the tube, which can help balance the decreasing cross section. However it is possible that the local discharge pressure upstream of the monolith also increases as compensation. Higher pressures typically lead to lower dissociation efficiencies [37] which could explain the results of monolith and catalyst experiments. This trend was also evident in the computational results of Figure 6.26b which showed that at lower operating pressures the conversion efficiency increases.

Based on the results of Figure 6.27, the Rh/TiO₂ catalyst has a strong negative

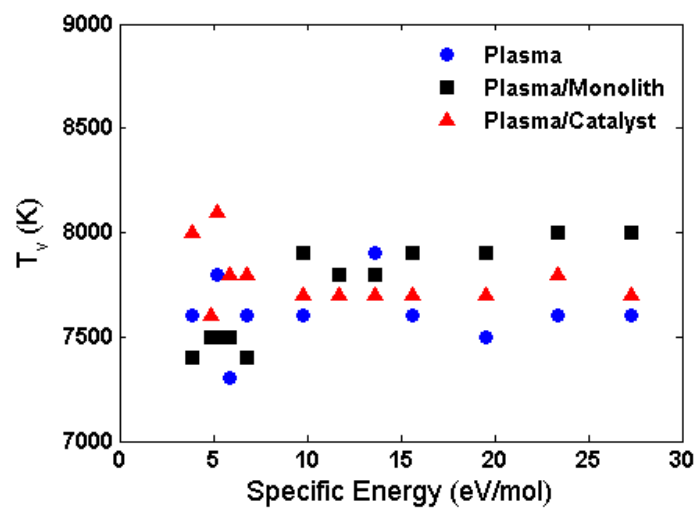


Figure 6.29: Summary of T_v results for all three plasma experiments

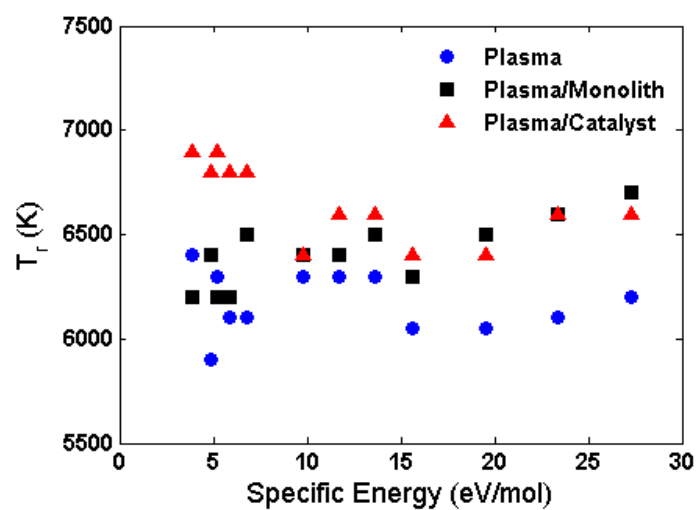


Figure 6.30: Summary of T_r results for all three plasma experiments

effect on CO₂ conversion to CO. Since the catalyst is placed downstream of the plasma, there should be little interaction between radical and excited species and the catalyst material. The average time it would take particles to travel from the end of the plasma to the location of the catalyst is about $10^{-4} - 10^{-5}$ s at the largest gas flow rates experimentally used. However, the typical lifetime of even long-lived species is only $10^{-14} - 10^{-10}$ s [37]. Therefore it is highly unlikely that any excited species or radicals exist by the time they reach the catalyst material, and hence the catalyst must be influencing reactions between neutral ground state species.

Specifically, the catalyst will enhance surface reactions given the large increase in surface area that the exiting gas must pass through before data collection at the RGA. The total surface area of a 2-cm-long monolith piece is about 30 cm², compared to only 6 cm² for a 2-cm-long section of tubing. This factor of 5 increase in surface area increases any possibility of collisional reactions with the surface. The catalyst was originally chosen to help lower the activation energy of the CO₂ dissociation reaction since it has been shown that CO₂ will dissociate on the surface of Rh [40, 104]. In fact the production of CO on the surface of Rh increases with increasing temperature [40], representing conditions closer to the work of this dissertation. However the dissociation products, CO and oxygen, can also recombine on the surface before desorption can occur [104], leaving the original Rh-dissociated CO₂ to desorb with a null CO production.

If the Rh catalyst can facilitate the reverse reaction between CO and O on the surface resulting from surface-dissociation of CO₂, then surely the plasma-created CO and oxygen hitting the surface can also participate in the reverse reaction. The reverse reaction, $CO + O_2 \rightarrow CO_2 + O$, is an exothermic process and thus energetically favorable releasing 0.3 eV/mol. Therefore it is likely that some of the plasma-created CO and oxygen simply recombined on the catalyst surface to produce CO₂ before exiting the discharge tube, ultimately lowering efficiencies. The sticking coefficients for

CO and oxygen, a measure of how well a species will adsorb on a surface as a function of coverage, have been reported as high on Rh surfaces. The same report shows that when Rh is pretreated with oxygen and exposed to CO, CO₂ is created [6]. The CO₂ creation rate also increases with temperature [35]. This CO oxidation reaction has been extensively studied with just a few examples listed here [14, 45, 98], and it may be difficult to find an appropriate catalyst to activate the endothermic CO₂ dissociation reaction preferred. Perhaps if different catalysts were tested or if the catalyst were placed directly in plasma using other configurations like a packed bed reactor, the efficiencies would increase for CO₂ dissociation

6.4.2 Computational Results

The discrepancy between computational and experimental results shown in Figures 6.21 and 6.22 indicates that the current model is leaving out other methods of CO production. As demonstrated by the results of the plasma/catalyst system, surface reactions play an important role in gas phase chemical reactions at atmospheric pressure with a high collision frequency and a small discharge volume. Just as catalyst surface reactions can influence the population of CO₂, it is likely that surface reactions are also influencing the production of CO through other reaction chemistry occurring in the experimental system. GlobalKin has a separate surface kinetics module specifically used to model the reactions occurring on a surface, though this surface module was not employed for the computational work presented here. However, there are other ways to simulate changes in gas composition due to reactions with the surface. Each species to be modeled has a user-defined sticking coefficient. First the user can define the fraction of species *A* to interact with, or be “consumed” by the surface. Then the user defines the fraction of “consumed” species *A* that will return to the plasma, also called the return branching ratio. Some of *A* may stick to the wall, indicating a non-zero sticking coefficient; some may return to the plasma; and some may return as

a different species, as when A reacts with species B on the surface to form AB . In this way, the effects of surface processes can be estimated in lieu of adding the official surface module to the simulation.

The results presented in Figure 6.31 display efficiency results for a set of simulations which included surface reactions with carbon atoms, labeled as the ‘Surface Reactions’ curve. The results are compared to the experimental results as well as the results for the model excluding any surface reactions. Carbon atoms were chosen as the primary in surface reactions because the OES spectra indicate that carbon is being produced in the plasma, but it does not consistently stick to the walls and remain in carbon form. Thus, carbon is necessarily sticking to the walls, reacting with other species in the discharge, and returning to the plasma in another form. Specifically in the simulation, surface reactions are included for neutral carbon atoms and excited oxygen atoms and molecules. The simulation assumes that 100% of carbon will react with the surface, with 50% returning to the plasma as carbon and 50% returning as CO. Similarly for excited molecular and atomic oxygen, only 5% will interact with the surface and of that 5%, half of the oxygen atoms will return as CO and half will return as ground state oxygen. The excited levels of atomic oxygen contain enough energy to overcome the activation energy required for carbon oxidation ($E_a < 2$ eV [38, 77]), and thus were appropriately chosen to interact with carbon on the surface to produce CO. The energy level diagrams for excited atomic and molecular oxygen can be seen in Appendix D.

The addition of these contrived surface reactions, though not a complete model, does demonstrate an improvement in overall efficiency in Figure 6.31. The ‘Surface Reactions’ curve comes in close agreement to experimental results for $E_v \approx 20 - 30$ eV/mol for both the energy efficiency and conversion efficiency curves. However the model is still unable to accurately predict CO production at low values of specific energy.

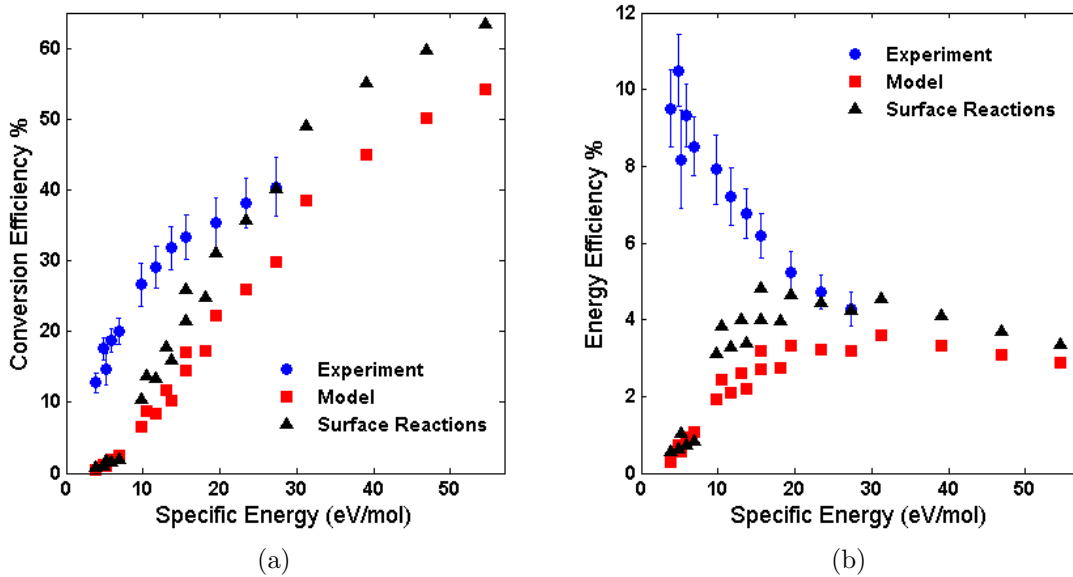


Figure 6.31: Computational efficiency results including surface reactions: a) energy efficiency, b) conversion efficiency.

The plasma properties simulated in GlobalKin have indicated that the discharge acts as purely non-thermal. This contradicts the experimental results which indicate a high gas temperature in thermal equilibrium with the vibrational temperature, where $T_g \approx 1/2T_e$. According to the simulation, $T_g < 1/10T_e$. In support of the experimental gas temperature, a published report of an atmospheric pressure surface wave discharge has also documented high gas temperatures when operating with molecular species. In this study, a 1 kW microwave-sustained N_2 discharge has a rotational temperature of around 5000 K (assumed equivalent to gas temperature), determined from the N_2^+ rotational spectrum [55]. Thus the experimentally measured gas temperature provides a better estimate than the simulation results.

The simulated electron densities, though, can actually support the experimental results. The electron density computed by GlobalKin for the CO_2 plasma is about 3-4 orders of magnitude lower than expected, based on experimental results reported for the non-thermal atmospheric pressure surface wave discharges shown in Figure 5.3. For the CO_2 plasma the ionization degree becomes only about $10^{-9} - 10^{-8}$, which is lower

than the minimum required value of 3×10^{-7} discussed in Section 3.2 to effectively stimulate the vibrational modes of CO_2 . The low ionization degree also leads to a decrease in the level of thermal non-equilibrium [37]. Hence, the lower-than-expected electron density has provided information to support the experimental results of low energy efficiency and high gas temperature.

Overall, the GlobalKin program does not provide a perfect model for the atmospheric pressure surface wave discharge. GlobalKin assumes a spatially uniform plasma, but surface wave discharges are neither axially nor radially uniform [55]. Particularly in contracted discharges, small changes in gas temperature can affect other plasma properties like electron density [72], which can affect the overall wave propagation. A more complete model would include a numerical solution of the full set of Maxwell's equations to account for changes in wave propagation, coupled self-consistently to a set of fluid-plasma equations for determining species densities and plasma temperatures. Such models have been developed and studied here [54, 72], and have shown good agreement with experimental results. Despite these faults, the GlobalKin model still provided useful information for characterizing the CO_2/Ar discharge.

6.4.3 Cost Analysis

An overall cost analysis of the MW system can be performed to determine the feasibility of the technology from an economic standpoint. In Chapter IV, a minimum energy efficiency was defined as $\eta_{min} = 52\%$ when a natural gas power plant with 60% energy conversion efficiency is used to power the plasma system. The highest energy efficiency reached in the atmospheric pressure microwave system was only 20%, but that only accounts for the efficiency of the dissociation process. A total plasma system efficiency can be calculated when taking into consideration the conversion of AC wall power to DC power in the MW power supply and the conversion of DC power to MW power at the magnetron head.

The efficiency of AC to DC conversion occurring at the MW power supply can be defined as

$$\eta_{AC \rightarrow DC} = (\text{power factor}) \times (\text{rectifier efficiency}) \quad (6.8)$$

where the power factor is the efficiency of AC to DC conversion and rectifier efficiency is the conversion of DC to DC. The MW power supply has a power factor rating of 0.74 while the rectifier efficiency is given as 90% [1], resulting in a total conversion efficiency of 67%. The total output DC power from the power supply is 3 kW, while the total MW output power is only 2 kW. Thus the conversion efficiency of DC power to MW is also 67%. Therefore the energy efficiency of the MW system before CO₂ dissociation is considered is only 45%. Even if the energy efficiency of dissociation is 100%, the total energy efficiency will never reach $\eta_{min} = 52\%$. When taking the power conversion losses into account, the total energy efficiency of the plasma system for CO₂ dissociation drops from its highest value of 20% to 9%, assuming all forward microwave power is transmitted to the plasma with no reflected power losses. This also assumes no other operating costs for external equipment like the recirculating chiller used in the experimental setup for this dissertation research.

The total MW system energy efficiency can be related to cost by using the current 2012 national average price of electricity. Since electricity used to power the plasma source currently costs 10 ¢/kW-hr, this can be used to calculate the cost of CO₂ dissociation. For $\eta_{total} = 9\%$, the energy requirement is 32 eV for every CO₂ molecule dissociated, equivalent to about 0.02 kW-hr/g of CO₂ destroyed. Using the average cost of electricity, the cost associated with dissociation is thus \$0.002/g of CO₂. In the U.S., the average amount of CO₂ emissions per kW-hr resulting from electricity and heat generation was 530 g/kW-hr between the years 2007-2009 [44]. Therefore the cost of eliminating CO₂ emissions from electricity and heat generation is \$1/kW-hr. To put this in perspective, the average American home annually consumes 11,500 kW-hrs of electricity [23]. This would cost each home \$11,500 to treat the CO₂ emissions

produced from electricity consumption alone.

The low pressure microwave system reported to achieve $\eta = 90\%$ [37] discussed in Section 5.1 can offer a realistic comparison. Assuming the same electrical energy losses to convert AC to MW power, the total energy efficiency becomes about 40%. This would result in about \$2,650 annually per household to eliminate all CO₂ emissions from electricity use. Putting this cost in the most commonly used measure of CO₂ emissions, it becomes \$400 per metric ton of CO₂ dissociated. In the year 2009, the U.S contributed a total of 5.5 billion metric tons of CO₂ emissions [31]. The cost required to reduce all of the CO₂ to CO in a plasma system with $\eta_{total} = 40\%$ is \$2 trillion. This would only treat emissions from one country for one year. The real operating cost would actually be a bit higher because this estimate does not include the electrical cost of the vacuum pump required to maintain low pressure during operation. Even in an ideal system with total energy efficiency of 100%, the cost reduces to \$1,100 annually per household. This becomes around \$180 per metric ton of CO₂ dissociated, or \$970 billion to treat all CO₂ emission in the 2009 from the U.S.

A cost comparison to other relevant emissions reduction technology will be useful for understanding how plasma dissociation might fit into an overall economic plan. CCS technology has been heavily researched and is already being implemented in some power plants. The cost estimates for CCS depend on a range of variables including the type of capture technology used, whether the technology is retrofit on existing plants or implemented on new construction, and if the technology is in the demonstration stage or past the early commercial stage. It also depends on how close the power plant is to the sequestration site. The total cost for capture, transport, and storage in a new-construction coal-fired initial demonstration power plant will cost \$86 - \$133 per metric ton of CO₂ sequestered [81]. Once the technology is past early commercial development, total cost is estimated to drop about 50% to \$44 - \$65 per metric ton. Retrofitting existing power plants increases costs by over 200% [81]. In any case, the

cost of CCS is still less than the plasma dissociation system, even when the plasma system is 100% efficient.

Even though CCS technology is slightly more cost effective, CCS only stores CO₂ somewhere else instead of being 'stored' in the atmosphere. The plasma system can actually change CO₂ into CO and oxygen, neither of which are technically considered global warming gases, though CO is toxic and can indirectly increase the global warming potential of other GHGs. Thus an overabundance of CO in the atmosphere will invariably cause other environmental challenges and is an undesirable outcome to the total plasma process. CO must find other practical uses, one such use being the creation of synthesis gas, also known as syngas. Syngas is composed of hydrogen and carbon monoxide, and can be used directly as a fuel or as an intermediate for generating synthetic liquid fuels. The CO produced from dissociation can be combined with previously produced hydrogen, or perhaps CO₂ and water vapor can be injected in the plasma system to simultaneously produce CO and H₂. In this configuration the waste CO₂ can produce a usable product via dissociation.

If the energy cost of CO₂ dissociation can be offset by the energy value of producing syngas in a CO₂/H₂O plasma, the technology becomes more economically favorable. The energy value, or heating value, of syngas depends on several factors including the gas composition, temperature of combustion, and the type of diluting agent, if any, that is used. Syngas is usually not manufactured as pure CO and H₂, and contains other species like CH₄, CO₂, N₂, and H₂O. In general, the lower heating value of syngas can range from 200-300 Btu/ft³ [106]. In comparison, natural gas has a much greater heating value near 1000 Btu/ft³. For a given syngas composition of 90% (H₂ + CO), the heating value is on the higher end of the syngas range at 319 Btu/ft³ [106]. This is equivalent to 0.002 kW-hr of energy released per gram of syngas burned. Thus if the energy cost of producing the syngas can fall below this value, then there is a net positive product of energy produced in the system. In comparison, the microwave

plasma source used in this dissertation had a cost of 0.02 kW-hr per gram of CO_2 dissociated. The plasma system for $\text{CO}_2/\text{H}_2\text{O}$ must be about an order of magnitude more cost efficient to create a positive net product of energy.

In addition to producing syngas, CO_2 can be combined with hydrogen-containing molecules to create other hydrocarbons. Specifically the conversion of CO_2 and CH_4 to higher hydrocarbons has been extensively studied in experimental plasma systems [62, 82, 93]. Typical products of the plasma conversion include gaseous hydrocarbons like ethylene, acetylene, and propylene as well as some liquid hydrocarbons and oxygenates. The process of CO_2 conversion to hydrocarbons has also been studied in photocatalytic reactors [86, 105]. In these reactors the energy can be supplied directly from solar panels, a renewable source, and the hydrogen can be produced from solar-powered water electrolysis. However, any dissociation or reforming process will be energy intensive and typical efficiencies for photocatalytic processes are usually less than 1% [86].

6.5 Summary

In summary, the atmospheric pressure microwave plasma source was experimentally tested for CO_2 dissociation in three different systems: the pure plasma, the plasma/monolith system, and the plasma/catalyst system. Each system produced different results, with the biggest change in efficiency occurring between the pure plasma and the plasma/catalyst systems. The computational work provided valuable insight into the mechanisms of CO production and some estimates for plasma properties.

Initial experiments performed in the pure plasma system showed the effects of adding CO_2 to an Ar discharge and the challenges of operating at atmospheric pressure. The emission spectra dramatically changed, eliminating almost all Ar neutral lines after the addition of CO_2 . The microwave energy was directed at vibrational excitation of CO_2 , not ionization, and Ar was used as an electron source. The variation of Ar flow

rates appeared to have an insignificant effect on dissociation efficiencies. Though the energy efficiency improved by almost a factor of seven over the results of Chapter IV, the inverse relationship between energy efficiency and conversion efficiency remained. Analysis of the optical emission spectra determined plasma temperature measurements, indicating thermal equilibrium between T_v and T_r . While energy was pumped into vibrational excitation of CO_2 , the vibrational modes quickly relaxed to translational modes.

The insertion of the uncoated monolith provided a small decrease in overall efficiencies, most likely due to changing the dynamics of gas flow exiting the discharge tube. The plasma temperature measurements changed slightly as well. However the Rh catalyst resulted in the largest change, with a strong decrease in efficiencies. While the Rh/ TiO_2 catalyst was chosen with hopes that it would facilitate CO_2 dissociation, it instead enabled the reverse reaction between CO and oxygen on the surface of the catalyst. The position of the catalyst downstream of the plasma limited any interaction between the catalyst and the excited and radical species which otherwise might have participated in CO_2 dissociation.

GlobalKin simulations were carried out to replicate the experimental operating conditions. The computed results for efficiencies were lower than the experimental results, particularly for high flow rates of CO_2 . The simulated electron temperature was higher, while the gas temperature was lower, than those provided by fitting SPECAIR simulations to the C_2 spectra. The addition of surface reactions to the simulation increased CO production and showed an improvement in overall efficiency.

CHAPTER VII

Conclusions

The aim of this dissertation was to determine the effectiveness of plasma CO₂ dissociation from an energy and economic standpoint as a method of carbon emission mitigation. Specifically, this aim was accomplished by experimentally studying CO₂ dissociation in an atmospheric pressure microwave plasma/catalyst system, providing an understanding of the plasma processes and properties relevant to dissociation. The uniquely intertwined energy and environmental challenges facing the world today require a solution to the overabundant carbon emissions and provide the practical motivation for this work. The atmospheric pressure plasma system was specifically designed and built for this purpose, taking into consideration the future need for large-scale industrial use. The dissociation of CO₂ was characterized for the atmospheric pressure plasma along with the plasma properties that affect dissociation. The influence of catalyst material was also characterized to determine the possibility of catalyst-enhanced dissociation. A global kinetic model was used to determine theoretical efficiencies and plasma properties of the system for comparison with the experimental results. Lastly, a cost analysis of the entire system was performed to determine the economic cost of using plasma technology for carbon mitigation.

This chapter serves to illustrate the main conclusions for this work, identifying the major contributions of the dissertation to the scientific community. Conclusions for

the experimental work are given in Section 7.1 and conclusions for the computational work are presented in Section 7.2. Section 7.3 describes the conclusions gained from the cost analysis of the microwave system, and lastly, suggestions for future work to proceed further in this research area will be offered in Section 7.4.

7.1 Experimental Conclusions

7.1.1 Development of Atmospheric Pressure Microwave Plasma Source

The experimental system was designed to meet the requirements of efficient CO₂ dissociation: a non-thermal discharge with $T_e > T_v > T_g$. The system was also designed with large-scale operation in mind to perform at atmospheric pressure, eliminating the operational and maintenance costs of a vacuum pump. Based on a review of the available literature, the microwave-excited surface wave plasma system was chosen for its ability to produce non-thermal and high electron density plasmas while operating at atmospheric pressure. Actual operation of the 2-kW microwave plasma requires external ignition when operating at atmospheric pressure because the applied electric field at 2 kW of input power is not capable of exceeding the necessary breakdown voltage for plasma ignition to occur. Typically, the external ignition source is in the form of a high voltage spark across the discharge tube generated by a Tesla coil. Additionally, the discharge tube requires a cooling mechanism to protect against melting due to high gas temperatures in the plasma. Mass spectrometry and optical emission spectroscopy are the main diagnostic tools implemented in the experimental setup, providing information on species and plasma temperature characterization, respectively.

7.1.2 Plasma System Characterization

The plasma system was experimentally characterized for various Ar/CO₂ flow rate ratios and MW power levels to determine optimum operating conditions for CO₂ dissociation. The addition of CO₂ to the pure Ar plasma caused several unexpected changes to the discharge. The effects of these changes can also be seen in the efficiency and temperature evaluations.

- The plasma cannot sustain itself at 2 kW with a pure CO₂ discharge at atmospheric pressure. The MW energy is primarily stimulates vibrational excitation and not ionization, resulting in a lack of electrons.
- The OES spectrum of the Ar/CO₂ plasma indicates that Ar acts as an electron source, as the Ar neutral emission lines are no longer present in the visible region. Thus the majority of Ar neutral species either become ions to sustain the plasma or are insufficiently excited to reach upper levels capable of emitting visible light on radiative decay.
- Once CO₂ is added to the discharge, C₂ becomes the dominant emitting species in the visible region, and the plasma glow visibly changes from light blue to green.
- Not only does the raw RGA spectrum indicate successful dissociation with peaks created for singly ionized CO and oxygen, but increasing power results in an increased flow of CO and oxygen exiting the discharge tube.
- Variation in Ar flow rate has no obvious affect on CO production.
- There is an unavoidable inverse relationship between energy efficiency and conversion efficiency of the dissociation process. Thus the highest energy efficiency achieved in the plasma system of 20% resulted in the lowest conversion rate of about 10%.

- Analysis of the C_2 spectra indicates that the microwave plasma does not produce a complete non-thermal plasma when operating with CO_2 as a major gas species. The vibrational and rotational gas temperatures are in thermal equilibrium, leading to low values of energy efficiency.

7.1.3 Plasma/Catalyst System Characterization

The plasma/catalyst system was characterized to determine the influence of the monolith structure and the Rh/TiO₂ catalyst material on CO₂ dissociation. Both the monolith and the catalyst resulted in changes to efficiencies and plasma temperatures.

- The monolith structure causes a slight efficiency loss for CO₂ dissociation
- The plasma temperatures at the discharge center move closer towards thermal equilibrium with the presence of the monolith downstream
- The monolith structure impedes exiting gas flow due to a 43% reduction in tube cross-sectional area, most likely resulting in higher pressure upstream of the monolith and leading to lower efficiencies.
- The monolith structure is not an appropriate design for this experimental system with high gas flow rates at atmospheric pressure.
- The Rh/TiO₂ catalyst coating causes a large drop in dissociation efficiency for this experimental configuration.
- The catalyst can be plausibly said to enhance the reverse reaction $CO + O_2 \rightarrow CO_2 + O$, resulting in an increased flow of CO₂ exiting the discharge tube.
- The Rh/TiO₂ coating is not an appropriate catalyst to facilitate CO₂ dissociation under high gas temperature conditions at atmospheric pressure

7.2 Computational Conclusions

A zero-dimensional computational model called GlobalKin was used to simulate the atmospheric pressure microwave plasma. While it was not a perfect model, it still provided important information on the characteristics of the CO₂/Ar plasma.

- Surface reactions play an important role in CO production, particularly between carbon and excited oxygen species
- The model predicted a pure non-thermal plasma, contradicting the experimental results
- The simulated electron density, though unable to be experimentally measured, is too low to maintain a population of vibrationally excited species
- The low electron density implies a tendency towards thermal equilibrium and lower dissociation efficiencies
- As expected, lower pressures lead to higher efficiencies as the system shifts further towards non-equilibrium
- A zero-dimensional model cannot accurately simulate the surface wave discharge, particularly at high flow rates where the model breaks down. A model which includes numerical solutions to Maxwell's equations would provide more complete results.

7.3 Cost Impact

The total system energy efficiency of CO₂ dissociation was analyzed to determine the realistic feasibility of the technology for carbon emissions control. A cost comparison to CCS technology was used to relate the plasma technology to an emissions control technology currently being implemented in the United States.

- Total system energy efficiency will always be limited by energy conversion losses, reducing the plasma efficiency by 45%.
- Because of conversion losses, the total energy efficiency will never be greater than $\eta_{min} = 52\%$ required for a plasma system power from natural gas, and thus energy produced from any fossil fuel source will create more CO₂ than the system is able to simultaneously destroy.
- From an energy standpoint, the plasma system must be powered by renewable energy sources.
- If high energy efficiency ($\eta = 90\%$) is achieved in the plasma system, the total cost per metric ton of CO₂ dissociated becomes comparable to the cost of implementing CCS technology in coal-fired power plants.
- Higher costs for CO₂ dissociation can be justified since the plasma system converts CO₂ into less-harmful gases, instead of simply storing CO₂ in geological locations.
- If the dissociation products can be used to produce a usable final product such as syngas or other hydrocarbons, the technology becomes economically appealing.

7.4 Future Work

The scope of this dissertation was to contribute to existing knowledge of CO₂ plasmas by characterizing the dissociation of CO₂ in an atmospheric pressure microwave plasma/catalyst system as well as determining the cost requirements that would make such a system competitive against other carbon reduction technologies. Given the experimental results presented here, suggestions can be made for modification of the existing system which may produce more desirable results. Modifications to

the computational plasma model can also lead to a more informed design of the experimental plasma/catalyst system.

Some design modifications of the experimental system could lead to lower overall operational costs and possible higher efficiencies. First a different discharge cooling mechanism could be implemented to eliminate the need for a recirculating chiller during continued operation at atmospheric pressure. A vortex gas flow formed via tangential gas injection would create a spiral of gas around the inner wall of the discharge tube, acting as a coolant by insulating the quartz walls from the hot plasma gas and thus preventing melting. This would lower overall operating cost by reducing electrical usage that would have been consumed by the chiller. Additionally, the vortex flow would act to stabilize the discharge in the center of the tube, which could enable successful testing at higher CO₂ flow rates. Then the desired operating range for specific energy $E_v = 0.3 - 1$ eV/mol could be reached when CO₂ flow rates are increased, potentially increasing the maximum energy efficiency achievable in the microwave plasma at atmospheric pressure. Since CO₂ has strong emissions in the deep IR, Fourier Transform Infrared (FTIR) spectroscopy could be a useful tool to measure plasma temperatures directly from the CO₂ emission spectra rather than relying on C₂. Also, other types of metal catalysts could also be tested on different supports. Specifically the catalyst support Al₂O₃ has been reported to increase CO₂ dissociation efficiencies. The monolith structure can also be modified with larger hole size for less gas flow constriction as gas exits the discharge tube.

A larger modification to the existing system could be made through the addition of a vacuum pump to allow for operation at low pressure. As reported in literature, operating the microwave system between 100-200 torr offers the advantage of producing a non-thermal discharge which can effectively stimulate the vibrational modes of CO₂ for dissociation processes. Another advantage to using a non-thermal plasma is the increased flexibility in catalyst placement. With lower gas temperatures, the catalyst

can be placed in direct contact with the discharge, a configuration which is known to have a greater affect on chemical reactivity. As such, the catalyst could be inserted in a packed-bed style in the form of pellets or a catalyst coating could be placed on the inner walls of the discharge tube. It is also important to go beyond examining the behavior of only CO₂ in the discharge, as the addition of hydrogen-containing compounds could produce usable products in the plasma. Thus is it recommended that the plasma chemistry of CO₂/H₂ or CO₂/H₂O systems should be studied and experimentally tested.

The computational model GlobalKin can be used to model the plasma-chemical reactions of a discharge comprised of CO₂ and hydrogen-containing species. The model can help design a plasma system to produce a given hydrocarbon outcome. As evident in the computational results, surface reactions play an important role in the chemical reactions occurring at atmospheric pressure. The simulation should be modified to include the surface reactions module to accurately model any reactions on the discharge tube surface. The surface module can also be used to model the effects of different catalyst material on dissociation of CO₂ or hydrocarbon production. Thus a more beneficial plasma/catalyst system could be experimentally tested.

APPENDICES

APPENDIX A

Description of Hönl-London Factors

The Hönl-London factors indicate how the total emission intensity of a transition is distributed among rotational P-, Q-, and R-branches. For diatomic molecules such as C_2 , each branch is denoted by the change in rotational quantum number J . Using the notation J' for the lower state and J'' for the upper state, $\Delta J = J'' - J'$. The R-branch is given by $\Delta J = 1$, the P-branch is given by $\Delta J = -1$ and the Q-branch is for $\Delta J = 0$. The shape and intensity of each branch is determined by the change in the orbital angular momentum quantum number Λ for a given transition. For $\Lambda = 0, 1, 2, 3, \dots, L$, the corresponding molecular state is designated by $\Sigma, \Pi, \Delta, \Phi, \dots$, where L is the orbital angular momentum [41]. For the Swan system of concern here, the transition occurs between electronic triplet states $d^3\Pi_g \leftrightarrow a^3\Pi_u$. Both states have quantum number $\Lambda = 1$, resulting in $\Delta\Lambda = 0$. The Hönl-London formulae for this transition are [41]:

$$S_J^R = \frac{(J'' + 1 + \Lambda'')(J'' + 1 - \Lambda'')}{J'' + 1} \quad (\text{A.1a})$$

$$S_J^Q = \frac{(2J'' + 1)\Lambda''^2}{J''(J'' + 1)} \quad (\text{A.1b})$$

$$S_J^P = \frac{(J'' + \Lambda'')(J'' - \Lambda'')}{J''} \quad (\text{A.1c})$$

APPENDIX B

GlobalKin Modeled Reaction Species and Mechanisms

E	: 0.00	: -1] 0.	[0.	\$ 5.46E-4	# 1.00	0.00	E	!
CO2	: -4.06	: 0] 3.941	[195.2	\$ 44.010	# 0.00	0.00	CO2	!
CO2V	: -3.98	: 0] 3.941	[195.2	\$ 44.010	# 0.05	1.00	CO2	!
CO2^	: 9.24	: 1] 3.941	[195.2	\$ 44.010	# 1.00	1.00	CO2V	!
CO2V^	: 9.32	: 1] 3.941	[195.2	\$ 44.010	# 1.00	1.00	AR	!
AR	: 0.00	: 0] 3.542	[93.3	\$ 39.948	# 0.00	0.00	AR	!
AR*	: 11.60	: 0] 3.542	[93.3	\$ 39.948	# 1.00	1.00	AR	!
AR**	: 13.10	: 0] 3.542	[93.3	\$ 39.948	# 1.00	1.00	AR	!
AR^	: 15.76	: 1] 3.542	[93.3	\$ 39.948	# 1.00	1.00	AR	!
AR2*	: 11.06	: 0] 0.	[0.	\$ 79.896	# 1.00	2.00	AR	!
AR2^	: 14.50	: 1] 0.	[0.	\$ 79.896	# 1.00	2.00	AR	!
O2	: 0.00	: 0] 3.467	[106.7	\$ 31.999	# 0.00	0.00	O2	!
O2V	: 0.20	: 0] 3.467	[106.7	\$ 31.999	# 0.05	1.00	O2	!
O2*	: 0.98	: 0] 3.467	[106.7	\$ 31.999	# 0.01	1.00	O2	!
O2^	: 12.06	: 1] 3.467	[106.7	\$ 31.999	# 1.00	1.00	O2	!
O2-	: -0.43	: -1] 3.467	[106.7	\$ 31.999	# 1.00	1.00	O2	!
O	: 2.55	: 0] 3.050	[106.7	\$ 15.999	# 0.02	0.50	O	!
O*	: 1.97	: 0] 0.	[0.	\$ 15.999	# 0.01	0.50	O	!
O^	: 16.27	: 1] 3.050	[106.7	\$ 15.999	# 1.00	1.00	O	!
O-	: 1.05	: -1] 3.050	[106.7	\$ 15.999	# 1.00	1.00	O	!
O3	: 1.48	: 0] 0.	[0.	\$ 47.998	# 0.00	0.00	C	!
C	: 7.42	: 0] 3.385	[30.6	\$ 12.011	# 0.00	0.00	C	!
C^	: 18.65	: 1] 3.385	[30.6	\$ 12.011	# 1.00	1.00	CO	!
CO	: -1.16	: 0] 3.690	[91.7	\$ 28.010	# 0.00	0.00	CO	!
COV	: -0.15	: 0] 3.690	[91.7	\$ 28.010	# 0.05	1.00	CO	!
CO^	: 12.71	: 1] 3.690	[91.7	\$ 28.010	# 1.00	1.00	COV	!
COV^	: 13.72	: 1] 3.690	[91.7	\$ 28.010	# 1.00	1.00	M	!
M	: 0.00	: 0] 0.	[0.	\$ 1.000	# 0.00	0.00	TE	!
TE	: 0.00	: 0] 0.	[0.	\$ 1.000	# 0.00	0.00	TGAS	!
TGAS	: 0.00	: 0] 0.	[0.	\$ 1.000	# 0.00	0.00	EDEP	!
EDEP	: 0.00	: 0] 0.	[0.	\$ 1.000	# 0.00	0.00	PDEP	!
PDEP	: 0.00	: 0] 0.	[0.	\$ 1.000	# 0.00	0.00	SPEED	!
SPEED	: 0.00	: 0] 0.	[0.	\$ 1.000	# 0.00	0.00	POSITION	!
POSITION	: 0.00	: 0] 0.	[0.	\$ 1.000	# 0.00	0.00	MIS	!
MIS	: 0.00	: 0] 0.	[0.	\$ 1.000	# 0.00	0.00	*	!
*								!	
!								!	
!								!	
E + CO2 > CO2 + E	: 0.0E+00		[0.00] 0.0E+00	!	-851 \$0& 0.	# 0. %		
E + CO2 > CO2^ + E + E	: 0.0E+00		[0.00] 0.0E+00	!	-856 \$0& 0.	# 0. %		
E + CO2 > CO2V + E	: 0.0E+00		[0.00] 0.0E+00	!	-852 \$0& 0.	# 0. %		
E + CO2 > CO2V + E	: 0.0E+00		[0.00] 0.0E+00	!	-853 \$0& 0.	# 0. %		
E + CO2 > CO2V + E	: 0.0E+00		[0.00] 0.0E+00	!	-854 \$0& 0.	# 0. %		
E + CO2 > CO2V + E	: 0.0E+00		[0.00] 0.0E+00	!	-844 \$0& 0.	# 0. %		
E + CO2 > CO2V + E	: 0.0E+00		[0.00] 0.0E+00	!	-845 \$0& 0.	# 0. %		
E + CO2 > CO2V + E	: 0.0E+00		[0.00] 0.0E+00	!	-846 \$0& 0.	# 0. %		
E + CO2 > CO2V + E	: 0.0E+00		[0.00] 0.0E+00	!	-847 \$0& 0.	# 0. %		
E + CO2 > CO2V + E	: 0.0E+00		[0.00] 0.0E+00	!	-848 \$0& 0.	# 0. %		
E + CO2 > CO + O-	: 0.0E+00		[0.00] 0.0E+00	!	-855 \$0& 0.	# 0. %		
E + CO2 > CO + O + E	: 0.0E+00		[0.00] 0.0E+00	!	-849 \$0& 7.	# 0. %		
E + CO2 > CO + O + E	: 0.0E+00		[0.00] 0.0E+00	!	-850 \$0& 7.	# 0. %		
E + CO2^ > CO + O	: 0.0E+00		[0.00] 0.0E+00	!	-2232 \$0& 0.	# 0. %		
E + CO2^ > CO2^ + E	: 0.0E+00		[0.00] 0.0E+00	!	-2231 \$0& 0.	# 0. %		
!								!	
E + CO2V > CO2V + E	: 0.0E+00		[0.00] 0.0E+00	!	-2700 \$0& 0.	# 0. %		
E + CO2V > CO2 + E	: 0.0E+00		[0.00] 0.0E+00	!	-2701 \$0& 0.	# 0. %		
E + CO2V > CO2V^ + E + E	: 0.0E+00		[0.00] 0.0E+00	!	-2705 \$0& 0.	# 0. %		
E + CO2V > CO + O-	: 0.0E+00		[0.00] 0.0E+00	!	-2702 \$0& 0.	# 0. %		
E + CO2V > CO + O + E	: 0.0E+00		[0.00] 0.0E+00	!	-2703 \$0& 5.	# 0. %		
E + CO2V > CO + O + E	: 0.0E+00		[0.00] 0.0E+00	!	-2704 \$0& 5.	# 0. %		
E + CO2V^ > CO + O	: 0.0E+00		[0.00] 0.0E+00	!	-2726 \$0& 0.	# 0. %		
E + CO2V^ > CO2V^ + E	: 0.0E+00		[0.00] 0.0E+00	!	-2725 \$0& 0.	# 0. %		
!								!	
E + CO > CO + E	: 0.0E+00		[0.00] 0.0E+00	!	-945 \$0& 0.	# 0. %		

E + O2V > O2* + E	: 0.00E+00	[0.00]	0.0	!	-2098	\$0&	0.	#	0.	%
E + O2V > O + O + E	: 0.00E+00	[0.00]	0.0	!	-2099	\$0&	0.	#	0.	%
E + O2V > O* + O + E	: 0.00E+00	[0.00]	0.0	!	-2100	\$0&	0	#	0.	%
E + O2V > O2^ + E + E	: 0.00E+00	[0.00]	0.0	!	-2103	\$0&	0.	#	0.	%
E + O2V > O^ + O + E + E	: 0.00E+00	[0.00]	0.0	!	-2105	\$0&	0.	#	0.	%
!										
E + O2* > O- + O	: 0.00E+00	[0.00]	0.0	!	-2058	\$0&	0.	#	0.	%
E + O2* > O2V + E	: 0.00E+00	[0.00]	0.0	!	-2097	\$1&	0.	#	0.	%
E + O2* > O2* + E	: 0.00E+00	[0.00]	0.0	!	-2066	\$0&	0.	#	0.	%
E + O2* > O2 + E	: 0.00E+00	[0.00]	0.0	!	-2067	\$0&	0.	#	0.	%
E + O2* > O + O + E	: 0.00E+00	[0.00]	0.0	!	-2068	\$0&	0.	#	0.	%
E + O2* > O* + O + E	: 0.00E+00	[0.00]	0.0	!	-2069	\$0&	0.	#	0.	%
E + O2* > O2^ + E + E	: 0.00E+00	[0.00]	0.0	!	-2072	\$0&	0.	#	0.	%
E + O2* > O^ + O + E + E	: 0.00E+00	[0.00]	0.0	!	-2074	\$0&	0.	#	0.	%
!										
E + O3 > O- + O2	: 0.00E+00	[0.00]	0.0	!	-1978	\$0&	0.	#	0.	%
E + O3 > O2- + O	: 0.00E+00	[0.00]	0.0	!	-1979	\$0&	0.	#	0.	%
E + O3 > E + O2 + O*	: 0.00E-09	[0.00]	0.0E+00	!	1	\$0&	0.	#	0.	%
E + O > O* + E	: 0.0E+00	[0.00]	0.0E+00	!	-935	\$0&	0.	#	0.	%
E + O > O* + E	: 0.0E+00	[0.00]	0.0E+00	!	-936	\$0&	0.	#	0.	%
E + O > O^ + E + E	: 0.0E+00	[0.00]	0.0E+00	!	-941	\$0&	0.	#	0.	%
!										
E + O* > O + E	: 0.0E+00	[0.00]	0.0E+00	!	-943	\$0&	0.	#	0.	%
E + O* > O^ + E + E	: 0.0E+00	[0.00]	0.0E+00	!	-944	\$0&	0.	#	0.	%
E + E + O^ > O* + E	: 5.00E-27	[-4.50]	0.0E+00	!	10	\$0&	0.	#	0.	%
!										
E + E + C^ > C + E	: 5.00E-27	[-4.50]	0.0E+00	!	10	\$0&	0.	#	0.	%
!										
E + E + AR^ > AR** + E	: 5.00E-27	[-4.50]	0.0E+00	!	10	\$0&	0.	#	0.	%
E + AR > AR* + E	: 0.0E+00	[0.00]	0.0E+00	!	-2382	\$0&	0.	#	0.	%
E + AR > AR* + E	: 0.0E+00	[0.00]	0.0E+00	!	-2	\$0&	0.	#	0.	%
E + AR > AR** + E	: 0.0E+00	[0.00]	0.0E+00	!	-3	\$0&	0.	#	0.	%
E + AR > AR^ + E + E	: 0.0E+00	[0.00]	0.0E+00	!	-4	\$0&	0.	#	0.	%
E + AR* > AR** + E	: 0.0E+00	[0.00]	0.0E+00	!	-5	\$0&	0.	#	0.	%
E + AR* > AR^ + E + E	: 0.0E+00	[0.00]	0.0E+00	!	-6	\$0&	0.	#	0.	%
E + AR** > AR^ + E + E	: 0.0E+00	[0.00]	0.0E+00	!	-7	\$0&	0.	#	0.	%
E + AR* > AR + E	: 0.0E+00	[0.00]	0.0E+00	!	-274	\$0&	0.	#	0.	%
E + AR** > AR + E	: 0.0E+00	[0.00]	0.0E+00	!	-275	\$0&	0.	#	0.	%
!										
CO2^ + O2 > O2^ + CO2	: 5.60E-11	[0.00]	0.0E+00	!	1	\$0&	0.	#	0.	%
CO2^ + O > O^ + CO2	: 9.62E-11	[0.00]	0.0E+00	!	1	\$0&	0.	#	0.	%
CO2^ + O > O2^ + CO	: 1.64E-10	[0.00]	0.0E+00	!	1	\$0&	0.	#	0.	%
CO2^ + CO > CO2 + CO^	: 1.90E-12	[0.00]	0.0E+00	!	1	\$0&	0.	#	0.	%
CO2 + O > CO + O2	: 2.80E-11	[0.00]	2.650E+04	!	20	\$0&	999.	#	0.	%
CO2 + M > CO + O + M	: 8.48E-10	[0.00]	55557.	!	20	\$0&	999.	#	0.	%
CO2V + M > CO2 + M	: 1.00E-12	[0.00]	0.0E+00	!	1	\$0&	0.	#	0.	%
CO2 + M > CO2V + M	: 1.00E-12	[0.00]	9.300E+02	!	20	\$0&	0.	#	0.	%
!										
CO^ + CO2 > CO2^ + CO	: 1.10E-09	[0.00]	0.0E+00	!	1	\$0&	0.	#	0.	%
CO^ + O2 > O2^ + CO	: 1.40E-10	[0.00]	0.0E+00	!	1	\$0&	0.	#	0.	%
CO^ + O > O^ + CO	: 1.40E-10	[0.00]	0.0E+00	!	1	\$0&	0.	#	0.	%
CO^ + O2- > CO + O2	: 2.00E-07	[0.00]	0.0E+00	!	6	\$0&	0.	#	0.	%
CO + O2 > CO2 + O	: 4.20E-12	[0.00]	2.400E+04	!	20	\$0&	999.	#	0.	%
CO + O + M > CO2 + M	: 1.70E-33	[0.00]	1.510E+03	!	20	\$0&	999.	#	0.	%
CO + O3 > O2 + CO2	: 4.00E-25	[0.00]	0.0E+00	!	1	\$0&	999.	#	0.	%
COV + M > CO + M	: 1.00E-12	[0.00]	0.0E+00	!	1	\$0&	0.	#	0.	%
CO + M > COV + M	: 1.00E-12	[0.00]	5.797E+03	!	20	\$0&	999.	#	0.	%
!										
O + O2 + M > O3 + M	: 6.90E-34	[-1.25]	0.0E+00	!	20	\$0&	999.	#	0.	%
O* + O2 > O + O2	: 3.80E-11	[0.00]	0.0E+00	!	1	\$0&	0.	#	0.	%
O + O3 > O2 + O2	: 8.00E-12	[0.00]	2.060E+03	!	20	\$0&	999.	#	0.	%
O^ + CO2 > CO2^ + O	: 1.00E-09	[0.00]	0.0E+00	!	1	\$0&	0.	#	0.	%
O- + O2 > O2- + O	: 1.50E-12	[0.00]	0.0E+00	!	1	\$0&	0.	#	0.	%
O- + O > O2 + E	: 1.90E-10	[0.00]	0.0E+00	!	1	\$0&	0.	#	0.	%

```

O- + CO > CO2 + E          : 5.50E-10 [ 0.00 ] 0.0E+00 ! 1 $0& 0. # 0. %
O2- + O > E + O3           : 1.50E-10 [ 0.00 ] 0.0E+00 ! 1 $0& 0. # 0. %
O2- + O > O- + O2          : 1.50E-10 [ 0.00 ] 0.0E+00 ! 1 $0& 0. # 0. %
O2- + O2* > E + O2 + O2   : 2.00E-10 [ 0.00 ] 0.0E+00 ! 1 $0& 0. # 0. %
!
!O2^ + O2- > O2 + O2      : 2.00E-06 [ 0.00 ] 0.0E+00 ! 6 $0& 0. # 0. %
!O^ + O2- > O + O2        : 2.00E-06 [ 0.00 ] 0.0E+00 ! 6 $0& 0. # 0. %
O2^ + O2- > O2 + O2       : 2.00E-07 [ 0.00 ] 0.0E+00 ! 6 $0& 0. # 0. %
O^ + O2- > O + O2         : 2.00E-07 [ 0.00 ] 0.0E+00 ! 6 $0& 0. # 0. %
O- + O^ + M > O2 + M      : 1.20E-25 [ 0.00 ] 0.0E+00 ! 4 $0& 0. # 0. %
O- + CO2^ > O + CO2       : 3.00E-06 [ 0.00 ] 0.0E+00 ! 6 $0& 0. # 0. %
!
!O- + CO^ > O + CO        : 3.00E-06 [ 0.00 ] 0.0E+00 ! 6 $0& 0. # 0. %
!O- + CO2^ > O + CO2      : 3.00E-06 [ 0.00 ] 0.0E+00 ! 6 $0& 0. # 0. %
O- + CO^ > O + CO         : 2.00E-07 [ 0.00 ] 0.0E+00 ! 6 $0& 0. # 0. %
O- + CO2^ > O + CO2       : 2.00E-07 [ 0.00 ] 0.0E+00 ! 6 $0& 0. # 0. %
O* + O3 > O2 + O + O      : 1.20E-10 [ 0.00 ] 0.0E+00 ! 1 $0& 0. # 0. %
O + O + M > O2 + M        : 5.21E-35 [ 0.00 ] -9.000E+02 ! 20 $0& 999. # 0. %
C^ + O- > C + O           : 5.00E-08 [ 0.00 ] 0.0E+00 ! 6 $0& 0. # 0. %
C^ + O2- > C + O2         : 5.00E-08 [ 0.00 ] 0.0E+00 ! 6 $0& 0. # 0. %
C + O2 > CO + O           : 2.60E-11 [ 0.00 ] 0.0E+00 ! 1 $0& 999. # 0. %
O2 + M > O + O + M        : 5.167E-10 [ 0.00 ] 58410. ! 20 $0& 999. # 0. %
O3 + M > O2 + O + M       : 1.559E-09 [ 0.00 ] 11490. ! 20 $0& 999. # 0. %
O* + CO2 > O2 + CO        : 2.00E-10 [ 0.00 ] 0.0E+00 ! 1 $0& 0. # 0. %
O* + CO2 > O + CO2        : 2.50E-10 [ 0.00 ] 0.0E+00 ! 1 $0& 0. # 0. %
O* + O2* > O + O2         : 1.00E-11 [ 0.00 ] 0.0E+00 ! 1 $0& 0. # 0. %
O* + O > O + O            : 1.00E-11 [ 0.00 ] 0.0E+00 ! 1 $0& 0. # 0. %
O2* + O2 > O2 + O2        : 2.20E-18 [ 0.00 ] 0.0E+00 ! 1 $0& 0. # 0. %
O2* + O2 > O + O3         : 2.95E-21 [ 0.00 ] 0.0E+00 ! 1 $0& 0. # 0. %
O2* + CO2 > O2 + CO2      : 3.00E-18 [ 0.00 ] 0.0E+00 ! 1 $0& 0. # 0. %
O2* + O3 > O2 + O2 + O    : 9.96E-11 [ 0.00 ] 3.050E+03 ! 20 $0& 0. # 0. %
O2V + M > O2 + M          : 1.00E-12 [ 0.00 ] 0.0E+00 ! 1 $0& 999. # 0. %
O2 + M > O2V + M          : 1.00E-12 [ 0.00 ] 2.318E+03 ! 20 $0& 0. # 0. %
O* + CO > CO2             : 3.80E-11 [ 0.00 ] 0.0E+00 ! 1 $0& 0. # 0. %
O* + CO > CO + O          : 1.50E-11 [ 0.00 ] 0.0E+00 ! 1 $0& 0. # 0. %
O* + O3 > O2 + O2         : 5.04E-10 [ 0.00 ] 0.0E+00 ! 1 $0& 0. # 0. %
O* + O > O + O            : 3.00E-12 [ 0.00 ] 0.0E+00 ! 1 $0& 0. # 0. %
!
O2- + AR^ > AR + O2        : 5.00E-07 [ 0.00 ] 0.0E+00 ! 6 $0& 0. # 0. %
O2- + AR2^ > AR + AR + O2 : 5.00E-07 [ 0.00 ] 0.0E+00 ! 6 $0& 0. # 0. %
O2- + CO2^ > CO2 + O2     : 5.00E-07 [ 0.00 ] 0.0E+00 ! 6 $0& 0. # 0. %
O- + AR^ > AR + O         : 5.00E-07 [ 0.00 ] 0.0E+00 ! 6 $0& 0. # 0. %
O- + O2^ > O2 + O         : 5.00E-07 [ 0.00 ] 0.0E+00 ! 6 $0& 0. # 0. %
!
AR^ + O2 > O2^ + AR        : 4.00E-11 [ 0.00 ] 0.0E+00 ! 1 $0& 0. # 0. %
AR^ + O3 > O2^ + AR + O   : 4.00E-11 [ 0.00 ] 0.0E+00 ! 1 $0& 0. # 0. %
AR* + O2 > O* + O + AR    : 2.10E-10 [ 0.00 ] 0.0E+00 ! 1 $0& 0. # 0. %
AR** + O3 > O* + O2 + AR : 2.10E-10 [ 0.00 ] 0.0E+00 ! 1 $0& 0. # 0. %
AR** + O3 > O* + O2 + AR : 2.10E-10 [ 0.00 ] 0.0E+00 ! 1 $0& 0. # 0. %
AR** + O2 > O* + O + AR  : 2.10E-10 [ 0.00 ] 0.0E+00 ! 1 $0& 0. # 0. %
AR** + AR + M > AR2* + M : 3.00E-33 [ 0.00 ] 0.0E+00 ! 1 $0& 0. # 0. %
AR2* > AR + AR            : 6.00E+07 [ 0.00 ] 0.0E+00 ! 1 $0& 0. # 0. %
AR2* + E > AR + AR + E   : 1.00E-07 [ 0.00 ] 0.0E+00 ! 1 $0& 0. # 0. %
AR^ + AR + M > AR2^ + M   : 2.00E-31 [ 0.00 ] 0.0E+00 ! 1 $0& 0. # 0. %
AR2^ + E > AR* + AR       : 1.00E-07 [ 0.00 ] 0.0E+00 ! 1 $0& 0. # 0. %
AR2^ + O2 > O2^ + AR + AR : 1.20E-10 [ 0.00 ] 0.0E+00 ! 1 $0& 0. # 0. %
AR2^ + O- > AR + AR + O   : 1.00E-07 [ 0.00 ] 0.0E+00 ! 1 $0& 0. # 0. %
AR^ + CO2 > CO2^ + AR     : 5.00E-10 [ 0.00 ] 0.0E+00 ! 1 $0& 0. # 0. %
AR^ + CO > CO^ + AR       : 4.00E-11 [ 0.00 ] 0.0E+00 ! 1 $0& 0. # 0. %
AR2^ + CO2 > CO2^ + AR + AR : 1.10E-09 [ 0.0 ] 0.0E+00 ! 1 $0& 0. # 0. %
AR2^ + CO > CO^ + AR + AR : 8.50E-10 [ 0.0 ] 0.0E+00 ! 1 $0& 0. # 0. %
AR2^ + O2 > O2^ + AR + AR : 1.20E-10 [ 0.0 ] 0.0E+00 ! 1 $0& 0. # 0. %
AR* + CO2 > CO + O + AR   : 5.30E-10 [ 0.00 ] 0.0E+00 ! 1 $0& 0. # 0. %
AR* + CO > C + O + AR     : 1.40E-11 [ 0.00 ] 0.0E+00 ! 1 $0& 0. # 0. %

```

APPENDIX C

Tabulated Empirical Values for CO₂ Reactions

#	Elementary chemical reactions	ΔH , $\frac{\text{kcal}}{\text{mole}}$	A , $\frac{\text{cm}^3}{\text{s}}$, $\frac{\text{cm}^6}{\text{s}}$	E_a , $\frac{\text{kcal}}{\text{mol}}$	α
1	$\text{CO}_2 + \text{CO}_2 \rightarrow \text{CO} + \text{O} + \text{CO}_2$	125.8	$4.39 \cdot 10^{-7}$	128.6	1
2	$\text{CO}_2 + \text{CO} \rightarrow \text{CO} + \text{O} + \text{CO}$	125.8	$4.39 \cdot 10^{-7}$	128.6	1
3	$\text{CO}_2 + \text{O}_2 \rightarrow \text{CO} + \text{O} + \text{O}_2$	125.8	$3.72 \cdot 10^{-10}$	119.6	1
4	$\text{CO} + \text{O} + \text{CO}_2 \rightarrow \text{CO}_2 + \text{CO}_2$	-125.8	$6.54 \cdot 10^{-36}$	4.3	0
5	$\text{CO} + \text{O} + \text{CO} \rightarrow \text{CO}_2 + \text{CO}$	-125.8	$6.54 \cdot 10^{-36}$	4.3	0
6	$\text{CO} + \text{O} + \text{O}_2 \rightarrow \text{CO}_2 + \text{O}_2$	-125.8	$6.51 \cdot 10^{-36}$	-3.7	0
7	$\text{O} + \text{CO}_2 \rightarrow \text{CO} + \text{O}_2$	7.8	$7.77 \cdot 10^{-12}$	33.0	0.5
8	$\text{CO} + \text{O}_2 \rightarrow \text{CO}_2 + \text{O}$	-7.8	$1.23 \cdot 10^{-12}$	25.2	0
9	$\text{O}_2 + \text{O}_2 \rightarrow \text{O} + \text{O} + \text{O}_2$	118.0	$8.14 \cdot 10^{-9}$	118.6	1
10	$\text{O}_2 + \text{O} \rightarrow \text{O} + \text{O} + \text{O}$	118.0	$2.0 \cdot 10^{-8}$	114.9	1
11	$\text{O}_2 + \text{CO} \rightarrow \text{O} + \text{O} + \text{CO}$	118.0	$2.4 \cdot 10^{-9}$	118.0	1
12	$\text{O}_2 + \text{CO}_2 \rightarrow \text{O} + \text{O} + \text{CO}_2$	118.0	$2.57 \cdot 10^{-9}$	111.5	1
13	$\text{O} + \text{O} + \text{O}_2 \rightarrow \text{O}_2 + \text{O}_2$	-118.0	$6.8 \cdot 10^{-34}$	0	0
14	$\text{O} + \text{O} + \text{O} \rightarrow \text{O}_2 + \text{O}$	-118.0	$2.19 \cdot 10^{-33}$	-4.5	0
15	$\text{O} + \text{O} + \text{CO} \rightarrow \text{O}_2 + \text{CO}$	-118.0	$2.75 \cdot 10^{-34}$	0	0
16	$\text{O} + \text{O} + \text{CO}_2 \rightarrow \text{O}_2 + \text{CO}_2$	-118.0	$2.75 \cdot 10^{-34}$	0	0

Figure C.1: Tabulated empirical values for CO_2 gas phase reactions. Gas phase reactions are shown with their enthalpies denoted by ΔH , the activation energy given by E_a , the pre-exponential factor A , and the efficiencies of vibrational excitation as α [37].

APPENDIX D

Excited Oxygen Energy Levels

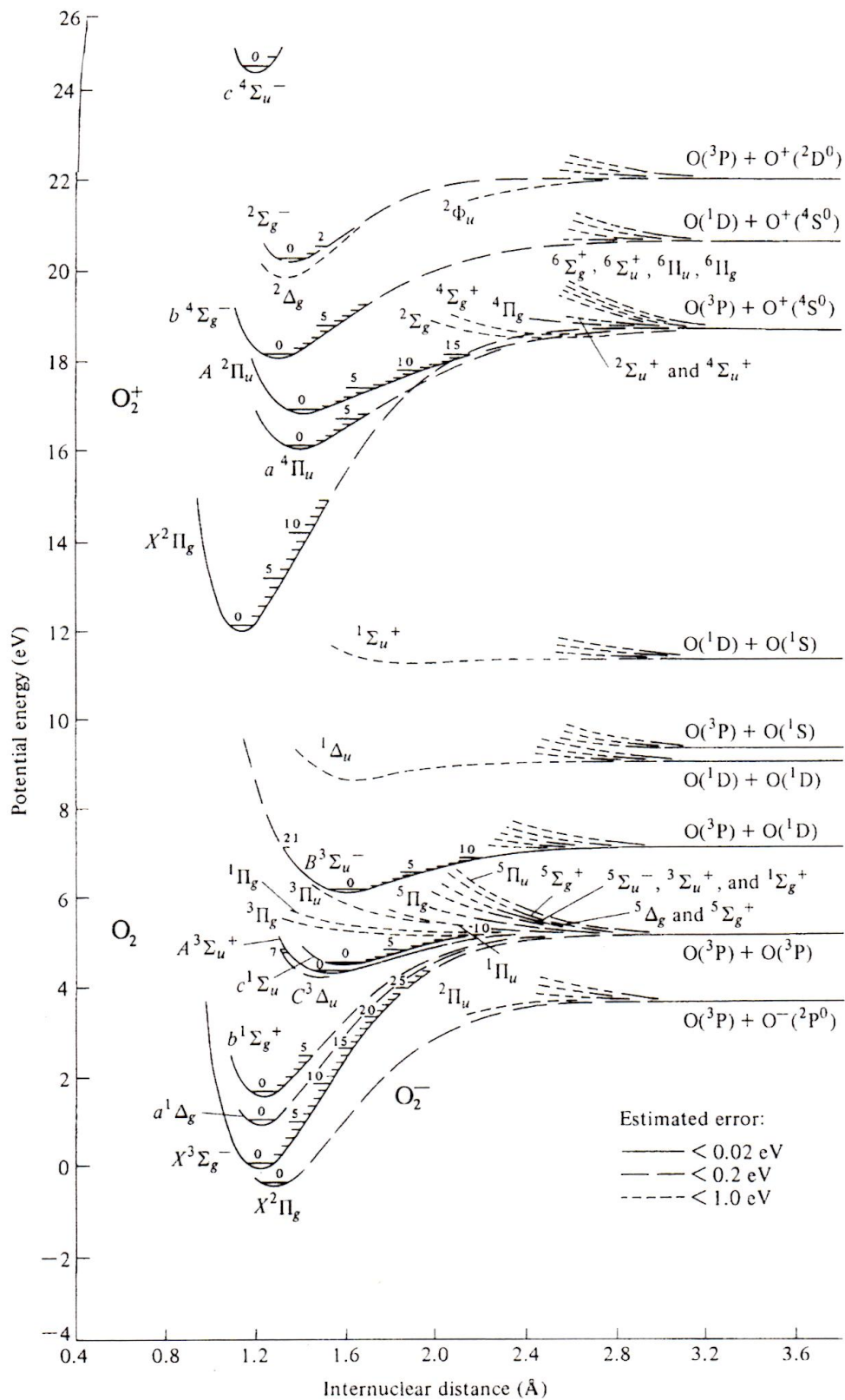


Figure D.2: Potential energy curves for O_2 [61].

BIBLIOGRAPHY

BIBLIOGRAPHY

- [1] Alter Power Systems. Switching power generation for a 2 kW magnetron. Technical report, Alter Power Systems, 2002.
- [2] Yacine Babou et al. Spectroscopic study of microwave plasmas of CO₂ and CO₂/N₂ mixtures at atmospheric pressure. *Plasma Sources Sci. Technol.*, 17, 2008.
- [3] Bo Bai, Herbert H. Sawin, and Brett A. Cruden. Neutral gas temperature measurements of high-power-density fluorocarbon plasmas by fitting swan bands of C₂ molecules. *Journal of Applied Physics*, 99, 2005.
- [4] Ananth Nuggehalli Bhoj. *Simulation of the Start Up Phase of Metal Halide Lamps*. PhD thesis, University of Illinois, 2004.
- [5] Olav Bolland and Henriette Undrum. A novel methodology for comparing CO₂ capture options for natural gas-fired combined cycle plants. *Advances in Environmental Research*, 7:901–911, 2003.
- [6] Michael Bowker, Quanmin Guo, and Richard Joyner. CO and O₂ adsorption on Rh(110). *Surface Sciences*, 253, 1991.
- [7] Michael C.J. Bradford and M. Albert Vannice. CO₂ reforming of CH₄ over supported Pt catalysts. *Journal of Catalysis*, 173, 1998.
- [8] Stephanie L. Brock et al. Plasma Decomposition of CO₂ in the Presence of Metal Catalysts. *Journal of Catalysis*, 180, 1998.
- [9] P.N. Brown, G.D. Bryrne, and A.C. Hindmarsh. VODE, a Variable-Coefficient ODE Solver. *SIAM Journal on Scientific and Statistical Computing*, 10, 1989.
- [10] M. Chaker, M. Moisan, and Z. Zakrzewski. Microwave and RF Surface Wave Sustained Discharges as Plasma Sources for Plasma Chemistry and Plasma Processing. *Plasma Chemistry and Plasma Processing*, 6, 1986.
- [11] Moo Been Chang and How Ming Lee. Abatement of perfluorocarbons with combined plasma catalysis in atmospheric-pressure environment. *Catalysis Today*, 89, 2004.

- [12] Hsin Liang Chen et al. Review of plasma catalysis on hydrocarbon reforming for hydrogen production - Interaction, integration, and prospects. *Applied Catalysis B: Environmental*, 85, 2008.
- [13] Hsin Liang Chen et al. Removal of Volatile Organic Compounds by Single-Stage and Two-Stage Plasma Catalysis Systems: A Review of the Performance Enhancement Mechanisms, Current Status, and Suitable Applications. *Environ. Sci. Technol.*, 43, 2009.
- [14] Byong K. Cho and Christopher J. Stock. Dissociation and oxidation of carbon monoxide over Rh/Al₂O₃ catalysts. *Journal of Catalysis*, 117, 1989.
- [15] C.O. Laux. SPECAIR. <http://www.specair-radiation.net>, May 2011.
- [16] M. Lino da Silva and M. Dudeck. Arrays of radiative transition probabilities for CO₂-N₂ plasmas. *Journal of Quantitative Spectroscopy and Radiative Transfer*, 102, 2006.
- [17] Rajesh Dorai, Khaled Hassouni, and Mark J. Kushner. Interaction between soot particles and NO_x during dielectric barrier discharge plasma remediation of simulated diesel exhaust. *Journal of Applied Physics*, 88, 2000.
- [18] Jim Van Durme et al. Combining non-thermal plasma with heterogeneous catalysis in waste gas treatment: A review. *Applied Catalysis B: Environmental*, 78, 2008.
- [19] Edward Rubin and Anand Rao. A Technical, Economic and Environmental Assessment of Amine-based CO₂ Capture Technology for Power Plant Greenhouse Gas Control. Technical report, Carnegie Mellon University Center for Energy and Environmental Studies, 2002.
- [20] Energy Information Administration. Documentation for Emission of Greenhouse Gases in the U.S. 2005. Technical Report DOE/EIA-0638(2005), Energy Information Administration, Office of Integrated Analysis and Forecasting, U.S. Department of Energy, 2007.
- [21] Energy Information Administration. Annual Energy Review 2010. Technical Report DOE/EIA-038(2010), Energy Information Administration, Office of Integrated Analysis and Forecasting, U.S. Department of Energy, 2011.
- [22] Energy Information Administration. Emission of Greenhouse Gases in the United States 2009. Technical Report DOE/EIA-0573(2009), Energy Information Administration, Office of Integrated Analysis and Forecasting, U.S. Department of Energy, 2011.
- [23] Energy Information Administration. Frequently Asked Questions. <http://www.eia.gov/tools/faqs/faq.cfm?id=97&t=3>, 2011.

- [24] Energy Information Administration. Greenhouse Gases. http://www.eia.gov/energyexplained/index.cfm?page=environment_about_ghg, April 2011.
- [25] Energy Information Administration. How dependent are we on foreign oil. http://www.eia.gov/energy_in_brief/foreign_oil_dependence.cfm, June 2011.
- [26] Energy Information Administration. International Energy Outlook 2011. Technical Report DOE/EIA-0484(2011), Energy Information Administration, Office of Integrated Analysis and Forecasting, U.S. Department of Energy, 2011.
- [27] Energy Information Administration. Use of nuclear power. http://www.eia.gov/energyexplained/index.cfm?page=nuclear_use, June 2011.
- [28] Energy Information Administration. What is renewable energy. http://www.eia.gov/energyexplained/index.cfm?page=renewable_home, October 2011.
- [29] Energy Information Administration. What is the role of coal in the United States. http://www.eia.gov/energy_in_brief/role_coal_us.cfm, May 2011.
- [30] Energy Information Administration. Where our natural gas comes from. http://www.eia.gov/energyexplained/index.cfm?page=natural_gas_where, November 2011.
- [31] Environmental Protection Agency. Inventory of U.S. Greenhouse Gas Emissions and Sinks:1990-2009. Technical report, Environmental Protection Agency, 2011.
- [32] Environmental Protection Agency. Past Climate Change. <http://www.epa.gov/climatechange/science/pastcc.html>, April 2011.
- [33] Environmental Protection Agency. Sea Level Changes. http://www.epa.gov/climatechange/science/recent_slc.html, April 2011.
- [34] Environmental Protection Agency. Temperature Changes. http://www.epa.gov/climatechange/science/recent_tc.html, April 2011.
- [35] A. Erdohelyi and F. Solymosi. Effects of the support on the adsorption and dissociation of CO and on the reactivity of surface carbon on Rh catalysts. *Journal of Catalysis*, 84, 1983.
- [36] T. Fleisch et al. Designing an efficient microwave-plasma source, independent of operating conditions, at atmospheric pressure. *Plasma Sources Sci. Technol.*, 16, 2007.
- [37] A. Fridman. *Plasma Chemistry*. Cambridge University Press, 2008.
- [38] Robert W. Froberg and Robert Essenhigh. Reaction order and activation energy of carbon oxidation during internal burning. In *Symposium (International) on Combustion*, volume 17, 1979.

- [39] J.M. Gomba, C. D'Angelo, D. Bertuccelli, and G. Bertuccelli. Spectroscopic characterization of laser induced breakdown in aluminium-lithium alloy samples for quantitative determination of traces. *Spectrochimica Acta B*, 56, 2001.
- [40] D.W. Goodman, D.E. Peebles, and J.M. White. CO₂ dissociation on rhodium: measurement of the specific rates on Rh(111). *Surface Science*, 140, 1984.
- [41] Gerhard Herzberg. *Molecular Spectra and Molecular Structure*. Krieger Publishing Company, 1950.
- [42] Howard Herzog and Dan Golomb. Carbon Capture and Storage from Fossil Fuel Use. *Encyclopedia of Energy*, 1:277–287, 2004.
- [43] Internal Revenue Service. Energy Provisions of the American Recovery and Reinvestment Act of 2009. <http://www.irs.gov/newsroom/article/0,,id=206871,00.html>, October 2011.
- [44] International Energy Agency. CO₂ Emissions from Fossil Fuel Combustion *Highlights*. Technical report, International Energy Agency, 2011.
- [45] T. Ioannides. CO oxidation over Rh dispersed on SiO₂, Al₂O₃, and TiO₂: kinetic study and oscillatory behavior. *Journal of Catalysis*, 156, 1995.
- [46] IPCC. *Special Report Emissions Scenarios. Contribution of Working Group III to the Third Assessment Report of the Intergovernmental Panel on Climate Change*. Cambridge University Press, 2000. IPCC-2000: WG3-TAR.
- [47] IPCC. *Climate Change 2001: The Physical Science Basis. Contribution of Working Group I to the Third Assessment Report of the Intergovernmental Panel on Climate Change*. Cambridge University Press, 2001. IPCC-2001: WG1-TAR.
- [48] IPCC. *Climate Change 2007: Mitigation of Climate Change. Contribution of Working Group III to the Fourth Assessment Report of the Intergovernmental Panel on Climate Change*. Cambridge University Press, 2007. IPCC-2007: WG3-AR4.
- [49] IPCC. *Climate Change 2007: The Physical Science Basis. Contribution of Working Group I to the Fourth Assessment Report of the Intergovernmental Panel on Climate Change*. Cambridge University Press, 2007. IPCC-2007: WG1-AR4.
- [50] John David Jackson. *Classical Electrodynamics*. John Wiley and Sons, Inc., 1999.
- [51] M. Jasinski, Z. Zakrzewski, and J. Mizeracyk. Spectroscopic measurements of electron density in atmospheric pressure surface wave sustained discharge in argon. *Czechoslovak Journal of Physics*, 65, 2006.

- [52] John F. Gerling. Waveguide Components and Configurations for Optimal Performance in Microwave Heating Systems. Technical report, Gerling Applied Engineering, 2000.
- [53] John Reed. California Carbon Capture and Storage. http://www.climatechange.ca.gov/carbon_capture_review_panel/index.html, May 2012.
- [54] Y. Kabouzi, D.B. Graves, E. Castanos Martinez, and M. Moisan. Modeling of atmospheric-pressure plasma columns sustained by surface waves. *Physical Review E*, 75, 2007.
- [55] Y. Kabouzi et al. Abatement of perfluorinated compounds using microwave plasmas at atmospheric pressure. *Journal of Applied Physics*, 93, 2003.
- [56] J.H. Kim et al. Optical measurements of gas temperatures in atmospheric pressure RF cold plasma. *Surface and Coatings Technology*, 171, 2003.
- [57] Robert Kunzig. Geoengineering: How to Cool the Earth-At a Price. *Scientific American*, 2008.
- [58] Christophe Olivier Laux. *Optical Diagnostics and Radiative Emission of Air Plasmas*. PhD thesis, Stanford University, 1993.
- [59] C.O. Laux, T.G. Spence, C.H. Kruger, and R.N. Zare. Optical diagnostics of atmospheric pressure air plasmas. *Plasma Sources Sci. Technol.*, 12, 2003.
- [60] K.M. Lemmer, A.D. Gallimore, and T.B. Smith. Using a helicon source to simulate atmospheric re-entry plasma densities and temperatures in a laboratory setting. *Plasma Sources Science and Technology*, 18, 2009.
- [61] M. A. Lieberman and A. J. Lichtenberg. *Principles of Plasma Discharges and Materials Processing*. John Wiley and Sons, Inc., 2005.
- [62] Chang-Jun Liu et al. Methane Conversion to Higher Hydrocarbons in the Presence of Carbon Dioxide Using Dielectric-Barrier Discharge Plasmas. *Plasma Chemistry and Plasma Processing*, 21, 2001.
- [63] Z. Machala et al. Emission spectroscopy of atmospheric pressure plasmas for bio-medical and environmental applications. *Journal of Molecular Spectroscopy*, 243, 2007.
- [64] T. Maehara et al. Spectroscopic measurements of high frequency plasma in supercritical carbon dioxide. *Physics of Plasmas*, 16, 2009.
- [65] M. Moisan and Z. Zakrzewski. Plasma sources based on the propagation of electromagnetic surface waves. *J. Phys. D: Appl. Phys.*, 24, 1991.

- [66] M. Moisan, Z. Zakrzewski, R. Pantel, and P. LePrince. A Waveguide-Based Launcher to Sustain Long Plasma Columns Through the Propagation of an Electromagnetic Surface Wave. *IEEE Transactions on Plasma Science*, 12, 1984.
- [67] M. Moisan et al. Properties and applications of surface wave produced plasmas. *Revue Phys. Appl.*, 17, 1982.
- [68] National Oceanic and Atmospheric Administration National Climatic Data Center. Greenhouse gases frequently asked questions. <http://www.ncdc.noaa.gov/oa/climate/gases.html>, February 2010.
- [69] NaturalGas.org. Electric Generation Using Natural Gas. http://www.naturalgas.org/overview/uses_eletrical.asp, 2011.
- [70] Sonca V. T. Nguyen. *Hydrogen Production in a Radio-Frequency Plasma Source Operating on Water Vapor*. PhD thesis, University of Michigan, 2009.
- [71] Sonca V. T. Nguyen, John E. Foster, and Alec D. Gallimore. Operating a radio-frequency plasma source on water vapor. *Rev. Sci. Instrum.*, 80, 2009.
- [72] E. Casta nos Martinez, Y. Kabouzi, K. Makasheva, and M. Moisan. Modeling of microwave-sustained plasmas at atmospheric pressure with application to discharge contraction. *Physical Review E*, 70, 2004.
- [73] H. Nowakowska, Z. Zakrzewski, M. Moisan, and M. Lubanski. Propagation characteristics of surface waves sustaining atmospheric pressure discharges: the influence of the discharge processes. *J. Phys. D: Appl. Phys.*, 31, 1998.
- [74] Thorsten Oberreuther, Christian Wolff, and Arno Behr. Volumetric plasma chemistry with carbon dioxide in an atmospheric pressure plasma using a technical scale reactor. *IEEE Transactions on Plasma Science*, 31, 2003.
- [75] A. Okada and K. Kijima. Measurement of C₂ rotational temperature in ArSiH₄CH₄ inductively coupled plasma flame with Abel inversion. *J. Phys. D: Appl. Phys.*, 35, 2002.
- [76] Toshihiko Osaki and Toshiaki Mori. Kinetic studies of CO₂ dissociation on supported Ni catalysts. *React. Kinet. Catal. Lett.*, 87, 2006.
- [77] Saul Patai, E. Hoffmann, and L. Rajbenbach. The oxidation of carbon by air. I. Catalysis in the oxidation of carbon black by air. *Journal of Applied Chemistry*, 2, 2007.
- [78] Paul M. Bellan. *Fundamentals of Plasma Physics*. Cambridge University Press, 2006.
- [79] R.W.B. Pearse and A.G. Gaydon. *The Identification of Molecular Spectra*. Chapman and Hall, 1976.

- [80] S. Pellerin et al. Application of the (0,0) Swan band spectrum for temperature measurements. *J. Phys. D: Appl. Phys.*, 29, 1996.
- [81] Peter Folger. Carbon Capture and Sequestration (CCS). Technical report, Congressional Research Service, 2009.
- [82] M.H. Pham et al. Activation of methane and carbon dioxide in a dielectric-barrier discharge-plasma reactor to produce hydrocarbons: Influence of $\text{La}_2\text{O}_3/\gamma\text{-Al}_2\text{O}_3$ catalyst. *Catalysis Today*, 171, 2011.
- [83] Janos Rasko and Frigyes Solymosi. Infrared Spectroscopic Study of the Photoinduced Activation of CO_2 on TiO_2 and Rb/TiO_2 Catalysts. *Journal of Physical Chemistry*, 98, 1998.
- [84] E. Rathakrishnan. *Gas Dynamics*. New Delhi: Prentice Hall of India, 2003.
- [85] R.J. Farrauto and C.H. Bartholomew. *Fundamentals of Industrial Catalytic Processes*. Blackie Academic and Professional, 1997.
- [86] Somnath C. Roy et al. Toward Solar Fuels: Photocatalytic Conversion of Carbon Dioxide to Hydrocarbons. *ACS Nano*, 4:1259–1278, 2010.
- [87] V.D. Rusanov, A.A. Fridman, and G.V. Sholin. The physics of a chemically active plasma with nonequilibrium vibrational excitation of molecules. *Sov. Phys. Usp*, 24, 1981.
- [88] A. Sainz, M.C. Garcia, and M.D. Calzada. Study of a stationary surface-wave sustained neon plasma column at atmospheric pressure. In *32nd EPS Conference on Plasma Phys.*, 2005.
- [89] Kotaro Saito, Tetsuo Sakka, and Yukio H. Ogata. Rotational spectra and temperature evaluation of C_2 molecules produced by pulsed laser irradiation to a graphitewater interface. *Journal of Applied Physics*, 94, 2003.
- [90] L.A. Schlie, R.D. Rathge, and E.A. Dunklea. High UV ($\lambda \geq 2200$), visible, and near infrared ($\lambda \leq 0.8\mu\text{m}$) transmissive liquid coolant for high power microwave (2.45 GHz) plasma tubes. *Review of Scientific Instruments*, 62, 1991.
- [91] LaVern A. Schlie. Liquid Coolant for high Power Microwave Excited Plasma Tubes. U.S. Patent 5055741, 1991.
- [92] M. Bruce Schulman et al. Emission from oxygen atoms produced by electron-impact dissociative excitation of oxygen molecules. *Physical Review A*, 32, 1985.
- [93] Jan Sentek et al. Plasma-catalytic methane conversion with carbon dioxide in dielectric barrier discharges. *Applied Catalysis B: Environmental*, 94, 2010.

- [94] D. Singh et al. Techno-economic study of CO₂ capture from an existing coal-fired power plant: MEA scrubbing vs. O₂/CO₂ recycle combustion. *Energy Conversion and Management*, 44:3073–3091, 2003.
- [95] David Stack et al. Spectroscopic studies and rotational and vibrational temperature measurements of atmospheric pressure normal glow plasma discharges in air. *Plasma Sources Sci. Technol.*, 15, 2006.
- [96] David Shane Stafford. *Modeling of Singlet-Delta Oxygen Yields in Flowing Electric Discharges*. PhD thesis, University of Illinois, 2004.
- [97] G.D. Stancu, F. Kaddouri, D.A. Lacoste, and C.O. Laux. Atmospheric pressure plasma diagnostics by OES, CRDS and TALIF. *J. Phys. D: Appl. Phys.*, 43, 2010.
- [98] Xingcai Su, Paul Cremer, Y. Ron Shen, and Gabor A. Somorjai. High-pressure CO oxidation on Pt(111) monitored with infrared-visible sum frequency generation (SFG). *J. Am. Chem. Soc.*, 119, 1997.
- [99] Terry Dinan. Trade-Offs in Allocating Allowances for CO₂ Emissions. Technical report, Congressional Budget Office, 2007.
- [100] Magesh Thiyagarajan and John Scharer. Experimental investigation of ultraviolet laser induced plasma density and temperature evolution in air. *Journal of Applied Physics*, 104, 2008.
- [101] Masahara Tsuji et al. Decomposition of CO₂ into CO and O in a microwave-excited discharge flow of CO₂/He or CO₂/Ar mixtures. *Chemistry Letters*, pages 22–23, 2001.
- [102] Stephen R. Turns. *An Introduction to Combustion: Concepts and Applications*. McGraw-Hill, 2006.
- [103] V. Unnikrishnan et al. Measurements of plasma temperature and electron density in laser-induced copper plasma by time-resolved spectroscopy of neutral atom and ion emissions. *Pramana Journal of Physics*, 74, 2010.
- [104] M.F.H. van Tol, A. Gielbert, and B.E. Nieuwenhuys. The adsorption and dissociation of CO₂ on Rh. *Applied Surface Sciences*, 67, 1993.
- [105] Oomman K. Varghese et al. High-Rate Solar Photocatalytic Conversion of CO₂ and Water Vapor to Hydrocarbon Fuels. *Nano Letters*, 9:731–737, 2009.
- [106] Vincent G. McDonell. Key Combustion Issues Associated with Syngas and High-Hydrogen Fuels. Technical report, Advanced Power and Energy Program University of California, 2000.
- [107] Jin-Yun Wang et al. CO₂ decomposition using glow discharge plasmas. *Journal of Catalysis*, 185:152–159, 1999.

- [108] Yuezhong Wen and Xuanzhen Jiang. Decomposition of CO₂ Using Pulsed Corona Discharges Combined with Catalyst. *Plasma Chemistry and Plasma Processing*, 21, 2001.
- [109] J. Christopher Whitehead. Plasma catalysis: A solution for environmental problem. *Pure Appl. Chem.*, 82, 2010.
- [110] D. Wu, R. A. Outlaw, and R. L. Ash. Extraction of oxygen from CO₂ using glow-discharge and permeation techniques. *Journal of Vacuum Science and Technology A: Vacuum, Surfaces, and Films*, 14:408–414, 1996.
- [111] Lan Yu, Christophe O. Laux, Denis M. Packan, and Charles H. Kruger. Direct-current glow discharges in atmospheric pressure air plasmas. *Journal of Applied Physics*, 91, 2004.
- [112] Yu. Ralchenko and A.E. Kramida and J. Reader and NIST ASD Team (2011). NIST Atomic Spectra Database (ver. 4.1.0). <http://physics.nist.gov/asd>, June 2012.
- [113] Guangyun Zheng et al. The mutual conversion of CO₂ and CO in dielectric barrier discharge (DBD). *Plasma Chemistry and Plasma Processing*, 23, 2003.